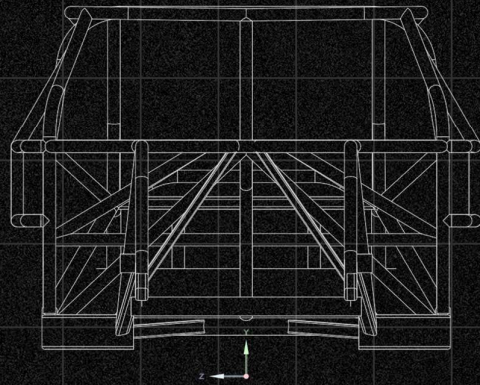


STUDY OF CAR ROOF CRUSHING DUE TO FALLING TREE TRUNK UNDER QUASI-STATIC & DYNAMIC LOADING FOR VARYING HEIGHTS & MATERIALS



$$[K]\{u\} = \{F\}$$

cdwr,all,filename,cdb

$$F = K_s \times u_s \times \ln \left(1 + \frac{u}{u_s} \right)$$

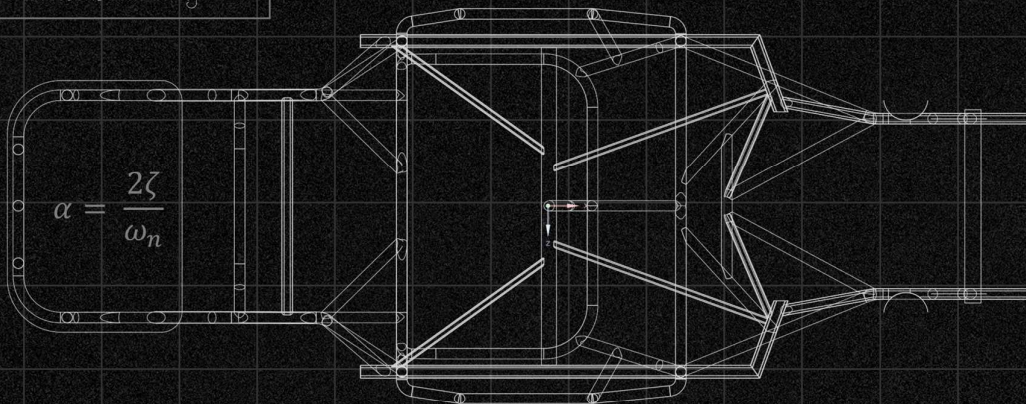
Non-linear Spring
Dynamics

$$\sigma = k + R + \sum_{i=1}^M \frac{C_i}{\gamma_i} (1 - e^{-\gamma_i \epsilon_p})$$

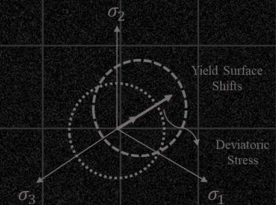
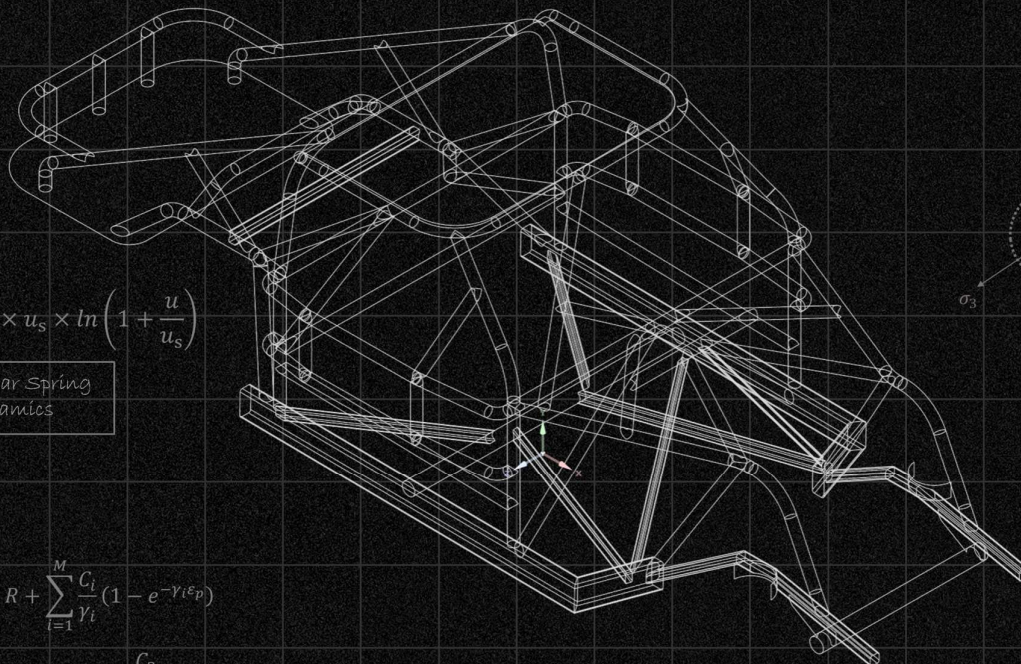
$$\sigma = \frac{C_1}{\gamma_1} (1 - e^{-\gamma_1 \epsilon_p}) + \frac{C_2}{\gamma_2} (1 - e^{-\gamma_2 \epsilon_p})$$

Chaboche Plasticity

$$\alpha = \frac{2\zeta}{\omega_n}$$



$$\{u_{n+1}\} = \{u_n\} + \{\dot{u}_n\} \Delta t + \left[\left(\frac{1}{2} - \alpha \right) \{\ddot{u}_n\} + \alpha \{\ddot{u}_{n+1}\} \right] \Delta t^2$$



global A n

loadA

n=length(A);

xmin=[0 0 0 0];

xmax=[1e5 800 1e4 400];

format shortg

u=rand(size(xmin));

Chirantan Gupta
Siddhartha Patra

Study of Car Roof Crushing due to Falling Tree Trunk under Quasi-Static & Dynamic Loading for Varying Heights & Materials

Thesis submitted in partial fulfilment of the requirements for the degree of
Master of Engineering in Automobile Engineering

By

Chirantan Gupta

Class Roll No: 002111204003

Examination Roll No: M4AUT23009

Registration No.: 160298 of 2021-2022

Under the supervision of

Dr. Siddhartha Patra

Submitted To

Department Of Mechanical Engineering

Faculty Of Engineering & Technology

Jadavpur University, Kolkata – 700032

Faculty Of Engineering And Technology
Jadavpur University

Kolkata-700032

Declaration of Originality and Compliance of Academic Ethics

*I hereby declare that this thesis entitled "**Study of Car Roof Crushing due to Falling Tree Trunk under Quasi-Static & Dynamic Loading for Varying Heights & Materials**" contains literature survey and original research work by the undersigned candidate, as part of Master of Automobile Engineering studies. All information in this document has been obtained and presented with academic rules and ethical conduct. I also declare that, as required by these rules and conduct, I have fully cited and referred all materials and results that are not original to this thesis.*

Name : Chirantan Gupta
Class Roll Number : 002111204003
Examination Roll Number : M4AUT23009
Registration Number : 160298 of 2021-2022

Signature:

Date:

Faculty Of Engineering And Technology
Jadavpur University

Kolkata-700032

Certificate Of Recommendation

We do hereby recommend that the thesis presented under our supervision by Chirantan Gupta (Roll No: 002111204003) entitled "Study of Car Roof Crushing due to Falling Tree Trunk under Quasi-Static & Dynamic Loading for Varying Heights & Materials" be accepted in partial fulfilment of the requirements for the degree of Master of Engineering in Automobile Engineering.

Thesis Supervisor

Dr. Siddhartha Patra
Dept. of Mechanical Engineering
Jadavpur University

Countersigned by

Prof. Amit Karmakar
(Head of the Department)
Mechanical Engineering
Jadavpur University

Prof. Saswati Mazumdar
(Dean)
Faculty of Engineering. & Technology
Jadavpur University

Faculty Of Engineering And Technology
Jadavpur University
Kolkata-700032

Certificate Of Approval

This foregoing thesis entitled "**Study of Car Roof Crushing due to Falling Tree Trunk under Quasi-Static & Dynamic Loading for Varying Heights & Materials**" is hereby approved as a credible study of an engineering subject carried out and presented in a manner satisfactory to warrant its acceptance as a prerequisite to the degree for which it has been submitted. It is understood that by this approval the undersigned does not endorse or approve any statement made, opinion expressed, or conclusion drawn there in but approves the thesis only for the purpose for which it has been submitted.

Committee for final evaluation of the thesis

Acknowledgements

I am deeply in debt and extremely thankful to my supervisor Dr. Siddhartha Patra, Department of Mechanical Engineering, Jadavpur University, for his noble guidance and support. He has been an ideal teacher, mentor, and thesis supervisor, offering advice and has been a true critic of my work, correcting mistakes and showing me the path whenever I encountered any problem. This thesis is a result of the countless number of one on one sessions and the late night discussions we had. His encouragement and belief in my abilities helped me complete this research work.

This project would not have been possible without the support of many people, especially my mother, Smt. Chitra Gupta. She is the source of my strength and beliefs. Her presence and our fun late night coffee sessions is what helped me pull the hectic all-nighters before the deadlines. To her, I give my everything, including this.

My heartfelt gratitude also goes to my friend Shourya Bhattacharyya, who has proved to be the truest friend in all these years, standing with me through difficulties providing guidance and humor. He has also been the source of my technical clarifications and other requirements for this work. Whenever I approached him with a new problem related to my work, he offered the best suggestions on how to tackle it effectively. His wise and valuable advice played an important role in making me possible to prepare this thesis.

I would also like to extend my gratitude to my eldest sister Mitali Biswas for being the awesome role model she is. Her positivity and outlook have greatly influenced me in overcoming the challenges that I faced.

Lastly, I want to thank my elder sister Dr. Pallabi Sengupta for being the source of my motivation. I am indebted to her for providing a constant source of humor and inspiration for the last one year. Her experience greatly helped me in delivering the best possible results.

Finally, I would also like to thank my alma mater, Jadavpur University, and all my professors for their invaluable sharing of knowledge and academic guidance which has helped me to shape myself as an enthusiastic learner of technology and as a person.

Date:

Chirantan Gupta

M.E (Automobile Engineering)
Department of Mechanical Engineering
Jadavpur University

Abstract

During vehicular accidents, there are several scenarios where the roof of the vehicle comes under direct load. The vehicular components like airbags and restraints (seatbelts) are responsible for providing safety, but the structural integrity of the roof determines the amount of cabin headspace the driver and the passengers get. Vehicular Rollover is one such accident where the roof can prevent fatal neck injury if it is structurally robust. When a heavy object falls from above, the roof becomes the only component that separates the passenger's head from the object. One such example is a heavy tree branch, or a trunk that has fallen on moving cars causing damage to the roof and compromising cabin head space. A limited amount of literature which analyses vehicular crashes is publicly available.

For studying this phenomenon, we conducted roof crushing simulations in ANSYS software. A NASCAR Car Frame CAD model obtained from the internet, was then modified slightly. The tree trunk was assumed to be 0.4 meters in diameter, 0.57 kg/m^3 dense, and weighs 1074 kg. We have broadly simulated four types of test cases. First, a quasi-static loading of the trunk on the centre of the roof. Second, a transient analysis of the trunk having a free fall vertically downwards on the roof from 0 m height above the roof. Third, a series of transient simulations of the tree trunk having a free fall from a height of at least 1m from the car roof. The height of the tree trunk from the roof was increased by 1m after each successful convergence till it reached 5m. Simulations were also conducted for 7.5m and 10m for a better understanding. Fourth, a set of two transient simulations where the height of free fall was fixed at 5 m above the roof. Each of these two simulations were performed with a material different from what was used to perform the previous simulations.

A total of eleven simulations were performed out of which one was static, and the rest were transient structural simulations. Eight out of the ten transient simulations were performed using the same material for the car frame while the height of free fall was varied from 0 m to 10 m. Three out of these transient simulations had the free fall height fixed at 5 m, but the material was varied for each and every simulation.

Seven parameters namely, the Equivalent Plastic Strain (ε_{eq}), Equivalent Stress (σ_{eq}), Roof Force (F_R), Suspension Spring Force (F_S), Suspension Damping Force (F_D), Total Suspension Force (F_T), and the Roof Distortion (u_R) were extracted and analysed. Close attention was also given to the roof and suspension forces while observing their change in behaviour as the height of free fall of the trunk and the car frame material was varied.

The Car frame did not undergo any plastic deformation when loaded under quasi-static conditions. The roof of the car kept crumbling to a dangerous amount as the height of free fall of the trunk was gradually increased beyond 1 m. Maximum plastic strain was observed locally at the location where the trunk and the roof made contact. For some cases, the maximum was also observed in the location where the rim of the roof was connected to the supporting pillars.

The intrusion of the roof into the passenger cabin i.e., the roof distortion exceeded 8 cm when the height of fall was increased to 2 m which can cause serious injuries. The cushioning effect offered by the roof and the frame structure along with the suspension was prominent when the height of free fall of the trunk was under 2 m. This effect gradually became negligible when the impact velocity exceeded 7 m/s.

An approximate relation was established between the quasi-static and dynamic loading of the car frame. This can be utilized to estimate the forces acting on the roof when compared to static behaviour which is still the trademark to formulate the Roof Strength of a passenger car.

The first chapter of the thesis is the introductory chapter. In this chapter we discussed about some basic terminologies like vehicular accidents, a vehicle's crashworthiness, different types of material behaviour, Isotropic and Kinematic hardening models, etc. related to this study to provide a better understanding. This was followed by the literature review comprising of the available literatures on several topics like the impact of vehicular crashes, different types of vehicular crashes that are analysed, different plasticity models, and the parameters utilised for conducting this study. The chapter ends with the scope of work and objectives of this study.

In the second chapter we discussed about the different methods which were implemented in order to conduct the simulations and extract the necessary results. A detailed description on the model preparation and simulation parameters is present in this chapter. The chapter also contains the necessary APDL commands implemented in pre-processing and post-processing of the simulations.

The third chapter encloses the meaningful and key observations deciphered after analysing the results generated from the simulations. The chapter also discusses in detail about the correlation between static and transient analyses results.

In the fourth and final chapter we discussed about a better variation of the scenario that has been considered for this research. Instead of the trunk falling perfectly aligned to the roof, it falls obliquely at an angle causing an imbalance of impact forces on the car frame. The chapter also provides necessary parameters and boundary conditions which can be implemented to conduct analyses on the aforementioned scenario.

Nomenclature

$[K]$	Stiffness Matrix
$\{u\}$	Nodal Displacement Vector
$\{F\}$	Nodal Force Vector
$[M]$	Mass Matrix
$[C]$	Damping Matrix
$\{\ddot{u}\}$	Nodal Acceleration vector
$\{\dot{u}\}$	Nodal Velocity Vector
$\{F(t)\}$	Time dependent Force Vector
α	Rayleigh Stiffness Damping Factor
β	Rayleigh Mass Damping Factor
t	Time
GDP	Gross Domestic Product per capita
VSL	Value of a Statistical Life
σ	Back Stress tensor
f	Yield Criterion
X	Kinematic Hardening Factor
R	Isotropic Hardening Factor
C_i	i^{th} Chaboche Back Stress Parameter
γ_i	i^{th} Chaboche exponential Parameter
ϵ_p	Plastic Strain
ζ	Damping Ratio
ω_n	Natural Frequency of the body
u_s	Spring Compression
ϵ_{eq}	Equivalent Plastic Strain
σ_{eq}	Equivalent von-mises Stress
k	Yield Stress

m_f	Face Sizing in cm
m_b	Body Sizing in cm
K_s	Spring Stiffness assuming linear behaviour
u_s	Maximum allowable Spring compression
u	Spring elongation or compression
M_c	Total mass of the Car Frame
σ_{ut}	Ultimate Tensile Strength
σ_N	True Stress
v_0	Impact velocity of the tree trunk
F_R	Roof Force
F_S	Suspension Spring Force
F_D	Suspension Damping Force
F_T	Total Suspension Force
u_R	Roof Distortion
u_{TD}	Total Roof Deformation
f_X^{\max}	Factor for the maximum value of Parameter X
f_0	Initial value of the factor at $h = 0$
f_Q	Maximum value of exponential dependence
b	Exponential Decay constant
f_m	Slope of the linear dependence of the factor
M_T	Mass of the Tree Trunk
Δu_{cg}	Displacement of the Centre of gravity of the Trunk
I_t	Moment of Inertia of the Trunk
L	Length of the Trunk
$\dot{\theta}$	Angular Velocity of impact of the Trunk

Contents

Acknowledgements.....	IV
Abstract.....	VI
Nomenclature.....	IX
List of Tables.....	XIII
Chapter 1: Introduction.....	1
1.1 Basic Concepts.....	1
1.1.1 Vehicular Accidents.....	1
1.1.2 Rollover Crash of Vehicles.....	2
1.1.3 Crashworthiness of a Vehicle.....	2
1.1.4 Roof Strength of a Vehicle.....	3
1.1.5 Material Behaviour of Car Frame.....	3
1.1.6 Plasticity Models.....	4
1.1.7 Finite Element Analysis on Vehicular Frame.....	5
1.1.8 Damping and its Sources.....	8
1.2 Literature Review.....	9
1.2.1 FEA and Vehicular Rollover.....	9
1.2.2 Scenarios with heavy impact on Vehicle Roof.....	10
1.2.3 Parameters for Modelling the Trunk and Car Frame.....	10
1.2.4 Materials for the Car Frame.....	11
1.2.5 Modelling Plasticity of the Car Frame.....	12
1.2.6 Formulation for the Dynamic Analysis of the Car Structure.....	13
1.3 Scope of Work.....	15
1.4 Objectives.....	16
Chapter 2: Methodology.....	17
2.1 Car Frame Meshing and Contact Preparation.....	17
2.2 Preparation of the Tree Trunk (Modelling and Meshing).....	21
2.3 Preparation of the Combined Model.....	22

2.4	Design & Implementation of Suspension and Support Springs.....	24
2.5	Modelling Plasticity with Chaboche Kinematic Hardening Model	26
2.6	Pre-processing	29
2.6.1	Lowering the Car Frame	29
2.6.2	Lowering the Trunk.....	30
2.6.3	Constraining the Damping and Wheel Springs.....	31
2.6.4	Constraining the Frictional Springs	33
2.6.5	Constraining the Non-linear Springs	33
2.7	Post-processing.....	35
2.7.1	Calculating the forces on the Roof.....	36
2.7.2	Calculating all the Suspension forces	38
2.8	System Specifications and Miscellaneous Parameters.....	40
Chapter 3:	Results and Discussion.....	42
3.1	Simulations with Heat Treated UHSS as the material	42
3.1.1	Car Frame loaded with the trunk under Static conditions.....	42
3.1.2	Free Fall from different heights under Transient conditions.....	44
3.2	Correlation between the Static and Transient Solutions.....	54
3.3	Simulations with $h = 5$ m using three Different Materials.....	64
3.4	Force vs. Time behaviour for $h = 5$ m using UHSS – Heat Treated as the material	70
Chapter 4:	Conclusion and Future Work.....	72
4.1	Conclusion.....	72
4.2	Future Scope of Work.....	73
References	i - vi

List of Tables

1. Table 1.1. Tyre and Suspension Stiffness values	13
2. Table 1.2. Values of Rayleigh Damping Coefficients	15
3. Table 2.1. Variance of the Maximum Equivalent Stress (σ_{eq}^{max}) for different mesh sizes.	18
4. Table 2.2. Total count of the elements and nodes in the contact and target region.....	23
5. Table 2.3. Parameters used for the calculation of suspension damping.....	25
6. Table 2.4. Chaboche Parameters for the three materials.....	27
7. Table 2.5. Ultimate Tensile Strength (σ_{ut}), Yield Stress (k), and Young's Modulus (E) of the three materials, UHSS Baseline, DP 350-600, and UHSS (Heated).	28
8. Table 2.6. Values of Initial velocity according to the height of free fall.....	31
9. Table 2.7. Specifications of the Computing Device Hardware used.	40
10. Table 2.8. Miscellaneous parameters pertaining to the simulations.	40
11. Table 3.1. Maximum values of Equivalent Plastic Strain (ϵ_{eq}), Equivalent Stress (σ_{eq}), and Roof Distortion (u_R) vs. Height (h) of free fall.	44
12. Table 3.2. Maximum values of Roof Force (F_R), Suspension Spring Force (F_S), Suspension Damping Force (F_D), and Total Suspension Force (F_T) vs. Height (h)	44
13. Table 3.3. Maximum value of Roof Deformation (u_{TD}) vs. Height (h) of free fall.....	45
14. Table 3.4. Values of the Max. Eq. Plastic Strain (ϵ_{eq}^{max}), Stress factor ($f_{\sigma_{eq}^{max}}$), Roof Force factor ($f_{F_R^{max}}$), Spring Force factor ($f_{F_S^{max}}$), Damping Force factor ($f_{F_D^{max}}$), Total Suspension Force factor ($f_{F_T^{max}}$), and Roof Deformation factor ($f_{u_R^{max}}$) vs. Height (h) of free fall.....	56
15. Table 3.5. Tabulation of the values of constants obtained for all the different parameters.	63
16. Table 3.6. Tabulation of the Maximum values of Equivalent Plastic Strain (ϵ_{eq}), Equivalent Stress (σ_{eq}), Roof Force (F_R), Suspension Spring Force (F_S), Suspension Damping Force (F_D), Total Suspension Force (F_T), and Roof Distortion (u_R) for the materials UHSS Heat Treated, DP 350-600, and UHSS Baseline.....	64
17. Table 3.7. Maximum value of Roof Distortion (u_{TD}) for the materials UHSS Heat Treated, DP 350-600, and UHSS Baseline	66

List of Figures

1. Figure 1.1. Schematic representation of the Yield Surface in the deviatoric stress space for (a) Isotropic Hardening and (b) Kinematic Hardening	4
2. Figure 2.1. (a) Isometric view, (b) Side view, and (c) Front view of the Car Frame.....	17
3. Figure 2.2. Isometric view of (a) highlighted components with different mesh size, (b) Meshed Car Frame showing the layout.	19
4. Figure 2.3. Different settings used for generating contacts.	20
5. Figure 2.4. Isometric view of all the generated bonded contacts.	20
6. Figure 2.5. (a) Plane of separation (AA') with the circumferential bias (b) Isometric view of the meshed tree trunk (c) Side view of the trunk showing the longitudinal bias.	21
7. Figure 2.6. Side view of the point mass attached to the tree trunk along with its properties.	22
8. Figure 2.7. Isometric view of the rough contact between (a) the Roof Surface and the tree trunk, (b) the Roof Rim and the tree trunk	23
9. Figure 2.8. Spring Force vs. Suspension travel of the non-linear spring	24
10. Figure 2.9. An isometric representation of all the 14 springs utilized to support the car frame.	25
11. Figure 2.10. Chaboche parameters comparison after fitting with the original data for material (a) UHSS Baseline, (b) DP 350-600, and (c) UHSS Heat Treated.	28
12. Figure 2.11. The Analysis settings used for carrying out the simulations.	35
13. Figure 2.12. Runtime utilization of the system hardware extracted with HW Monitor.	41
14. Figure 2.13. Runtime utilization of the CPU extracted with the Windows Task Manager.	41
15. Figure 3.1. Depiction of the Total Deformation across the (a) whole Car Frame in Isometric View, (b) whole Car Frame from Side View, and (c) enlarged portion of the side view emphasizing the Roof Deformation for the Static Analysis at $t = 1$ s.	43
16. Figure 3.2. Depiction of the Total Deformation across the (a) whole Car Frame in Isometric View, (b) whole Car Frame from Side View, and (c) enlarged portion of the side view emphasizing the Roof Deformation for the 0 m Height Transient Analysis at $t = 1$ s.	46

17. Figure 3.3. Depiction of the Total Deformation across the (a) whole Car Frame in Isometric View, (b) whole Car Frame from Side View, and (c) enlarged portion of the side view emphasizing the Roof Deformation for the 1 m Height Transient Analysis at $t = 1$ s.....	47
18. Figure 3.4. Depiction of the Total Deformation across the (a) whole Car Frame in Isometric View, (b) whole Car Frame from Side View, and (c) enlarged portion of the side view emphasizing the Roof Deformation for the 2 m Height Transient Analysis at $t = 1$ s.....	48
19. Figure 3.5. Depiction of the Total Deformation across the (a) whole Car Frame in Isometric View, (b) whole Car Frame from Side View, and (c) enlarged portion of the side view emphasizing the Roof Deformation for the 3 m Height Transient Analysis at $t = 1$ s.....	49
20. Figure 3.6. Depiction of the Total Deformation across the (a) whole Car Frame in Isometric View, (b) whole Car Frame from Side View, and (c) enlarged portion of the side view emphasizing the Roof Deformation for the 4 m Height Transient Analysis at $t = 1$ s.....	50
21. Figure 3.7. Depiction of the Total Deformation across the (a) whole Car Frame in Isometric View, (b) whole Car Frame from Side View, and (c) enlarged portion of the side view emphasizing the Roof Deformation for the 5 m Height Transient Analysis at $t = 1$ s.....	51
22. Figure 3.8. Depiction of the Total Deformation across the (a) whole Car Frame in Isometric View, (b) whole Car Frame from Side View, and (c) enlarged portion of the side view emphasizing the Roof Deformation for the 7.5 m Height Transient Analysis at $t = 1$ s.....	52
23. Figure 3.9. Depiction of the Total Deformation across the (a) whole Car Frame in Isometric View, (b) whole Car Frame from Side View, and (c) enlarged portion of the side view emphasizing the Roof Deformation for the 10 m Height Transient Analysis at $t = 1$ s.....	53
24. Figure 3.10. The Maximum Equivalent Stress (σ_{eq}^{max}) developed in the model for (a) 0 m Transient, (b) 1 m Transient, (c) 2 m Transient, and (d) 3 m Transient (e) 4 m Transient, (f) 5 m Transient, (g) 7.5 m Transient, and (h) 10 m Transient Simulations.	55
25. Figure 3.11. Plot of Max. Equivalent Plastic Strain (ϵ_{eq}^{max}) vs. h (m)	57

26. Figure 3.12. Plot of the Stress factor ($f_{\sigma_{eq}^{max}}$) vs. h (m) comparing the Fit.	58
27. Figure 3.13. Plot of the Roof Force factor ($f_{F_R^{max}}$) vs. h (m) comparing the Fit.	59
28. Figure 3.14. Plot of the Spring Force factor ($f_{F_S^{max}}$) vs. h (m) comparing the Fit.	60
29. Figure 3.15. Plot of the Damping Force factor ($f_{F_D^{max}}$) vs. h (m) comparing the Fit.	61
30. Figure 3.16. Plot of the Total Suspension Force factor ($f_{F_T^{max}}$) vs. h (m) comparing the Fit.	62
31. Figure 3.17. Plot of the Roof Distortion factor ($f_{u_R^{max}}$) vs. h (m) comparing the Fit. ...	63
32. Figure 3.18. The Maximum Equivalent Stress (σ_{eq}^{max}) developed in the model with frame material as (a) UHSS Heat Treated, (b) DP 350-600, and (c) UHSS Baseline.	65
33. Figure 3.19. Total Deformation across the (a) whole Car Frame in Isometric View, (b) whole Car Frame from Side View, and (c) enlarged portion of the side view emphasizing the Roof Deformation for the Transient Analysis at $t = 1$ s using DP 350-600 as the material.	67
34. Figure 3.20. Total Deformation across the (a) whole Car Frame in Isometric View, (b) whole Car Frame from Side View, and (c) enlarged portion of the side view emphasizing the Roof Deformation for the Transient Analysis at $t = 1$ s using UHSS – Baseline as the material.	68
35. Figure 3.21. Variation of the Roof Force (F_R) and Roof Distortion (u_R) with (a) Young's Modulus (E), and (b) Ultimate Tensile Strength (σ_{ut}) of the materials.	69
36. Figure 3.22. Dependence of the Roof Force (F_R) on time (t) when $h = 5$ m and UHSS – Heat Treated was the material used.	70
37. Figure 3.23. Dependence of the Damping Force (F_D), Spring Force (F_S), and Total Suspension Force (F_T) on time (t) for (a) the Front Wheel Suspension and (b) the Rear Wheel Suspension when $h = 5$ m and UHSS – Heat Treated was the material used.	71
38. Figure 4.1. (a) Diagrammatic representation of the phenomenon when the tree trunk falls on the car roof in an oblique orientation. (b) Schematic showing the angle of orientation of the trunk with respect to the road and its original position.	73
39. Figure 4.2. (a) Top view of the complete model. (b) Front view of the complete model.	74

Chapter 1: Introduction

The initial half of the introductory chapter provides an outline to the various terminologies and concepts which would be essential pertaining to this study. The next half contains a detailed literature review that has been conducted to study the effect of a falling tree on a car roof.

1.1 Basic Concepts

In this section, some of the important topics related to this study have been elaborated to enlist their individual key aspects and develop an overall understanding of the study.

1.1.1 Vehicular Accidents

Car accidents are unfortunate events that involve collisions or crashes involving vehicles, often leading to property damage, injuries, and sometimes even fatalities. These accidents can occur due to numerous factors, including human error, road conditions, weather, mechanical failures, and more. Common types of car accidents include rear-end collisions, side-impact crashes (also known as T-bone collisions), head-on collisions, and rollovers. The severity of accidents can range from minor fender-benders to more severe crashes leading to a wide range of injuries, including whiplash, fractures, sprains, and more. The severity of injuries varies based on the nature of the accident and the safety measures in place [1].

The consequences of car accidents can range from minor property damage to severe injuries or loss of life. Accidents can also lead to traffic congestion, legal proceedings, and increased insurance premiums. Governments and organizations often work to improve road safety through measures such as better road design, public awareness campaigns, stricter traffic laws, and improved vehicle safety features.

Every year the lives of approximately 1.3 million people are cut short as a result of a road traffic crash. Between 20 and 50 million more people suffer non-fatal injuries, with many incurring a disability as a result of their injury. Safe vehicles play a critical role in averting crashes and reducing the likelihood of serious injury. There are a number of regulations on vehicle safety that, if applied would potentially save many lives. These include requiring vehicle manufacturers to meet front and side impact regulations, to include electronic stability control, and to ensure airbags and seatbelts are fitted in all vehicles [2].

1.1.2 Rollover Crash of Vehicles

A vehicular rollover crash is a type of traffic collision in which a vehicle turns over onto its side or roof during an accident. This type of crash can happen to various types of vehicles, including cars, SUVs, trucks, and buses. Vehicular rollovers can vary in severity, ranging from minor incidents with no injuries to catastrophic accidents resulting in severe injuries or fatalities. Rollover crashes typically occur when a vehicle experiences a rapid change in its motion, often involving sharp turns, abrupt steering maneuvers, or collision impact. The vehicle's momentum can cause it to tip over due to the force generated during these actions [3]. SUVs and trucks with a higher centre of gravity are more susceptible to rollovers than lower-profile vehicles like sedans. However, any type of vehicle can potentially experience a rollover depending on the circumstances.

1.1.3 Crashworthiness of a Vehicle

Crashworthiness refers to a vehicle's ability to protect its occupants during a collision by minimizing the risk of injury. It encompasses the design, construction, and safety features of a vehicle that work together to absorb and dissipate the energy generated during a crash, thereby reducing the forces transferred to the occupants. Crashworthiness is a crucial aspect of vehicle safety and involves various engineering and design considerations. Key elements of a vehicle's crashworthiness include:

- **Structural Integrity:** The vehicle's structure should be designed to maintain its integrity and prevent excessive deformation during a collision. This involves using strong materials and well-engineered designs to ensure that the passenger compartment remains intact.
- **Occupant Restraint Systems:** Seat belts and airbags are primary occupant protection mechanisms. Seat belts keep occupants securely in their seats and prevent them from colliding with the vehicle's interior. Airbags deploy rapidly upon impact to cushion and protect the occupants from hitting hard surfaces.
- **Roof Strength:** A strong roof structure prevents the collapse of the passenger compartment in case of a rollover, reducing the risk of head and neck injuries.

Crashworthiness is tested through various crash tests, including frontal, side, and rollover tests conducted by regulatory agencies and independent organizations [4]. In conclusion, crashworthiness is a crucial aspect of vehicle safety, encompassing design, engineering, and regulatory standards to protect occupants during accidents.

1.1.4 Roof Strength of a Vehicle

The roof strength of a vehicle refers to its ability to maintain its structural integrity and prevent collapse during a rollover accident. A strong roof is essential for protecting occupants' heads and preventing serious injuries. The roof's ability to withstand the forces generated during a rollover is measured by its crush resistance. Stronger roofs deform less, maintaining a larger space between the roof and occupants' heads. Vehicles that meet or exceed the specified strength requirements receive a roof crush rating from the NHTSA (National Highway Traffic Safety Administration). A rating of 1 indicates the strongest roof, while a rating of 5 indicates the weakest. Ensuring a vehicle has a strong roof is an essential aspect of overall vehicle safety, particularly in situations where rollovers are possible.

1.1.5 Material Behaviour of Car Frame

1.1.5.1 Elastic Behaviour

Elastic deformation is the deformation that dissipates when the external forces that caused the modification and tension linked with it are removed. As a result, elastic deformation is reversible and non-permanent. The chemical notion of “elasticity” best describes elastic deformation. Elasticity is a substance’s capacity to return to its original condition after being deformed. Elastic deformation is mostly determined by the chemical bonding of the material.

Materials with suitable elasticity can absorb and distribute impact forces, contributing to a safer and smoother ride. Common materials like steel and aluminium alloys are chosen for car chassis due to their balanced elastic properties

1.1.5.2 Plastic Behaviour

Plastic deformation is defined as the persistent deformation or change in the shape of a solid body caused by a sustained force. This happens when a great amount of tension is applied to a material. Plastic deformation is permanent and irreversible. Plasticity is the ability to be permanently formed or moulded.

Metal plasticity refers to the ability of certain metals, particularly advanced high-strength steels (AHSS), to undergo significant plastic deformation before failure. These materials, including dual-phase (DP) steel, complex phase (CP) steel, and lightweight steel with induced plasticity (L-IP), offer a combination of strength, formability, and weight reduction for car chassis

applications. Steel, especially AHSS, is a common choice due to its desirable mechanical properties and formability.

1.1.6 Plasticity Models

There are many different plasticity models that have been developed and that are available in finite element software. In practice, the different models can be divided into two groups: Isotropic hardening and Kinematic hardening.

The isotropic hardening accounts for the change in size of the yield surface. For instance, if one loads a specimen in uniaxial tension beyond the yield stress, then unloads and reloads it in uniaxial compression, the new yield stress in compression will be equal in magnitude to the new yield stress in tension, that is, the yield surface has expanded as shown in Figure 1.1 (a). The isotropic hardening plasticity models can provide accurate predictions all the way to failure (under monotonic loading).

The kinematic hardening, on the other hand, accounts for the translation of the yield surface in the deviatoric stress space as shown in Figure 1.1 (b). For instance, if one loads a specimen beyond the yield stress in uniaxial tension, then unloads and reloads it in uniaxial compression, the new yield stress point in compression is going to be smaller in magnitude than the original one. This is known as the Bauschinger effect. This type of hardening causes plastic anisotropy in the material behaviour. The kinematic hardening models are often based on non-linear equations with material parameters that need to be determined from experimental tests, and hence are often more difficult to calibrate [5].

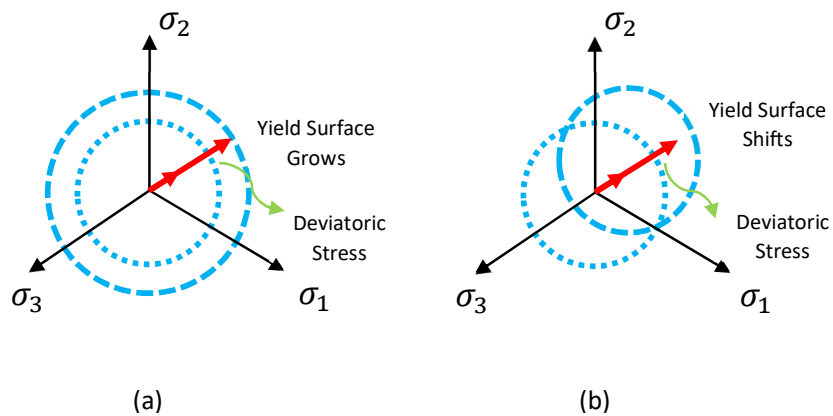


Figure 1.1. Schematic representation of the Yield Surface in the deviatoric stress space for (a) Isotropic Hardening and (b) Kinematic Hardening

1.1.6.1 Chaboche Nonlinear Kinematic Hardening Model

The Chaboche nonlinear kinematic hardening model is a constitutive material model used in the field of mechanical engineering and materials science to describe the behaviour of materials subjected to cyclic loading. This model is particularly relevant in the study of fatigue and durability of materials under varying mechanical loads. Proposed by Chaboche and his co-workers, this model is based on a decomposition of non-linear kinematic hardening rule proposed by Armstrong and Frederick [6]. This decomposition is significant in better describing the three critical segments of a stable hysteresis curve. These three segments are:

- the initial modulus when yielding starts,
- the nonlinear transition of the hysteresis curve after yielding starts until the curve becomes linear again,
- the linear segment of the curve in the range of higher strain.

The Chaboche model considers the nonlinear relationship between stress and strain during cyclic loading. It considers the accumulation of plastic strain over multiple loading cycles. The Chaboche nonlinear kinematic hardening model is commonly used in numerical simulations and finite element analysis (FEA) to predict the behaviour of materials subjected to complex loading conditions, such as those encountered in structural components of machinery, aerospace, and automotive industries.

1.1.7 Finite Element Analysis on Vehicular Frame

FEA is a general numerical method where we can solve complex geometrical models by dividing them into simpler, easy to comprehend parts that are called finite elements. This process of dividing and breaking up the system is done by space discretization, generating the mesh of the object. This develops a finite number of points or nodes which acts as numerical domain for the analysis. These nodes are assigned with their algebraic equations which are later grouped into a large system of equations and solved for the entire model. In modern age, one cannot do without FEA to design structures. In this study, we have used the following types of Structural Analyses.

1.1.7.1 Static Analysis

A static structural analysis determines the effect of steady (or static) loading conditions on a structure, while omitting inertia and damping effects, such as those caused by time varying

loads. These are the most common analyses performed for verification and/or validation but do not indicate that they are always simple in nature. Significant performance insight into a component and/or assembly can be obtained from a static simulation.

1.1.7.1.1 Linear Static Analysis

A linear static analysis is an analysis where a linear relation holds between applied forces and displacements. In practice, this is applicable to structural problems where stresses remain in the linear elastic range of the used material. In a linear static analysis, the model's stiffness matrix is constant, and the solving process is shorter when compared to a nonlinear analysis on the same model. Therefore, a linear static analysis is often used prior to performing a full nonlinear analysis. The matrix form of linear static analysis [7] is given by Eqn. 1.1.

$$[K]\{u\} = \{F\} \quad 1.1$$

In the automotive industry, linear static analysis is utilized to assess the stress, deformation, and strain distribution in critical components. It helps engineers predict structural integrity, optimize designs, and prevent failures. By simulating different scenarios, linear static analysis assists in streamlining vehicle aerodynamics, improving fuel efficiency, and enhancing overall performance.

1.1.7.1.2 Nonlinear analysis

A nonlinear analysis is an analysis where a nonlinear relation holds between applied forces and displacements. Nonlinear effects can originate from geometrical nonlinearity's (i.e., large deformations), material nonlinearity's (i.e., elasto-plastic material), and contact. These effects result in a stiffness matrix which is not constant during the load application. This is opposed to the linear static analysis, where the stiffness matrix remained constant. The source of this nonlinearity can be attributed to multiple system properties, for example, materials, geometry, nonlinear loading, and constraints [8]. Non-linear static analysis plays a vital role in evaluating the structural behaviour of vehicles. Unlike linear analysis, which assumes a linear relationship between forces and displacements, non-linear analysis considers changes in stiffness, material behaviour, and large displacements.

Geometric Nonlinearity - In analyses involving geometric nonlinearity, changes in geometry as the structure deforms are considered in formulating the constitutive and equilibrium equations. Many engineering applications such as metal forming, tire analysis, and medical

device analysis require the use of large deformation analysis based on geometric nonlinearity. Small deformation analysis based on geometric nonlinearity is required for some applications, like analysis involving cables, arches, and shells.

Material Nonlinearity - Material nonlinearity involves the nonlinear behavior of a material based on a current deformation, deformation history, rate of deformation, temperature, pressure, and others. Examples of nonlinear material models are large strain (visco) elasto-plasticity and hyperelasticity (rubber and plastic materials).

1.1.7.2 Transient Analysis

In the context of Finite Element Analysis (FEA), transient analysis refers to a simulation technique that evaluates the time-dependent behavior of a physical system or structure subjected to varying loads, boundary conditions, or initial conditions over a specific time interval. It involves solving a set of equations at discrete time steps to understand how the system's response evolves over time. The matrix form of the analysis is given by Eqn. 1.2.

$$[M]\{\ddot{u}\} + [C]\{\dot{u}\} + [K]\{u\} = \{F(t)\} \quad 1.2$$

The Newmark method is a widely used numerical technique for conducting transient analysis in structural engineering and dynamics. It is used to simulate the time-dependent behavior of structures under varying loading conditions. This method involves integrating the equations of motion to predict the response of the system over time. It provides an efficient and stable way to analyze dynamic systems, such as impact analysis. The Newmark method's accuracy and stability make it suitable for simulating wave propagation and other complex transient phenomena [9]. The semi-discrete equation of motion given by Eqn. 1.3.

$$[M]\{\ddot{u}_{n+1}\} + [C]\{\dot{u}_{n+1}\} + [K]\{u_{n+1}\} = \{F(t_{n+1})\} \quad 1.3$$

The Newmark family of time integration algorithms requires the displacement and velocity to be updated which is given by Eqn. 1.4 and 1.5.

$$\{\dot{u}_{n+1}\} = \{\dot{u}_n\} + [(1 - \delta)\{\dot{u}_n\} + \delta\{\ddot{u}_{n+1}\}]\Delta t \quad 1.4$$

$$\{u_{n+1}\} = \{u_n\} + \{\dot{u}_n\}\Delta t + \left[\left(\frac{1}{2} - \alpha\right)\{\ddot{u}_n\} + \alpha\{\ddot{u}_{n+1}\}\right]\Delta t^2 \quad 1.5$$

Where α and δ are Newmark's integration parameters.

Thus, the Newmark family of time integration algorithms can be determined by the Newmark integration parameters. In the end, the Newmark integration scheme consists of the three finite difference equations presented in Eqn. 1.3 through Eqn. 1.5, and the three unknowns $\{\ddot{u}_{n+1}\}$, $\{\dot{u}_{n+1}\}$, and $\{u_{n+1}\}$ can be numerically calculated by the three algebraic equations along with the three known quantities $\{\ddot{u}_n\}$, $\{\dot{u}_n\}$, and $\{u_n\}$.

Transient static analysis plays a crucial role in assessing the dynamic behaviour of vehicles under varying time-dependent loads. It involves simulating the response of a vehicle's structure to forces such as impacts, crashes, and other transient events. By considering factors like impact forces, stress distribution, and deformations, transient analysis aids in optimizing vehicle designs for safety, performance, and durability. It enables engineers to refine designs, improve under hood and underbody packaging, and ensure that vehicles meet safety standards. Transient analysis thus contributes significantly to enhancing vehicle performance and occupant safety.

1.1.8 Damping and its Sources

Damping refers to the process of reducing or preventing the oscillation of an oscillatory system by dissipating the energy stored in the oscillation. It is an influence that decreases the amplitude of mechanical or electrical waves over time. Damping is essential for controlling vibratory motion, reducing noise, and stabilizing systems.

1.1.8.1 Viscoplasticity

Damping due to viscoplasticity refers to the energy dissipation that occurs in a material or structure under cyclic loading as a result of both viscous and plastic deformation mechanisms. Viscoplastic damping is particularly relevant in the context of structural dynamics, where materials exhibit both viscous and plastic behavior, resulting in energy dissipation through internal friction and irreversible deformation.

1.1.8.2 Contact Damping

In the context of finite element analysis, software like ANSYS offers the concept of contact damping, which can be defined between interacting surfaces to simulate viscous damping effects. This is particularly useful in simulations where mechanical contact analysis is involved. The damping model defines forces that resist relative motion between contacting surfaces, aiding in the accurate representation of real-world behaviors.

1.1.8.3 Material Damping

Various mathematical models and experimental techniques are used to quantify and analyze material damping. This damping property is crucial in designing structures that can withstand vibrations and dynamic loads effectively. In engineering simulations, material damping is considered in finite element analysis to accurately predict dynamic responses of structures [10].

1.1.8.4 Stabilization Damping

Stabilization damping is a technique used in finite element analysis (FEA) simulations to enhance the convergence and stability of nonlinear solutions, particularly in contact problems. It involves introducing a damping force that helps control rigid body motions and oscillations during simulations. The method is crucial in preventing convergence difficulties caused by force imbalances and high deflections.

1.2 Literature Review

According to MORTH (Ministry of Road Transport & Highways), India is home to the second largest road network and witnessed 151,113 road deaths in the year 2019, which roughly translates to 11% of Global Road accident fatalities. This was accompanied by 4,51,361 injuries according to the MoRTH 2019 Annual Report [11 - 12]. The 2020 Annual report states that the worst affected group in road accidents is the 18-45 years age group accounting for a massive 70% of the total accidental fatalities [13]. The social cost of road traffic accidents in India was estimated at 3% of the country's GDP in the year 2000 [14]. This value was revised to 0.77% for the year 2018 as per the study commissioned by MoRTH along with the Indian Institute of Technology (IIT), Delhi, and Delhi Integrated Multi-Modal Transport System (DIMTS) [15]. The estimation was made using the regression Eqn. 1.6 provided in by the International Road Assessment Programme (iRAP) [16].

$$\log_n(\text{VSL}) = 3.015 + 1.125 \log_n(\text{GDP}) \quad 1.6$$

1.2.1 FEA and Vehicular Rollover

Over the past few decades, Finite Element simulations have extensively been performed for frontal, side, and rear impact collisions but less emphasis is given to scenarios where the roof gets crushed. Some of the studies have used FEA to simulate rollover crashes, optimize vehicle

structures, and comply with safety standards, such as the UN ECE R66 standard for bus rollover tests [17]. Vehicular Rollover is the only scenario where the roof strength is judged, and it is by far the largest contributor to passenger casualties as the passenger headroom gets compromised [18]. A structurally weak roof will lead to a greater reduction in cabin headroom which in turn increases the risk of fatal head injuries [19]. On analysing the data from the NASS-CDS (National Automotive Sampling System–Crashworthiness Data System), Burns et al.[20] concluded that a substantial percentage of SCI (Spinal Cord Injuries) can be prevented if the roof intrusion is restricted to 15 cm. The National Highway Traffic Safety Administration (NHTSA) has formulated several regulations for designing and manufacturing automobiles. According to the FMVSS (Federal Motor Vehicle Safety Standards) No. 216, the roof of a car having a Gross Vehicle Weight Rating (GVWR) of 4563 kg or less should be able to withstand an applied force equal to 2.5 times of the unloaded car weight [21]. A study conducted by Mao et al. [22] shows that the static roof crush tests (FMVSS No. 216) cannot determine the strength of the pillars as effectively as the inverted drop test.

1.2.2 Scenarios with heavy impact on Vehicle Roof

A similar test of the roof strength occurs when a whole tree trunk falls on a car. In a rollover accident, the roof gets crushed under the impact of the car's own weight. When a tree trunk falls, the consequences of a heavy external weight impacting the car roof can be seen. Several cases have been reported by trusted news agencies where the roof of the car crumbled after being impacted by a roadside tree [23]. In such cases, the passengers sustained serious injuries which sometimes proved to be fatal [24]–[26].

1.2.3 Parameters for Modelling the Trunk and Car Frame

Extensive crash studies conducted by major OEMs are not only expensive but also time consuming, so the results are not publicly available. Most of the studies on production car models are sponsored by the companies themselves and the contents aren't readily available. The simulations in the present study were conducted on the tubular frame chassis of a NASCAR car [27]. As for the tree trunk, field studies in Bengaluru conducted by Nagendra et al. [28] between November 2007 and April 2008, provided the necessary parameters. The average height of street side trees was found to be 9.7 meters with an average DBH (Diameter at breast height) of 39 cm. Roadside plantations typically have an average density of 0.57 g/cm³ [29]. The green weight (W_{sat}) of 5 cm long samples of wood at maximum moisture level was

noted. After oven drying them at 102°C, the dry weight (W_{dry}) was also recorded. Finally, the specific gravity of the samples was calculated using Eqn. 1.7.

$$\text{Specific Gravity} = \left[\frac{W_{\text{sat}} - W_{\text{dry}}}{W_{\text{dry}}} + 0.6536 \right] \quad 1.7$$

1.2.4 Materials for the Car Frame

The car body-in-white (BIW), is a crucial aspect of automotive design and manufacturing. The choice of materials directly impacts a car's performance, safety, and production cost. Several materials are commonly used which include Steel, Aluminium, Mixed Materials, and Plastics.

The choice of material depends on factors like cost, safety regulations, performance, and market positioning. Steel is often preferred for cost-effective mass production, while aluminium and composites are chosen for lightweight and high-performance applications. Advances in material science continue to drive innovation in car body design, with a focus on reducing weight to improve fuel efficiency and environmental impact [30].

In a car frame, diverse types of steel are utilized to deliver a balance of cost and crashworthiness. The superior energy absorbing ability of steel makes it the most viable option when it comes to manufacturing automobile chassis. In a vehicular crash, the safety of the passengers depends on the amount of the impact force absorbed by the car frame itself. Greater the energy absorbed, lesser is the impact experienced by the passengers [31]. Apart from the new, high strength materials like different grades of DP (Dual Phase) -, TRIP (Transformation Induced Plasticity) - and TWIP (Twinning-Induced Plasticity) -steels, Press Hardening Steels (PHS) are also a popular for their application in producing high strength structural body elements (e.g., A and B-Pillars, etc.) [32]. By using manganese boron steel 22MnB5, it has been possible to achieve strengths greater than 1500 MPa during press quenching. However, new processing alternatives and materials with further increased strength or increased part ductility and new heating technologies are constantly appearing on the scene [33].

Different grades of HSS (High-Strength Steel) are the most preferred materials for their impressive structural strength. UHSS (Ultra High-Strength Steel) and AHSS (Advanced High-Strength Steel) together have the highest weight share in a car BIW (Body in White) [34]–[37]. The nomenclature “AHSS” refers to dual phase (DP), transformation induced plasticity

(TRIP), complex phase (CP) and martensitic (M) steels with yield strength above 300 MPa and tensile strength above 600 MPa. Despite their strength, most AHSS, with the exception of the martensitic steels, have a superior formability resulting from a high work hardening rate [38].

1.2.5 Modelling Plasticity of the Car Frame

As discussed earlier in section 1.1.6, there are many different plasticity models that have been developed and that are available in finite element software. This section discusses about the available literatures on Isotropic and Kinematic Hardening Models.

1.2.5.1 Isotropic Hardening Model

Isotropic hardening is related to the accumulated dislocation structure and expands the yield surface of a material under plastic deformation. The evolution law for isotropic hardening [39] takes the form given in Eqn. 1.8 where b and Q are material parameters. This equation describes a hardening behaviour that starts from zero but levels off as deformation progresses.

$$\dot{R} = b(Q - R)\dot{\epsilon}_p \quad 1.8$$

The value of b is normally between 0.5 and 1 and is related to the speed for R to saturate. On the other hand, the value of Q represents the level of saturation [40]. The direct relationship between R and ϵ_p can be obtained after integration which is given by Eqn. 1.9.

$$R = Q(1 - e^{-b\epsilon_p}) \quad 1.9$$

Isotropic hardening is suitable for large strain, proportional loading situations. Proportional loading refers to loading scenarios when the orientation of the principal stresses does not change during the course of loading. Isotropic hardening is not suitable for cyclic loading applications [41].

1.2.5.2 Chaboche Kinematic Hardening Model

For rate-independent plasticity, Chaboche [42] defined an elasticity domain given by Eqn. 1.10 where X accounts for the kinematic hardening.

$$f = |\sigma - X| - k + R \leq 0 \quad 1.10$$

The hardening equation for monotonic uniaxial loading tests can be obtained using e Eqn. 1.11 where k is the yield strength at zero plasticity and R represents the isotropic hardening factor.

$$\sigma = k + R + \sum_{i=1}^M \frac{C_i}{\gamma_i} (1 - e^{-\gamma_i \varepsilon_p}) \quad 1.11$$

The value of R can be neglected as we will be studying a case of sudden impact. The yield strength is a constant and Eqn. 1.11 can be further simplified to consider only the back stress. This is represented by Eqn. 1.12 which is the non-linear kinematic hardening rule [43].

$$X = \sum_{i=1}^M \frac{C_i}{\gamma_i} (1 - e^{-\gamma_i \varepsilon_p}) \quad 1.12$$

1.2.6 Formulation for the Dynamic Analysis of the Car Structure

1.2.6.1 Structural Properties of Car Suspension

To make the arrangement as realistic as possible, proper boundary conditions and relevant data is needed. The movement of the car in the rectilinear directions must be constrained in such a way that the road friction can be replicated. The coefficient of friction between the tyre and the road was estimated to be between 0.7 and 0.9 [44], [45]. The whole weight of a car body is primarily supported by the wheel and suspension system. With the idea of a passenger car in mind, two stiffnesses must be decided.

- The stiffness offered by the car tires.
- The stiffness offered by the suspensions.

The values of tyre and suspension stiffness obtained across literatures are listed in Table 1.1.

Tyre Stiffness (kN/m)	Suspension Stiffness (kN/m)	Reference
205 - 245	24.2 – 28.4	J. A. Calvo et al. [46]
200	41.73 – 78.16	Anil Shirahatt et al [47]
180	-	Mahmood M. et al. [48]

Table 1.1. Tyre and Suspension Stiffness values

1.2.6.2 Effects of Damping on the Dynamics of the Car

Passenger cars must provide a smooth and comfortable riding experience with the help of proper damping. In a spring-damper system, the value of the damping ratio determines the rate at which the damper dissipates the energy. According to G. Ślaski [49], the damping ratio of a passenger car can vary between 0.2 and 0.8 depending on the road conditions. A lower damping ratio provides superior ride comfort but compromises on vehicle handling. On the other hand, a high value signifies better vehicle control but compromises on comfort. J. A. Calvo et al. [46] reported that the damping ratio of a car typically varies from 0.2 to 0.4 which can be further reduced to a range of 0.2 – 0.25 for better comfort. In a study conducted by Guruguntla et al. [50], revealed that seated occupants perceive maximum vibration in the 3–6 Hz frequency range. The ride comfort depends on the characteristics of the forces that cause oscillations and vibrations, on the design of the car, the parameters of the suspension, the driving conditions etc.

1.2.6.3 Rayleigh Damping for the frame structure

In a dynamic analysis, the material damping needs to be considered. In ANSYS Mechanical, material damping can be administered to the simulation with the help of Rayleigh damping.

The Rayleigh damping model approximates viscous damping available in Harmonic and Dynamic FEA simulations. It allows modelling the energy dissipation in the material due to internal friction, assuming it is proportional to the strain or deformation rate [51]. The system equation is given by equation (1.2). The damping effect of the Rayleigh damping is controlled by two parameters: α and β . The viscous damping matrix $[C]$ is given by the Eqn. 1.13.

$$[C] = \alpha[K] + \beta[M] \quad 1.13$$

For $\beta = 0$, α is given by Eqn. 1.14 and for $\alpha = 0$, β is given by Eqn. 1.15.

$$\alpha = \frac{2\zeta}{\omega_n} \quad 1.14$$

$$\beta = 2\zeta\omega_n \quad 1.15$$

Table 1.2 lists the values of Rayleigh damping found across various literatures.

Type of Structure	β	α	Reference
Rectangular SFT	0.946	2.2×10^{-4}	M. H. Rahman et al. [52]
Train Sleeper	8.52	0	André Paixão et al. [53]
Gear	7.1×10^{-4}	1.4×10^{-7}	A Kahraman et al. [54]
Crane	0.4424	1.165×10^{-2}	S Hajdu et al. [55]

Table 1.2. Values of Rayleigh Damping Coefficients

1.3 Scope of Work

When looking at past papers, most of the work till date is centred around frontal, side, and rollover crash scenarios [17]. Comparatively less emphasis was given to scenarios where the structural integrity of the Roof gets compromised. A standard static structural test parameter for the Roof like the FMVSS No. 216 is unable to clearly replicate a rollover crash [22]. In a rollover accident, the roof gets crushed under the impact of the car's own weight. Whereas the impact of a freely falling tree trunk might lead to more serious accidents depending on height from which it falls.

The material for the Car Frame has to be selected based on its intrinsic properties. The material should also have a good energy absorbing ability for better crashworthiness. Over the years, different types and grades of steel has become the standard choice for such application [32 - 38]. They provide impressive structural strength whilst having superior formability as a result of high work hardening rate. Three material variants considered for this study were:-

- Two variants of UHSS [37] – (i) Baseline sample, (ii) Welded Sample
- One variant of AHSS [34] – DP 350/600

For the Tree trunk, survey data of road side plantations are available for cities. This can be used to estimate the average dimensions and density of Trees [28 - 29].

The plastic behaviour also needs to be depicted accurately based on the Hardening models available in ANSYS. Considering rate-Independent plasticity, the plastic strains were assumed to develop instantaneously while not being a function of time. This is a reasonable assumption

for the bulk of engineering problems. Two types of Models are available namely, Isotropic Hardening [39 -41] and Kinematic Hardening [42 - 43].

The parameters of the suspension and car frame material damping can be determined from past research [46 - 55] and optimized to be in line with this study. Different time dependent and independent analyses can be performed to study the maximum deformation, maximum stress, maximum plastic strain, and over the time behaviour of the different forces acting on the car frame.

1.4 Objectives

This study approaches with the following objectives.

1. Analyse the phenomenon when the trunk of a tree freely falls on a car parked below it.
2. Quasi-Static Analysis of a falling tree trunk on the roof of a car.
3. Dynamic Analysis of the freely falling tree trunk for a release height variation from 0 m to 10 m.
4. Studying the effect of Dynamic loading with the variation of the height of free fall.
5. Observing the effect of material variation in the car frame.
6. Comparison between the static analysis and the transient analysis results in establishing a probable relation between them.
7. Study the variance of the forces acting on the car frame.

Chapter 2: Methodology

The simulations in the present study were conducted on the tubular frame chassis of a NASCAR car [27]. The car frame model used is primarily modified using ANSYS SpaceClaim keeping the main load bearing components intact. A roof surface was added to the model to replicate an actual car frame as shown in Figure 2.1. From the original file, all solid bodies were converted into surface bodies using the surface “extraction tool” of SpaceClaim. The imperfections which resulted from the surface extraction were manually corrected. Multiple bodies which were parts of the same structure were attached together with the help of the “combine tool”. Using only surface bodies substantially reduced the computational cost. Furthermore, the shell bodies as shown in Figure 2.1 were comprised of hollow cylindrical pipes which helped in reducing the overall mesh count.

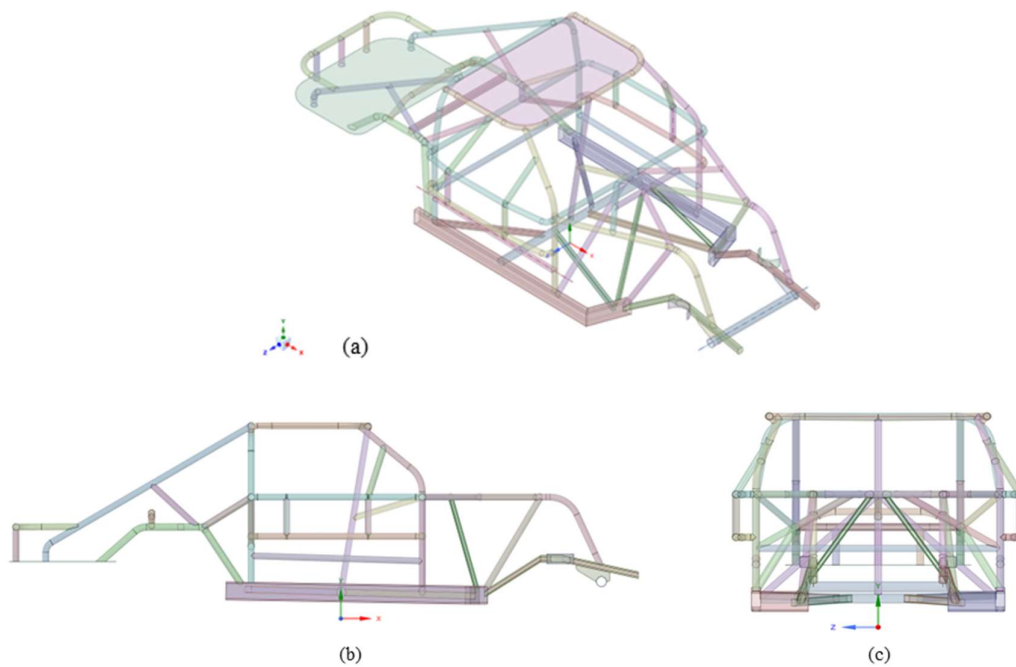


Figure 2.1. (a) Isometric view, (b) Side view, and (c) Front view of the Car Frame

2.1 Car Frame Meshing and Contact Preparation

In finite element analysis (FEA) as the geometry, or spatial domain, is meshed more finely convergence occurs, which means arriving nearest to the true solution. Mesh convergence involves choosing an optimal mesh by running multiple simulations with different levels of

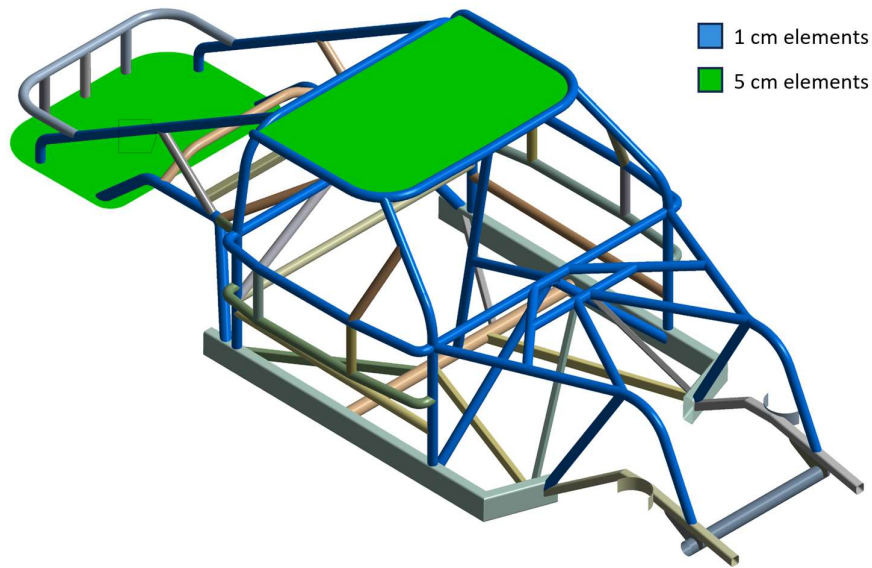
fine/coarse mesh, reducing the element size, and calculating the result of this process on the accuracy of the solution. Typically, as the mesh size is reduced, the solution becomes more accurate as the performance of the critical point of the product is finely analysed across its spatial domain. But to attain a more accurate result, longer runtime is required, and complexity of the process is also increased. Keeping theses in mind, a particular size of meshing was chosen for the analysis. A default mesh size of 1.75 cm was used. A set of three different mesh sizes were tested. Each set consisted of a different face sizing (m_f) and body sizing (m_b) to control the total number of elements. The Face sizing was used to vary the mesh layout of the flat surfaces whereas, the body sizing was used to alter the mesh distribution of the cylindrical parts. The Mesh Independence study was conducted using a transient structural analysis where the tree trunk fell from 0 m height and UHSS – Heat Treated was the material used. The results of the study are listed in Table 2.1 showing the variance of the Maximum Equivalent Stress (σ_{eq}^{max}) for different mesh sizes.

Face & Edge Sizing	Total Element Count	Total Node Count	σ_{eq}^{max} (Mpa)	Diff. (%)
$m_f = 7.5$ cm, $m_b = 1.25$ cm	43,418	43,812	186.31	-8.26 %
$m_f = 5$ cm, $m_b = 1$ cm	59,735	60,128	203.08	-
$m_f = 2.5$ cm, $m_b = 0.75$ cm	96,733	97,227	205.44	+1.16 %

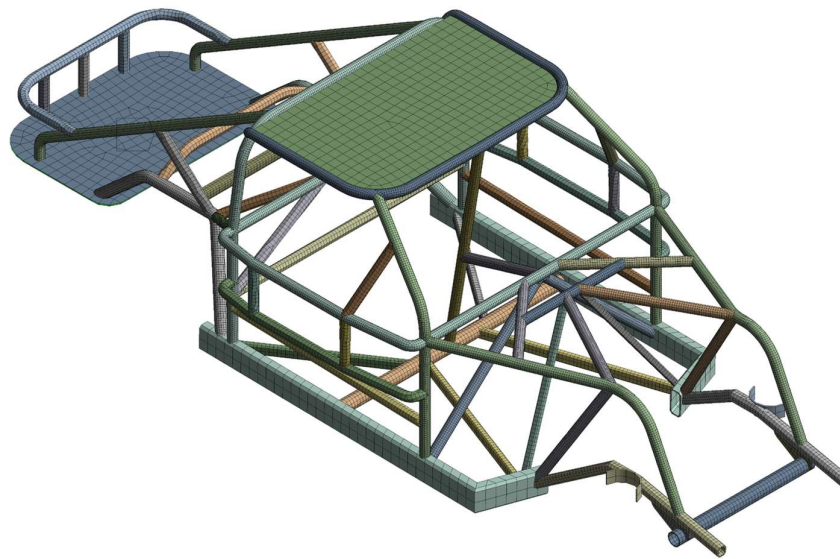
Table 2.1. Variance of the Maximum Equivalent Stress (σ_{eq}^{max}) for different mesh sizes.

The car frame was meshed with lower order shell elements having a default mesh size of 1.75 cm. In Figure 2.2 (a), the parts which are red in colour have a reduced mesh size of 1 cm and the green surface parts have a default mesh size of 5 cm. The use of 1 cm mesh sizing helped in accurately capturing the curvature of the cylindrical bodies with a smooth mesh layout. Moreover, the parts assumed to be the main load bearing path are coloured blue and thus have

a reduced mesh size. The mesh which was generated using the above settings had a total element count of 59,735 elements and a node count of 60,128 as shown in Figure 2.2 (b).



(a)



(b)

Figure 2.2. Isometric view of (a) highlighted components with different mesh size, (b) Meshed Car Frame showing the layout.

All the connections between adjacent parts were set as bonded pairs. The connections were auto generated with a tolerance of 1.65 cm by setting the “tolerance slider” with a value of -18. The “tolerance slider” has a maximum limiting value of 100 and a minimum of -100. Rest of

the settings are shown in Figure 2.3. Using these settings, a total of 125 active connections were generated as shown in Figure 2.4.

Tolerance	
Tolerance Type	Slider
Tolerance Slider	-18
Tolerance Value	1.6545 e-002 m
Use Range	No
Face/Face	No
Face/Edge	Yes
Edge Overlap Tolerance	Off
Edge/Edge	No
Priority	Include All
Group By	Bodies
Search Across	Bodies
Statistics	
Connections	125
Active Connections	125

Figure 2.3. Different settings used for generating contacts.

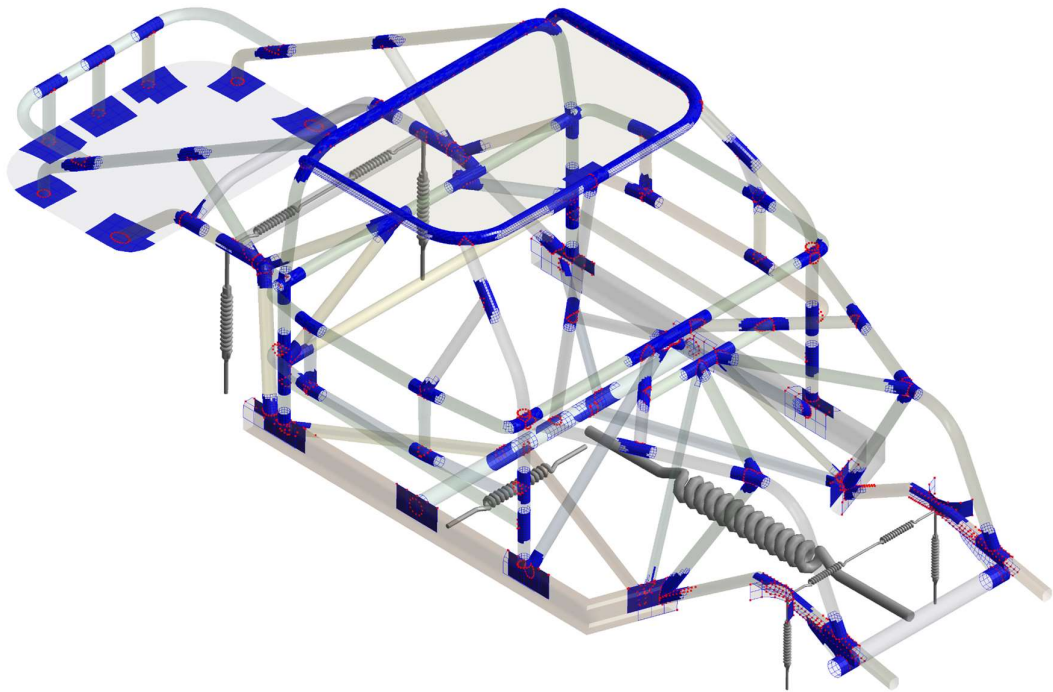


Figure 2.4. Isometric view of all the generated bonded contacts.

2.2 Preparation of the Tree Trunk (Modelling and Meshing)

The tree trunk was designed measuring 1.5 m in height and 0.4 m in diameter. The trunk is meshed by dividing it into 40 elements along the circumferential edge and 50 elements along the height as shown in Figure 3.5. To add bias to the trunk mesh properly, the log was divided into two equal sections along the plane passing through AA' as shown. Along the circumference of the log, a smooth transition type bias with a growth rate of 1.2 was provided. The same was done for the height but with a growth rate of 10.0. The significance of providing a bias lies in the fact that the elements which will encounter the rim of the roof will be smaller in size. This will help in better contact detection and more accurate results. Moreover, using bias helps us to reduce the overall mesh size as we can now obtain comparable results with a smaller mesh and a reduced computation time.

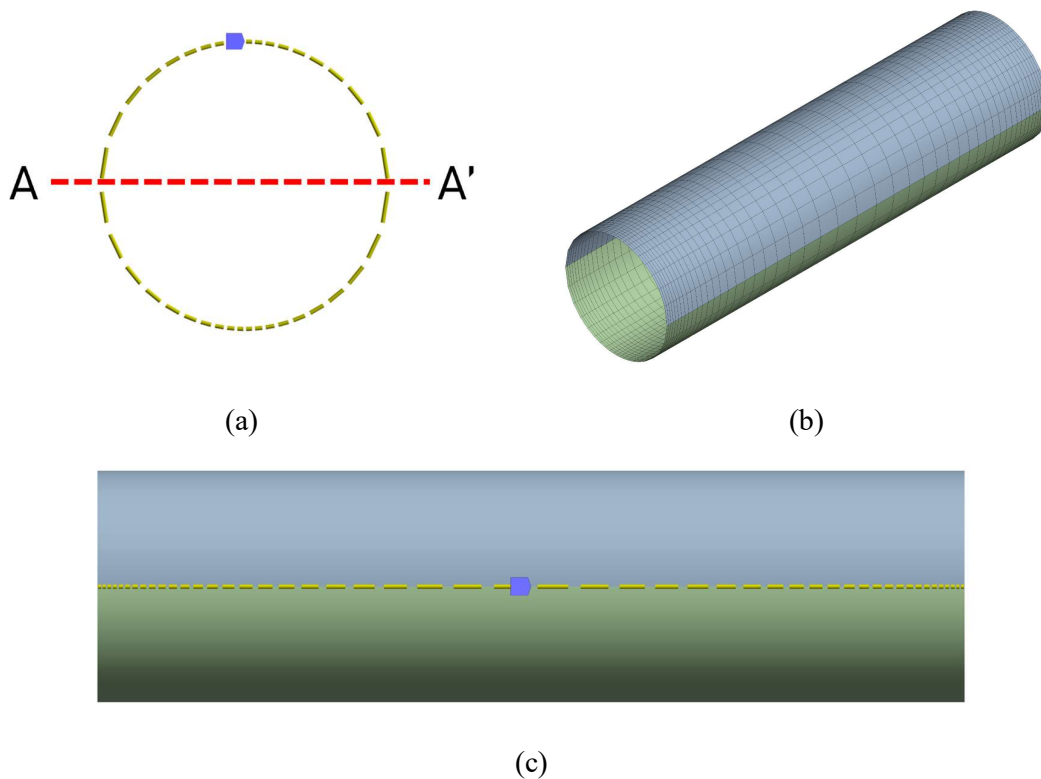


Figure 2.5. (a) Plane of separation (AA') with the circumferential bias (b) Isometric view of the meshed tree trunk (c) Side view of the trunk showing the longitudinal bias.

The tree trunk has 2000 elements in total with a node count of 2142. The element order was set to Linear with a default mesh size of 12.13 cm.

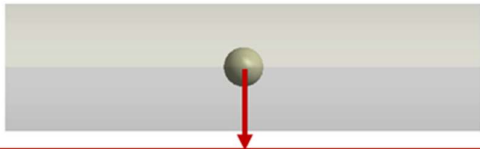
This alternative method used to design the tree trunk helps us solve and optimize a couple of problems. As depicted in Figure 2.5, instead of using a solid cylindrical block, we opted for a cylindrical surface. We also omitted the flat faces on both sides of the trunk to reduce the overall surface area of the model. By doing this, we could then use surface elements instead of solid ones with a sizable reduction to the mesh count. The flat faces would have had no interaction with the car frame, so their omission does not affect the results. On the downside, we neglected the damage to the tree trunk because of the impact. As a trunk would relatively behave as a rigid mass, this was a calculated assumption so that we could potentially save some computation power to observe the changes in the car frame.

2.3 Preparation of the Combined Model

The meshed files of the car frame and the tree trunk were created separately and a .cdb file was generated for each of them using the command,

```
cdwr, all, filename, cdb
```

Both generated cdb files were imported in a separate workbench file using the external model tool. After importing, the setting “Check Valid Blocked CDB File” needed to be turned off so that workbench can read the files. The trunk is designed as a thin cylindrical surface with an exceedingly small thickness of 10^{-4} mm. To replicate the behaviour of a solid log of wood, a point mass is attached to it. After that the behaviour between the point mass and the log surface was set as Rigid. This specifies that a rigid constraint is added to the link connecting the mass and the surface preventing any deformation. The parameters required to define the point mass were calculated using a wood density of 570 kg/m^3 and the average dimensions of a roadside tree. The point mass along with its parameters are shown in Figure 2.6.



Mass	1074.4 kg
Mass Moment of Inertia X	211.61 kg.m ²
Mass Moment of Inertia Y	211.61 kg.m ²
Mass Moment of Inertia Z	21.367 kg.m ²

Figure 2.6. Side view of the point mass attached to the tree trunk along with its properties.

Two Rough contacts were added to the model as shown in Figure 2.7. These rough contacts helped to prevent the lateral sliding of the log along the X and Z directions.

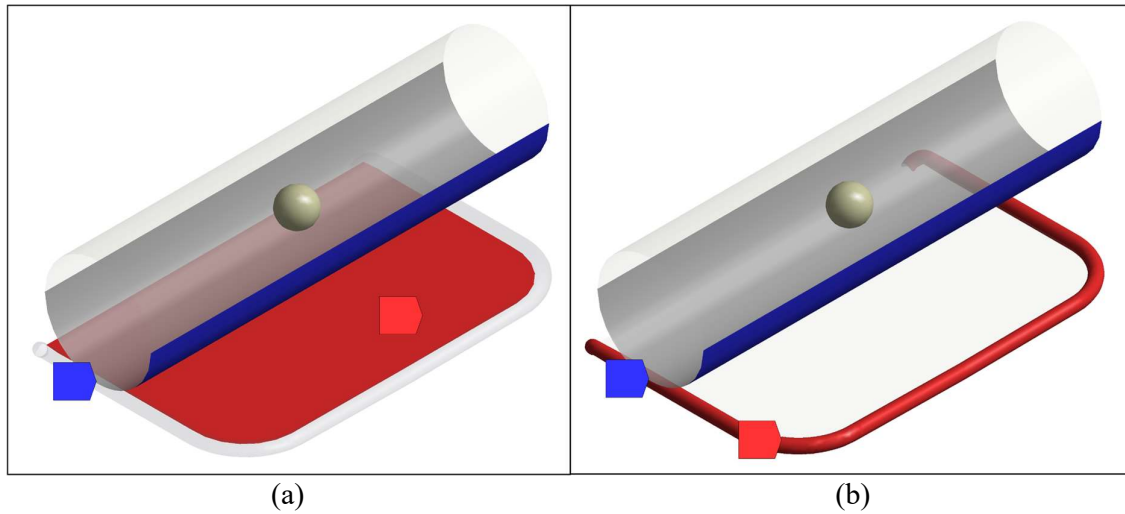


Figure 2.7. Isometric view of the rough contact between (a) the Roof Surface and the tree trunk, (b) the Roof Rim and the tree trunk

To overcome the convergence issues, the Normal Stiffness Factor for the contact shown in 3.7(a) was set as 10^{-2} and for 3.7(b), it was set as 10^{-4} . The formulation was also set to the Pure Penalty method. The rest of the setting were kept unaltered. For both contacts, the tree trunk was declared as the Target Body with the bottom surface being the Target Shell Face. Both the Roof Surface and the Roof Rim had their top surface declared as the Contact shell face.

The Pure Penalty formulation used in declaring the contacts provided better convergence when compared to the default Augmented Lagrange formulation. However, some penetration was observed which was neglected for being less than 1% when compared to the dimensions of the model. The total number of contact and target elements are listed in Table 2.2.

Parameters	Total Count
Contact Elements	6,265
Contact Nodes	6,422
Target Elements	1,000
Target Nodes	1,071

Table 2.2. Total count of the elements and nodes in the contact and target region.

2.4 Design & Implementation of Suspension and Support Springs

A total of 14 springs have been used to support the frame and provide the necessary boundary conditions. For modelling the suspensions, 8 springs have been used in pairs of 2 springs in each wheel suspension. This is done because damping cannot be added to a non-linear spring. In each pair, one spring has a initial stiffness of 24 kN/m with infinite stiffness at 50% compression with no damping given by Eqn. 2.1, while the other is a longitudinal spring with a damping coefficient of 1394.4 Ns/m using 2.2.

$$F = K_s \times u_s \times \ln\left(1 + \frac{u}{u_s}\right) \quad 2.1$$

$$C = 2\zeta\sqrt{M_c K_s} \quad 2.2$$

While modelling a non-linear spring in ANSYS, a tabular set of data must be added. Mechanical has a limit of 9 sets of data with the condition that it must be symmetrical in nature. The data obtained using Eqn. 2.1 is represented using the Spring Force vs. Spring Displacement plot in Figure 2.8.

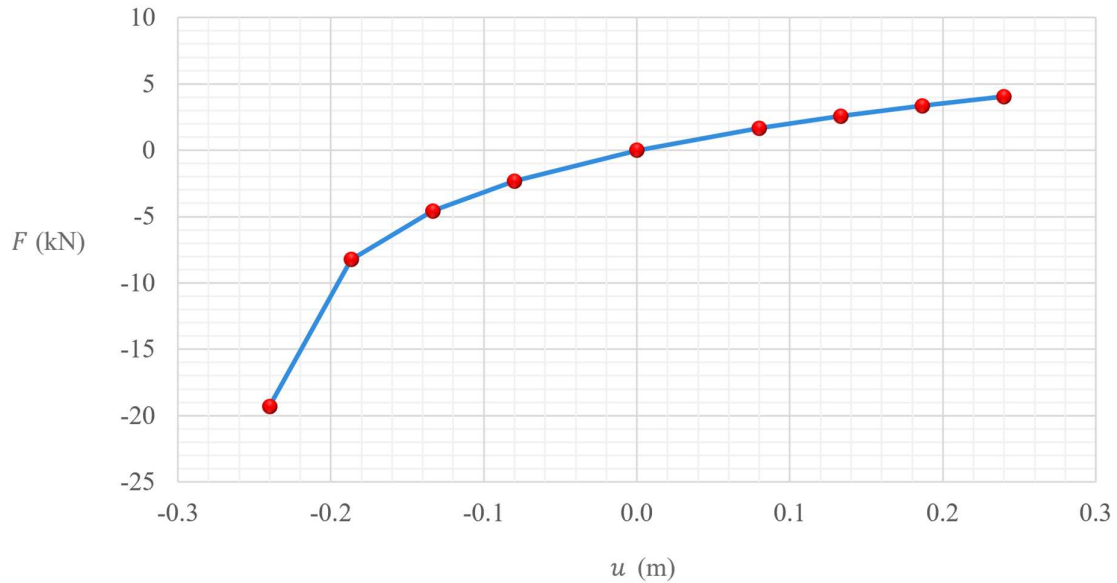


Figure 2.8. Spring Force vs. Suspension travel of the non-linear spring.

The damping coefficient was calculated by considering the parameters given in Table 2.3.

Parameters	Value considered
Stiffness assuming linear spring behaviour	24 kN/m
Damping Ratio	0.3
Quarter Car Mass	225 kg
Damping Coefficient	1,394 Ns/m

Table 2.3. Parameters used for the calculation of suspension damping.

The wheels have been replicated using 4 Torsional Springs of stiffness of 200 kNm/degree. The last two springs are used to prevent the linear motion in X and Z directions. Both springs have a spring stiffness of 8 kN/m (one-third of the suspension stiffness). The 8 suspension springs are attached to a single node rather than a whole part. While implementing the latter, we noticed that the link between the spring and the part which its scoped to, has rigid behaviour. This was preventing the scoped part from deforming leading to an unrealistic solution and so the single node approach was used. All the springs used are depicted in Figure 2.9.

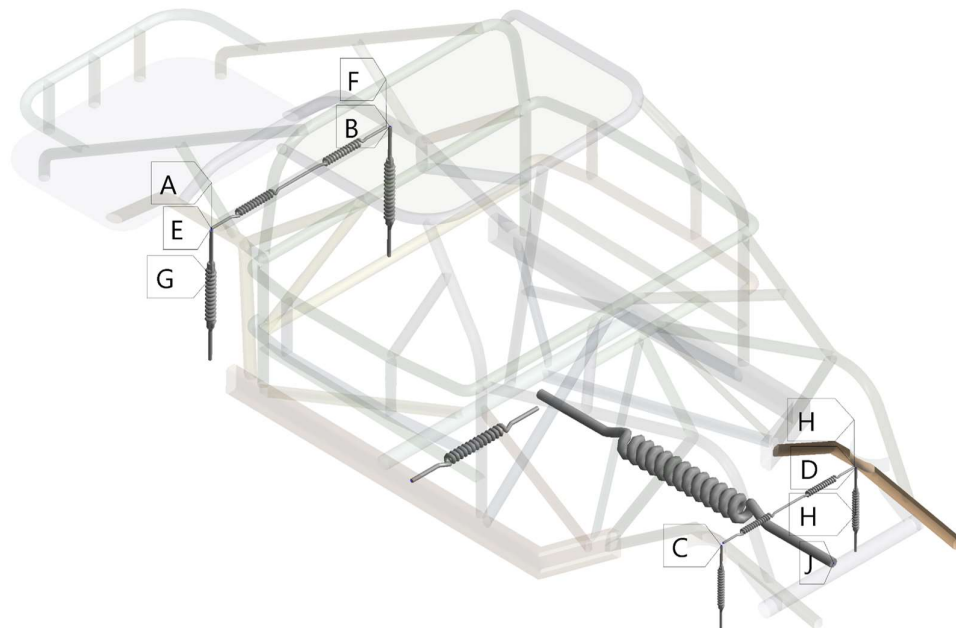


Figure 2.9. An isometric representation of all the 14 springs utilized to support the car frame.

2.5 Modelling Plasticity with Chaboche Kinematic Hardening Model

The plasticity of the car frame material is modelled using the Chaboche Kinematic Hardening model using two sets of Chaboche parameters using equation. After obtaining the engineering stress-strain curves of UHSS and AHSS (DP 350/600), the data is extracted manually from the curves using a graph reader. From this data, we obtained the true stress-strain curve. The elastic zone was removed after finding out the point at which plasticity starts. The point identified is the yield point and the corresponding stress is the Yield Stress. After fitting the Yield point to the origin, we obtain the curve of the plastic region. The plastic strain (ϵ^p) is then calculated by subtracting the elastic strain from the true strain. In an analogous way, the back stress (σ) is obtained by subtracting the yield stress from the true stress. The relation between the Chaboche parameters and the back stress is given in Eqn. 2.3.

$$\sigma = \frac{C_1}{\gamma_1} (1 - e^{-\gamma_1 \epsilon^p}) + \frac{C_2}{\gamma_2} (1 - e^{-\gamma_2 \epsilon^p}) \quad 2.3$$

We used a curve fitting algorithm in MATLAB to find out the two pairs of Chaboche parameters. The code used for curve fitting is given below.

Main.m

```
global A n
loadA
n=length(A);
xmin=[0 0 0 0];
xmax=[1e5 800 1e4 400];
format shortg
u=rand(size(xmin));
[x ERMS]=fmincon(@fit,xmin.*u+(1-u).*xmax,[],[],[],[],xmin,xmax)
```

loadA.m

```
A = [% contains the plastic strain vs back stress values]
```

```

fit.m

function ERMS=fit(x)
global A n
C1=x(1);
y1=x(2);
C2=x(3);
y2=x(4);
B=C1/y1*(1-exp(-y1*A(:,1)))+C2/y2*(1-exp(-y2*A(:,1)));
ERMS=norm(B-A(:,2))/sqrt(n);
end

```

The values obtained are listed in Table 2.4 and their fit is graphically shown in Figure 2.10.

Parameters	UHSS Baseline	DP 350-600	UHSS (Heated)
C_1 (MPa)	12835	10865	57654
γ_1	185.32	170.23	520.94
C_2 (MPa)	10000	4943.4	2815.7
γ_2	62.742	16.68	14.796

Table 2.4. Chaboche Parameters for the three materials.

The Ultimate Tensile Strength (σ_{ut}) of the three materials was calculated using the principle of necking [56]. Necking will occur in uniaxial tension at a strain at which the slope of the true stress-strain curve is equal to the true stress (σ_N) at that particular strain. The mathematical representation of this statement is given by Eqn. 2.4.

$$\frac{d\sigma_N}{d\varepsilon_p} = \sigma_N \quad 2.4$$

The true stress (σ_N) is represented by the Eqn. 2.5.

$$\sigma_N = k + \sigma \quad 2.5$$

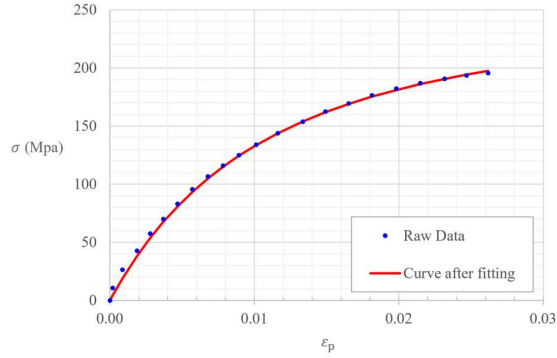
Finally, the Ultimate Tensile Strength (σ_{ut}) can be calculated using Eqn. 2.6.

$$\sigma_{ut} = \sigma_N e^{-\varepsilon_p} \quad 2.6$$

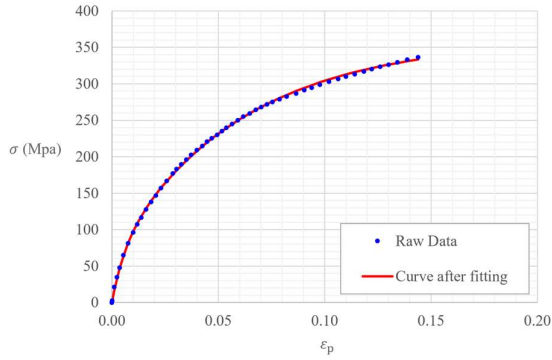
The values of σ_{ut} , k , and E for all the three materials are listed in Table 2.5.

Parameters	UHSS Baseline	DP 350-600	UHSS (Heated)
σ_{ut} (MPa)	1346.88	595.24	423.68
k (MPa)	1183.61	350.98	209.03
E (GPa)	104.41	125.53	152.28

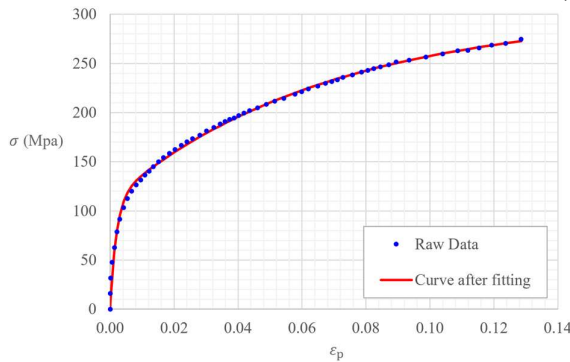
Table 2.5. Ultimate Tensile Strength (σ_{ut}), Yield Stress (k), and Young's Modulus (E) of the three materials, UHSS Baseline, DP 350-600, and UHSS (Heated).



(a)



(b)



(c)

C_1 (MPa)	12835
γ_1	185.32
C_2 (MPa)	10000
γ_2	62.742

C_1 (MPa)	10865
γ_1	170.23
C_2 (MPa)	4943.4
γ_2	16.68

C_1 (MPa)	57654
γ_1	520.94
C_2 (MPa)	2815.7
γ_2	14.796

Figure 2.10. Chaboche parameters comparison after fitting with the original data for material (a) UHSS Baseline, (b) DP 350-600, and (c) UHSS Heat Treated.

2.6 Pre-processing

The whole car frame was balanced on four suspensions. Naturally, all the four suspensions will have some initial compression to support the weight when the car is at rest. Implementing Eqn. 2.1, this initial compression was found out to be 42 mm which was administered to the model using the APDL command snippet (1).

2.6.1 Lowering the Car Frame

The “ESEL” command was set to select a new set using “s”. The ‘item’ parameter was set to “type” which specifies the mode of selection to be on the basis of element type number. The component field was kept empty. ‘VMIN’ was assigned with the value “1” and ‘VMAX’ was assigned “59”. The default increment value from ‘VMIN’ to ‘VMAX’ will be “1” as nothing was assigned. This command line helps to select all the elements of the Car Frame. After the completion of the element selection, all the corresponding nodes of these elements were selected using the “NSLE” command. The selected set of nodes were then lowered by 42 mm with the “IC” command. This applied the initial condition of displacing ‘all’ the selected nodes in the y-direction (using the degree of freedom as ‘uy’) by “-0.042” meter. Finally, the “ALLSEL” was written to revert the selection back to all entities of the whole model.

(1) APDL Code for lowering the car frame by 42 mm.

```
ESEL,s,type,,1,59
NSLE
IC,all,uy,-0.042
ALLSEL
```

While performing the simulations, the trunk needs to be dropped from different heights ranging from 0 m to 10 m. To achieve this, two approaches were considered.

- **First Approach** – The log could be designed with a physical gap from the roof and then have a free fall from that height.
- **Second Approach** – No physical gap in-between the trunk and the car but instead an initial velocity was provided to the trunk depending on the height of free fall.

After performing a detailed comparison between these two approaches, some insights were developed,

- Providing a physical gap increased the time duration of the simulation.

- The increase in time gap happened as the initial phase of the simulation was occupied by the free fall of the log before contacting the car.
- During this time, the solver converged multiple sub steps leading to an increased time step size when the contact finally occurs.
- As a result, the residual forces increased resulting in a series of sub steps with no convergence to reduce the time step size causing delay.
- Finally, for each height increase, the gap had to be changed manually resulting in the generation of a new cdb file.

Due to the above reasons, the second approach was implemented. The designed tree trunk had a physical gap of 10 cm with the roof of the car. The tree trunk also had a gap of 42 mm due to the lowering of the car frame. To reduce both gaps, the APDL code (2) was used.

2.6.2 Lowering the Trunk

The “ESEL” command was set to select a new set using “s”. The ‘item’ parameter was set to “ename” which specifies the mode of selection to be on the basis of the element identification number. The component field was kept empty. ‘VMIN’ was assigned with the value “21”. This command line helps to select the point mass element attached to the tree trunk. The second “ESEL” command was set to add a new element set to the current selection using “a”. The component field was kept empty. ‘VMIN’ was assigned with the value “60” and ‘VMAX’ was assigned “61”. The default increment value from ‘VMIN’ to ‘VMAX’ will be “1” as nothing was assigned. This command line helps to select all the elements of the Tree Trunk as it was divided into two semi-cylindrical surfaces. All the corresponding nodes of these elements were selected using the “NSLE” command. The selected set of nodes were then lowered by 142 mm with the “IC” command. This applied the initial condition of displacing ‘all’ the selected nodes in the y-direction (using the degree of freedom as ‘uy’) by “-0.142” meter. Finally, the “ALLSEL” reverted the selection back to all entities of the whole model.

(2) APDL Code for lowering the trunk.

```
ESEL,s,enam,,21
ESEL,a,type,,60,61
NSLE
IC,all,uy,-0.142
ALLSEL
```

The initial velocity (v_0) was calculated using Eqn. 2.7 and the values are listed in Table 2.6.

$$v_0 = \sqrt{2g(h)} \quad 2.7$$

Height (h)	Acceleration	Initial Velocity (v_0)
1 m	$g = 9.8066 \text{ m/s}^2$	4.4176 m/s^2
2 m		6.2553 m/s^2
5 m		9.8979 m/s^2

Table 2.6. Values of Initial velocity according to the height of free fall.

To mimic the wheel-suspension system of a car, all the springs were constrained using codes.

2.6.3 Constraining the Damping and Wheel Springs

The “/PREP7” command is a preprocessing command used for setting up the model before simulation. The damping springs were defined using COMBIN14 spring element. The “ESEL” command was set to select a new set using “s”. The ‘item’ parameter was set to “ename” which specifies the mode of selection to be on the basis of the element identification number. The component field was kept empty. ‘VMIN’ was assigned with the value “14”. Thus all the springs defined using the COMBIN14 element were selected. Next, a loop was declared with the “*DO” command. This loop ran a total of four iterations for the four damping springs. Finally, the loop was terminated by deploying the “*ENDDO” command. Similarly, a second loop was used for the four torsional springs.

(3) APDL Code for constraining the damping and wheel springs.

```

/PREP7
ESEL,s,enam,,14

*DO,i,1,4
{!loop commands (a)}
*ENDDO

*DO,i,1,4
{!loop commands (b)}
*ENDDO

```

The “*GET” command assigned the minimum element number in the selected set of elements to the parameter “spelnum”. The second “*GET” command stored the element type number in the parameter “spetnum”. This type number was the one corresponding to the element number stored in “spelnum”. In the next step, the “KEYOPT” command was utilized. It requires three parameters namely, the *element type number* (which was stored in “spetnum”), the *key option number* of the element to be changed, and the *value to be assigned* to the selected key option to make the changes. For the COMBIN14 spring element, the Degree of Freedom selection is changed using KEYOPT(2). The value of KEYOPT(2) was set to “2” which constrained the longitudinal spring-damper to have a single degree of freedom in the “UY” direction. Finally, the element was unselected from the selected set of COMBIN14 elements using the “ESEL” command so that during the next iteration, only the elements with unchanged key options were present in the selection.

```
!loop commands (i)

*GET,spelnum,elem,,num,min
*GET,spetnum,elem,spelnum,attr,type
KEYOPT,spetnum,2,2
ESEL,u,elem,,spelnum
```

Just like the above loop commands, this loop was used to change the behaviour of the torsional springs. The only difference was the constraint of having only torsional behaviour in the z-direction. The value of KEYOPT(2) was set to “6” which constrained the springs to have a single degree of freedom in the “ROTZ” direction i.e., only torsion about the z-direction. Finally, the element was unselected from the selected set of COMBIN14 elements using the “ESEL” command so that during the next iteration, only the elements with unchanged key options were present in the selection.

```
!loop commands (ii)

*GET,spelnum,elem,,num,min
*GET,spetnum,elem,spelnum,attr,type
KEYOPT,spetnum,2,6
ESEL,u,elem,,spelnum
```

2.6.4 Constraining the Frictional Springs

The frictional springs were constrained to operate only along their respective axis. No loop was required as there were only two such springs. Moreover, the values for the two spring were different. To change the constraints of the spring aligned parallel to the z-axis, the spring was selected using double “*GET” commands just like the previous cases. The value of KEYOPT (2) was set to “3” which constrained the spring to have a single degree of freedom in the “UZ” direction i.e., only linear displacement along the z-direction. Finally, the element was unselected from the selected set of COMBIN14 elements using the “ESEL” command.

(4) APDL Code for constraining the Frictional springs.

```
!Spring along the Z-direction
*GET,spelnum,elem,,num,min
*GET,spetnum,elem,spelnum,attr,type
KEYO,spetnum,2,3
ESEL,u,elem,,spelnum
...
```

For the frictional spring aligned parallel to the x-axis, it was first selected using the double “*GET” commands like before. The value of KEYOPT (2) was set to “1” which constrained the spring to have a single degree of freedom in the “UX” direction i.e., only linear displacement along the x-direction. Finally, the element was unselected from the selected set of COMBIN14 elements using the “ESEL” command.

```
...
!Spring along the X-direction
*GET,spelnum,elem,,num,min
*GET,spetnum,elem,spelnum,attr,type
KEYOPT,spetnum,2,1
ESEL,u,elem,,spelnum
```

2.6.5 Constraining the Non-linear Springs

The non-linear springs were defined with the COMBIN39 element. The “ESEL” command was set to select a new set using “s”. The ‘item’ parameter was set to “ename” which specifies the

mode of selection to be on the basis of the element identification number. The component field was kept empty. ‘VMIN’ was assigned with the value “39”. This command line helped to select all the springs defined using the COMBIN39 element. Next, a loop was declared with the “*DO” command. This loop ran a total of four times to iterate among the four non-linear springs. The loop was then terminated by deploying the “*ENDDO” command. Since all the springs had been constrained, the “ALLSEL” was written to revert the selection back to all entities of the whole model. Finally, the “FINISH” was written to exit normally from the ANSYS processor.

(5) APDL Code for constraining the non-linear springs.

```
ESEL,s,enam,,39

*DO,i,1,4
{!loop commands (iii)}
*ENDDO

ALLSEL
FINISH
```

Continuing to loop commands (iii), the “*GET” command assigned the minimum element number in the selected set of elements to the parameter “spelnum”. The second “*GET” command stored the element type number in the parameter “spetnum”. This type number was the one corresponding to the element number stored in “spelnum”. In the next step, the “KEYOPT” command was utilized. It requires three parameters namely, the *element type number* (which was stored in “spetnum”), the *key option number* of the element to be changed, and *the value to be assigned* to the selected key option to make the changes. For the COMBIN39 spring element, the Degree of Freedom selection is changed using KEYOPT(3). The value of KEYOPT(3) was set to “2” which constrained the longitudinal spring-damper to have a single degree of freedom in the “UY” direction. The second “KEYOPT” command assigns the value “0” to KEYOPT(4) which prevents KEYOPT(4) from overriding KEYOPT(3). Finally, the element was unselected from the selected set of COMBIN14 elements using the “ESEL” command so that during the next iteration, only the elements with unchanged key options were present in the selection. This concludes all the APDL command snippets that have been utilized in this study for pre-processing.

```

{!loop commands (iii)}

*GET,spelnum,elem,,num,min
*GET,spetnum,elem,spelnum,attr,type
KEYOPT,spetnum,3,2
KEYOPT,spetnum,4,0
ESEL,u,elem,,spelnum

```

A few changes were made to the default analysis settings before running the simulation. These changes are listed below in Figure 2.11.

Step Controls		Nonlinear Controls	
Number of Steps	1	Force Convergence	Program Controlled
Current Step Number	1	Moment Convergence	Remove
Step End Time	1 s	Disp. Convergence	Program Controlled
Auto Time Stepping	On	Output Controls	
Define By	Substeps	Stress	Yes
Initial Substeps	1.00 E+05	Back Stress	No
Minimum Substeps	100	Strain	Yes
Maximum Substeps	1.00 E+05	Contact Data	Yes
Time Integration	On	Nodal Forces	Yes
Solver Controls		Damping Controls	
Solver Type	Direct	Method	Direct Input
Weak Springs	Off	Stiffness Damping	0
Large Deflection	On	Mass Damping	4.424

Figure 2.11. The Analysis settings used for carrying out the simulations.

2.7 Post-processing

The forces exerted on the roof and the suspensions were obtained after loading the result (.rst) files in Mechanical APDL. Three parameters namely,

- Rear Wheel Suspension force

- Front Wheel Suspension force
- Total Force on Roof Surface were extracted.

The forces acting on the whole roof was obtained after algebraically adding up the forces acting individually on the Roof Surface and the Rim. ANSYS Mechanical has the option to execute post commands after completing a simulation and the results are obtained in the Post Output window. The Roof forces were extracted from the RST file using Code Snippet (6) and (7).

2.7.1 Calculating the forces on the Roof

Two “*DIM” commands were used to declare two arrays namely, “froof” and “frim”. The “froof” array stored the forces experienced by all the nodes of the roof surface and the “frim” array stored the forces of the rim of the roof. The argument “arg1” stored the total number of converged substeps of that particular simulation whose forces were being extracted. The arrays were defined with these parameters to store the forces at each and every converged substep. Next, a loop was declared with the “*DO” command. This loop would iterate according to the number of converged substeps starting from 1 extracting and storing the roof forces at each substep. The loop was then terminated by deploying the “*ENDDO” command. Finally, the forces were displayed in the Post Output window using the “*vwrite” command.

(6) APDL Code to calculate the forces on the roof.

```
*DIM,froof,array,arg1,1,1
*DIME,frim,array,arg1,1,1

*DO,i,1,arg1
{!loop commands (iv)}
{!loop commands (v)}
*ENDDO

*vwrite,froof(1),frim(1)
```

This loop was used to calculate the roof forces experienced on the roof surface. The “SET” command was used to define the data set as the i^{th} substep of the 1st Load step. The “ESEL” command was used to select the elements with type number “62” i.e., the roof surface elements. After the completion of the element selection, all the corresponding nodes of these elements were selected using the “NSLE” command. The following “FSUM” command gave the

summation of forces in only the contact nodes. The “*GET” command was used to extract “fy”. The value got assigned to ‘f1’ temporarily which was then stored in the “froof()” array under the ith row. The iterations continued till ‘i’ became equal to the value of “arg1”.

```

{!loop commands (iv)}
SET,1,i

ESEL,s,type,,62
NSLE
FSUM,,cont

*GET,f1,fsum,,item,fy
froof(i)=f1

```

This loop was used to calculate the forces experienced on the roof rim. The “ESEL” command was used to select the elements with type number “64” i.e., the roof rim elements. After the completion of the element selection, all the corresponding nodes of these elements were selected using the “NSLE” command. The following “FSUM” command gave the summation of forces in only the contact nodes. The “*GET” command was used to extract “fy” i.e., y-component of the summation of the nodal contact forces obtained from the “FSUM” command. The value got assigned to ‘f2’ temporarily which was then stored in the “frim()” array under the ith row. The iterations continued till ‘i’ became equal to the value of “arg1”.

```

{!loop commands (v)}
ESEL,s,type,,64
NSLE
FSUM,,cont

*get,f2,fsum,,item,fy
frim(i)=f2

```

Two forces were obtained from the suspensions. One was the Spring Force and the other was the Damping Force. Two different sets of four springs each were deployed for achieving the result. The first set of four COMBIN14 longitudinal springs provide the damping whereas the second set of four COMBIN39 non-linear longitudinal springs provide the spring force. These forces were obtained using the Code (7).

2.7.2 Calculating all the Suspension forces

The “ESEL” command was set to select a new set using “s”. All the springs defined using the COMBIN14 element were selected. A value of “0” was assigned to the parameter “spelnum”. Next, a loop was declared with the “*DO” command. This loop iterated four times for the four damping springs.

(7) APDL Code to calculate all the forces on the suspensions.

```
ESEL,s,enam,,14
spelnum = 0
*DO,i,1,4
{!loop commands (vi)}
*ENDDO
...
```

The loop was used to assign arbitrary reference numbers to the different result parameters to be extracted from the springs. The “elnext ()” command was used to get the number of the next element from the selected set of elements. The “ESOL” command specified a reference number to the damping forces in each and every spring element. Since the damping forces of a spring are Nonsummable (nmisc) items which are not averaged, the Sequence Number method was used to extract the data using “ESOL”. For COMBIN14, the sequence number for getting damping forces is “3”. At the end, reference number 2, 3, 4, and 5 were assigned to the damping forces of the four springs.

```
{!loop commands (vi)}
spelnum = elnext(spelnum)
ESOL,1+i,spelnum,,nmisc,3
```

This part of the code was used for the non-linear springs. The “ESEL” command was set to select a new set using “s”. All the four springs defined using the COMBIN39 element were selected. A value of “0” was assigned to the parameter “spelnum”. Next, a loop was declared with the “*DO” command. This loop iterated four times for the four non-linear longitudinal springs.

```

...
ESEL,s,enam,,39
spelnum = 0
*DO,i,1,4
{!loop commands (vii)}
*ENDDO
...

```

The “`elnext()`” command was used to get the number of the next element from the selected set of elements. The “`ESOL`” command specified a reference number to the spring forces in each and every spring element. Since the spring forces are Summable (`smisc`) items which are not averaged, the Sequence Number method was used. For `COMBIN39`, the sequence number for getting spring forces is “1”. At the end, reference number 6, 7, 8, and 9 were assigned to the spring forces of the four non-linear springs.

```

{!loop commands (vii)}

spelnum = elnext(spelnum)
ESOL,5+i,spelnum,,smisc,1

```

Finally, the “`PRVAR`” command was used to list the values of the variables assigned with the reference numbers against time.

```

...
PRVAR,2,3,4,5
PRVAR,6,7,8,9

```

This concludes all the APDL command snippets that have been utilized in this study for post-processing. The forces extracted using these codes were then analysed to procure meaningful and probable insights.

2.8 System Specifications and Miscellaneous Parameters

The specifications of the computing system are listed in Table 2.7.

Part	Specification
Processor	Intel i5 12400F (6 Cores + 12 Threads)
CPU Base Clock Speed	2.5 GHz
RAM	16 GB DDR4
RAM Clock speed	3200 MHz
GPU	GTX 1650 (4 GB)
GPU Acceleration	Turned Off

Table 2.7. Specifications of the Computing Device Hardware used.

Rest of the Miscellaneous Parameters are mentioned in Table 2.8.

Parameters	Value
Total D.O.F.	3,50,498
Number of CPU Cores Requested	6
RAM Utilized	12.63 GB
Average Time for Simulations	2.717 hrs (or) 163 mins
Shortest Time for Simulations	1.01 hrs (or) 66 mins
Average Time for Simulations	3.85 hrs (or) 233 mins

Table 2.8. Miscellaneous parameters pertaining to the simulations.

The utilization of the Processor during the runtime of the simulations is shown in Figure 2.12. In the left half of the picture, utilization of all the system components were shown. The right half of the figure shows the per core utilization and temperatures of the CPU.

Figure 2.13 highlights the Total CPU utilization accompanied by the rest of the statistics. The average CPU utilization remained around 80% over the course of time taken to run the simulations.

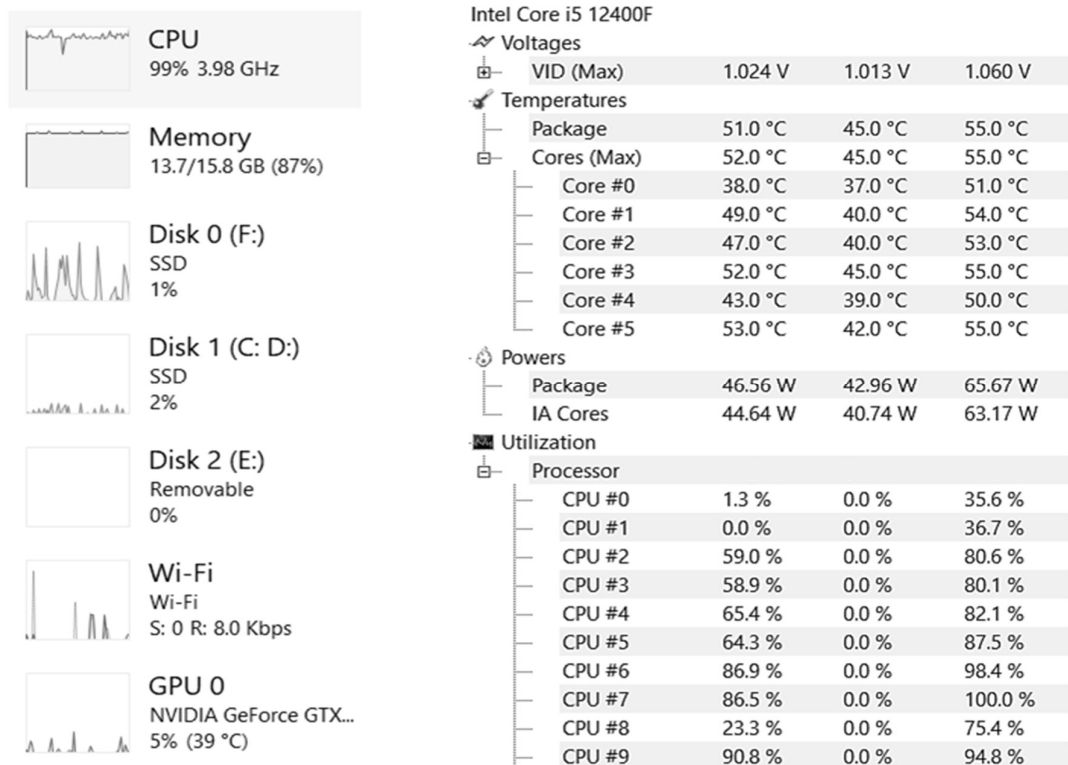


Figure 2.12. Runtime utilization of the system hardware extracted with HW Monitor.

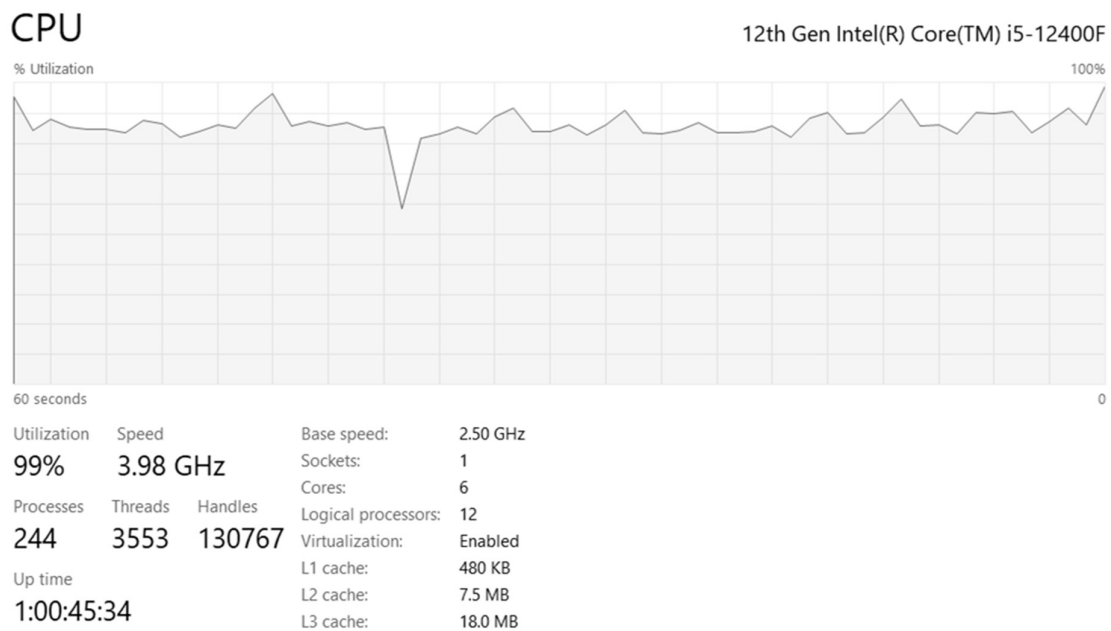


Figure 2.13. Runtime utilization of the CPU extracted with the Windows Task Manager.

Chapter 3: Results and Discussion

A total of 11 simulations were carried out with different parameters. Out of the 11 simulations, one was a Static Structural Analysis while the rest were Transient in nature. For the simulations, two parameters were varied namely,

- The height (h) from which the tree trunk had a free fall and,
- The material used to model the car body

Three kind of materials were used as stated earlier. The Heat Treated UHSS material was utilized for all the Transient simulations where the height of free fall was varied from 0 to 10 meters as well as the single Static simulation. Collectively, a total of 9 simulations had the same material. On closer inspection, a height of up to 5 m should have been practical but the higher heights helped in developing a better understanding.

Continuing to the second set of simulations, the height of free fall was kept constant at 5 meters while the material was changed to DP 350-600 (AHSS) with a yield stress of 350.98 MPa followed by UHSS – Baseline with a yield stress of 1183.61 MPa. A total of three simulations were carried out for the three different materials with the tree trunk having the same height of free fall.

3.1 Simulations with Heat Treated UHSS as the material

This section has been broadly divided into three categories based on the results obtained from all the simulations with the same material used in the car frame. The results extracted from the various simulations have been depicted in the first two categories. The third and final part establishes a correlation within the data obtained as a result from the simulations.

3.1.1 Car Frame loaded with the trunk under Static conditions

Under Static loading conditions, the car frame deformed by a maximum of 12.2 cm. This deformation was noticed at the tail end of the model as shown in Figure 3.1(a). The Roof of the car deformed by a maximum of 11.8 cm from its initial position as shown in Figure 3.1 (b) and Figure 3.1 (c). The Roof Distortion was calculated to be about 1.1 cm approximately. No plastic strain was found as the maximum amount of stress developed in the model was 138 Mpa. The maximum stress was located on the rim of the roof.

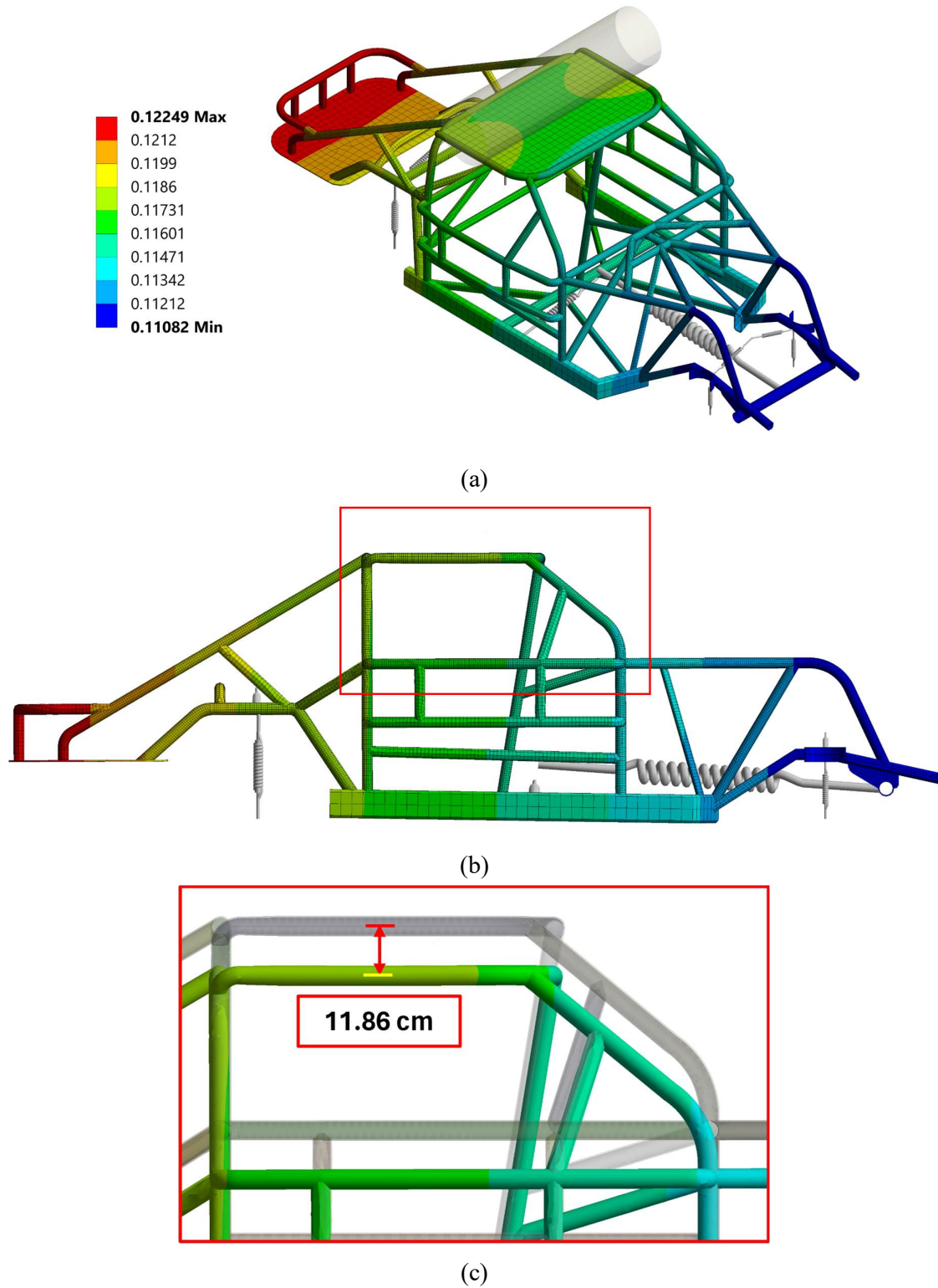


Figure 3.1. Depiction of the Total Deformation across the (a) whole Car Frame in Isometric View, (b) whole Car Frame from Side View, and (c) enlarged portion of the side view emphasizing the Roof Deformation for the Static Analysis at $t = 1$ s.

3.1.2 Free Fall from different heights under Transient conditions

The heights used for the Transient simulations were 0 m, 1 m, 2 m, 3 m, 4 m, 5 m, 7.5 m, and 10 m respectively. All these Transient simulations had the same material used in the car frame. Seven parameters namely, the Equivalent Plastic Strain (ε_{eq}), Equivalent Stress (σ_{eq}), Roof Force (F_R), Suspension Spring Force (F_S), Suspension Damping Force (F_D), Total Suspension Force (F_T), and the Roof Distortion (u_R) were taken into consideration. The maximum values obtained from for all the above parameters are listed below in Table 3.1 and Table 3.2.

Height (h)	ε_{eq}^{max}	σ_{eq}^{max} (Mpa)	u_R^{max} (cm)
0 m	0.42	203.08	2.1
1 m	8.02	403.87	4.8
2 m	19.57	436.31	8.9
3 m	26.19	443.29	11.3
4 m	28.22	445.97	12.8
5 m	29.38	453.17	14.0
7.5 m	30.61	461.21	16.1
10 m	47.65	457.07	17.2

Table 3.1. Maximum values of Equivalent Plastic Strain (ε_{eq}), Equivalent Stress (σ_{eq}), and Roof Distortion (u_R) vs. Height (h) of free fall.

Height (h)	F_R^{max} (kN)	F_S^{max} (kN)	F_D^{max} (kN)	F_T^{max} (kN)
0 m	13.90	5.94	0.78	6.07
1 m	69.73	17.17	4.78	17.40
2 m	85.52	38.32	7.53	38.88
3 m	101.72	36.21	7.08	37.06
4 m	142.93	42.66	7.83	43.59
5 m	121.86	47.10	8.39	47.77
7.5 m	183.72	59.01	10.08	59.45
10 m	293.96	67.71	11.65	68.51

Table 3.2. Maximum values of Roof Force (F_R), Suspension Spring Force (F_S), Suspension Damping Force (F_D), and Total Suspension Force (F_T) vs. Height (h)

3.1.2.1 Deformation of the car frame at different heights

Apart from the values listed above, one more parameter worth mentioning is the Total Deformation of the roof structure at the end of 1 s. This parameter consisted of two separate entities namely, the roof displacement and the roof distortion. The summation of these two gives the Total Roof Deformation (u_{TD}). After noting the maximum value of this parameter across all simulations, the least deformation was observed in the 0 m drop and the maximum occurs in the 10 m drop scenario as listed in Table 3.3.

Height (h)	u_{TD}^{\max} (cm)
0 m	13.33
1 m	16.35
2 m	22.73
3 m	27.04
4 m	30.51
5 m	34.20
7.5 m	42.26
10 m	50.95

Table 3.3. Maximum value of Roof Deformation (u_{TD}) vs. Height (h) of free fall.

Figure 3.2 to Figure 3.9 represent the Total Deformation of the car frame at the end of one second for different heights of free fall of the tree trunk. Part (a) of all the figures represent the isometric view of the deformed frame with the tree trunk partially visible. Noticeable distortion of 4.8 cm with a deformation of 16.35 cm was observed in Figure 3.3 which represents the 1 m free fall of the trunk. The distortion was a bit short from doubling itself at 8.9 cm when the height was increased to 2 m as shown in Figure 3.4. From 3 m onwards, the distortion kept on increasing gradually without any sudden jumps and reached 16.1 cm at 7.5 m height as represented in Figure 3.8.

After the height of fall reached 4 m, some amount of noticeable upward bending was observed in the rear section of the frame represented by Figure 3.6 (b). This bending became prominent in Figure 3.7 (b) which depicts the side view of the car frame with 5 m height of free fall. The 10 m height variation in Figure 3.9 shows major distortion and flattening of the frame due to the trunk and suspension forces acting in the opposite direction.

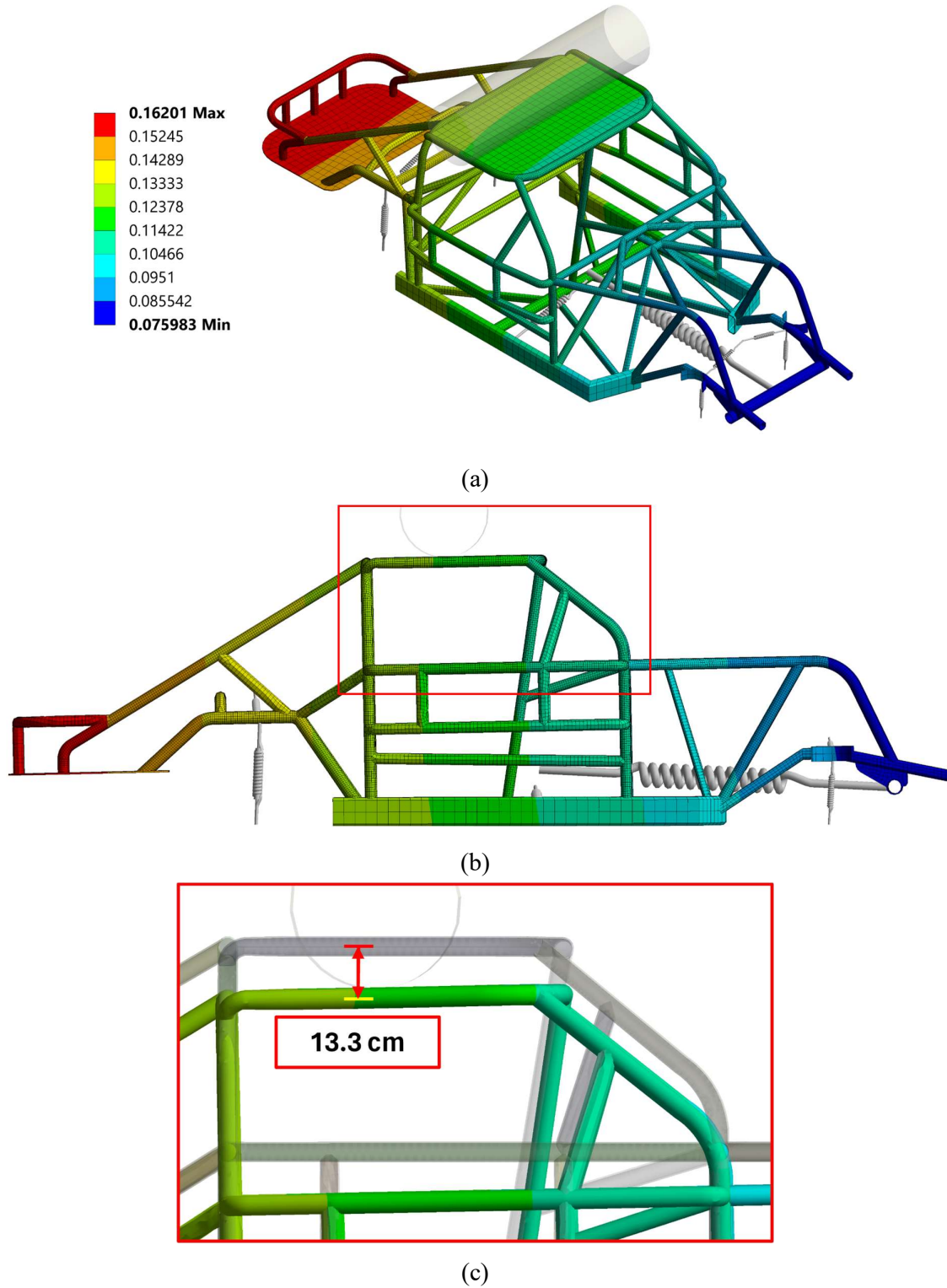


Figure 3.2. Depiction of the Total Deformation across the (a) whole Car Frame in Isometric View, (b) whole Car Frame from Side View, and (c) enlarged portion of the side view emphasizing the Roof Deformation for the 0 m Height Transient Analysis at $t = 1$ s.

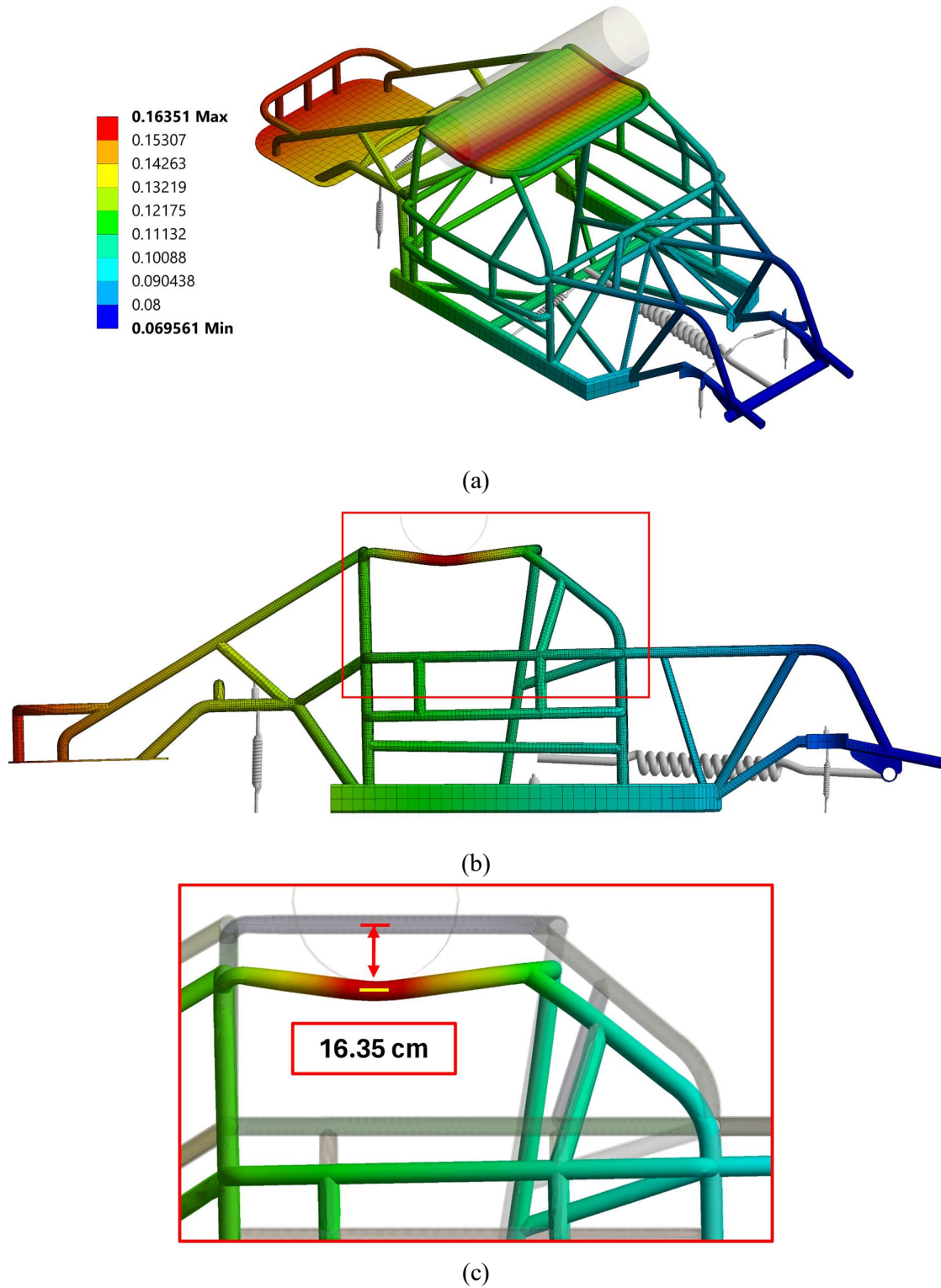


Figure 3.3. Depiction of the Total Deformation across the (a) whole Car Frame in Isometric View, (b) whole Car Frame from Side View, and (c) enlarged portion of the side view emphasizing the Roof Deformation for the 1 m Height Transient Analysis at $t = 1$ s.

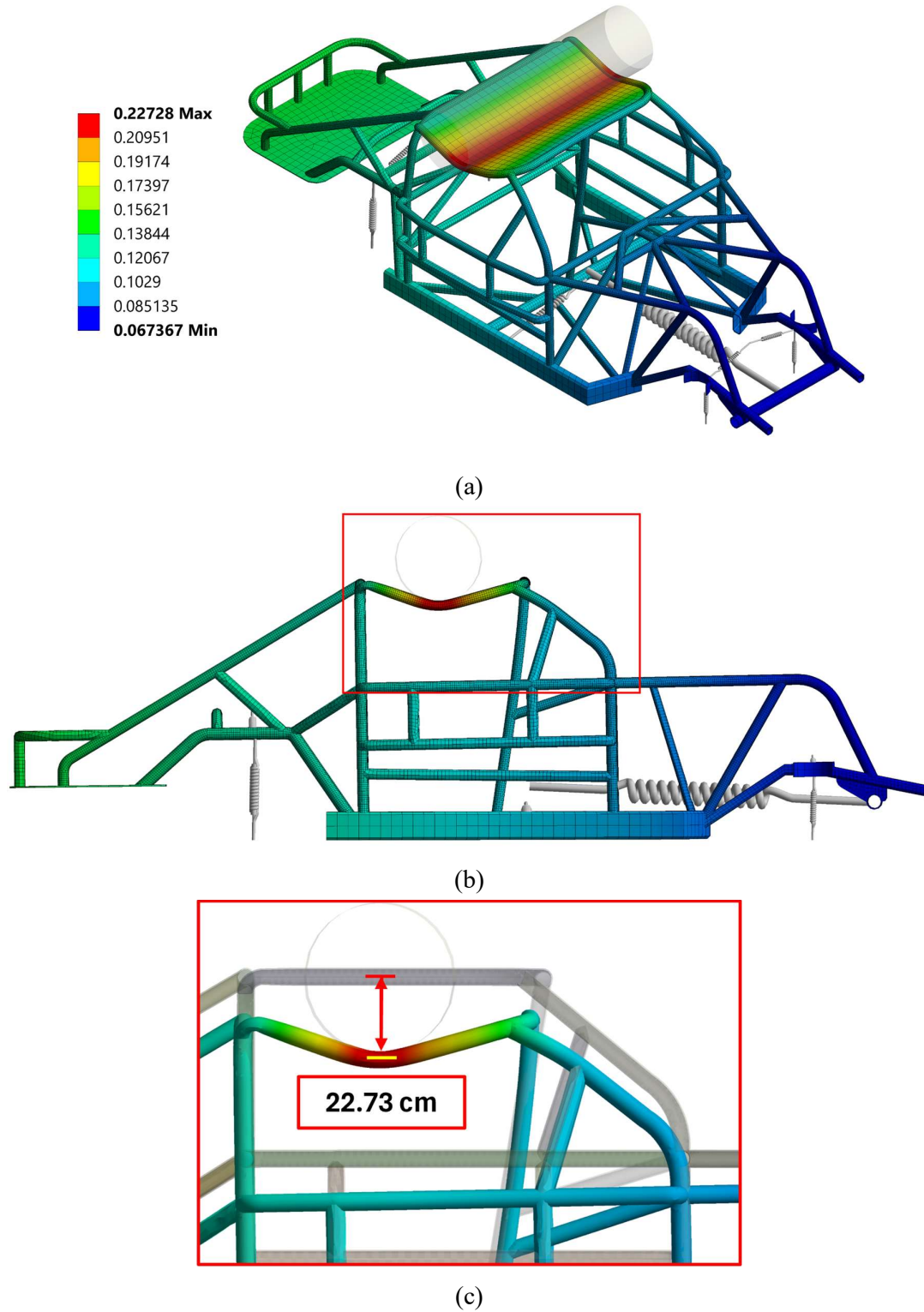


Figure 3.4. Depiction of the Total Deformation across the (a) whole Car Frame in Isometric View, (b) whole Car Frame from Side View, and (c) enlarged portion of the side view emphasizing the Roof Deformation for the 2 m Height Transient Analysis at $t = 1$ s.

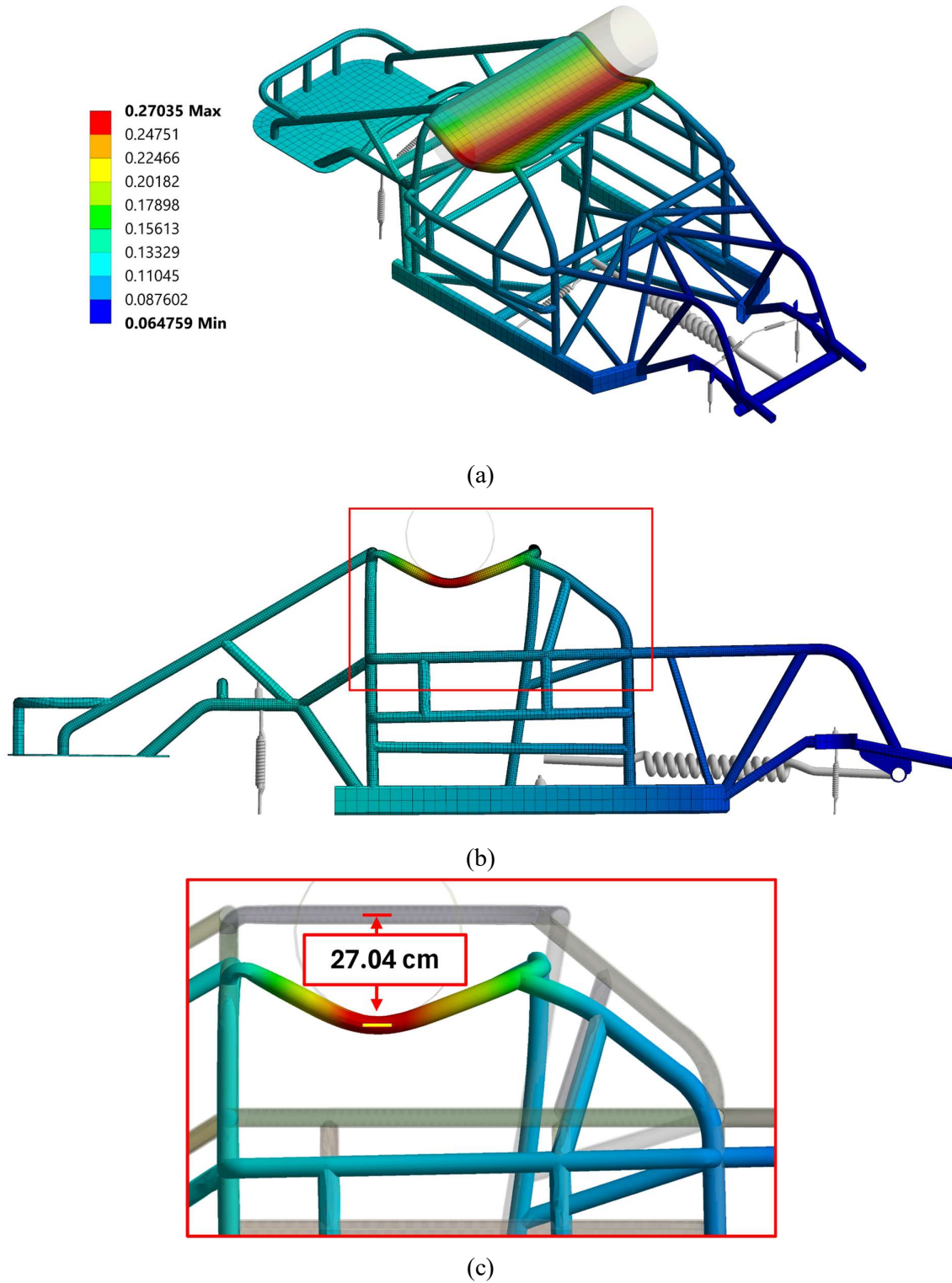


Figure 3.5. Depiction of the Total Deformation across the (a) whole Car Frame in Isometric View, (b) whole Car Frame from Side View, and (c) enlarged portion of the side view emphasizing the Roof Deformation for the 3 m Height Transient Analysis at $t = 1$ s.

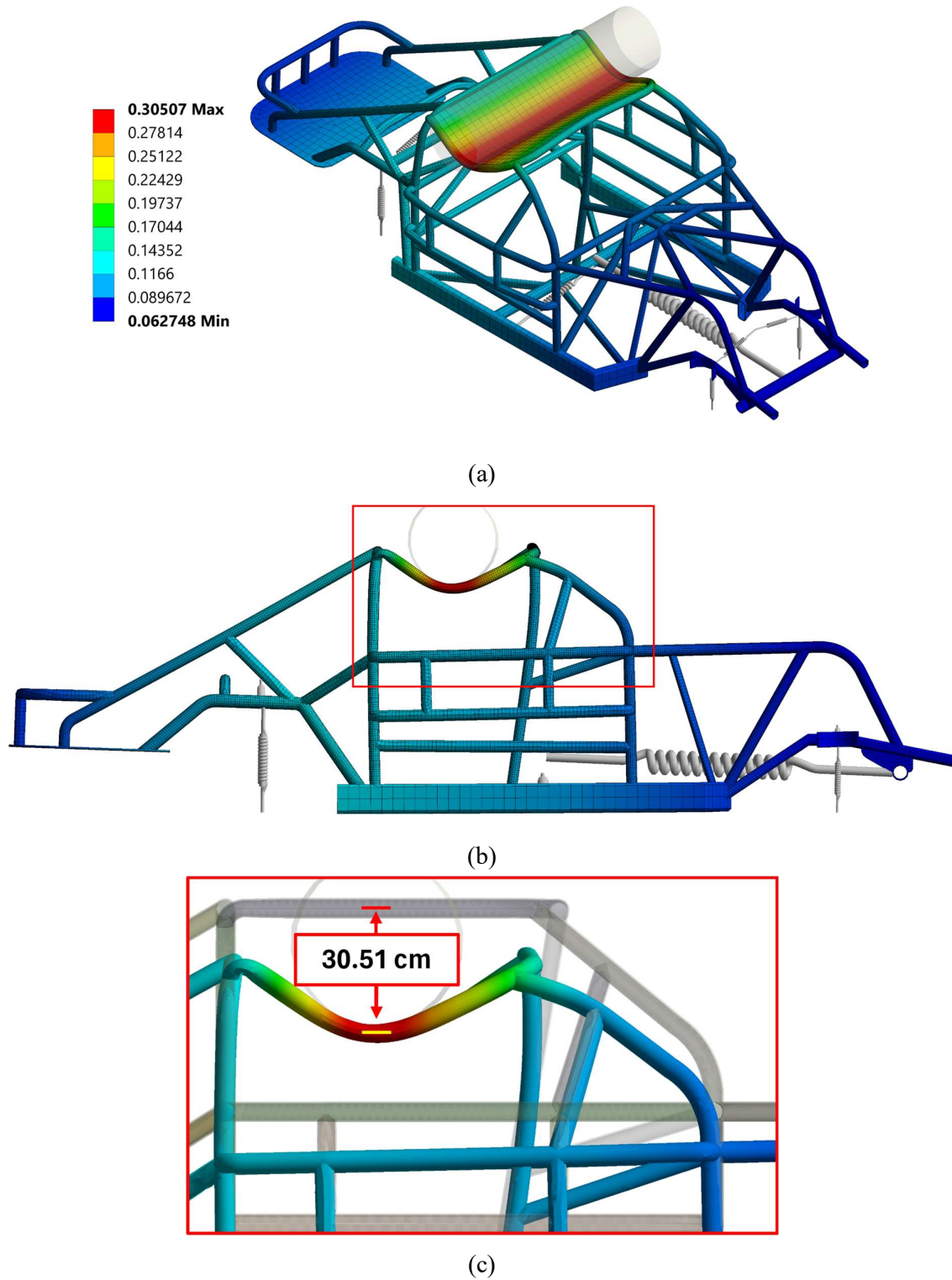


Figure 3.6. Depiction of the Total Deformation across the (a) whole Car Frame in Isometric View, (b) whole Car Frame from Side View, and (c) enlarged portion of the side view emphasizing the Roof Deformation for the 4 m Height Transient Analysis at $t = 1$ s.

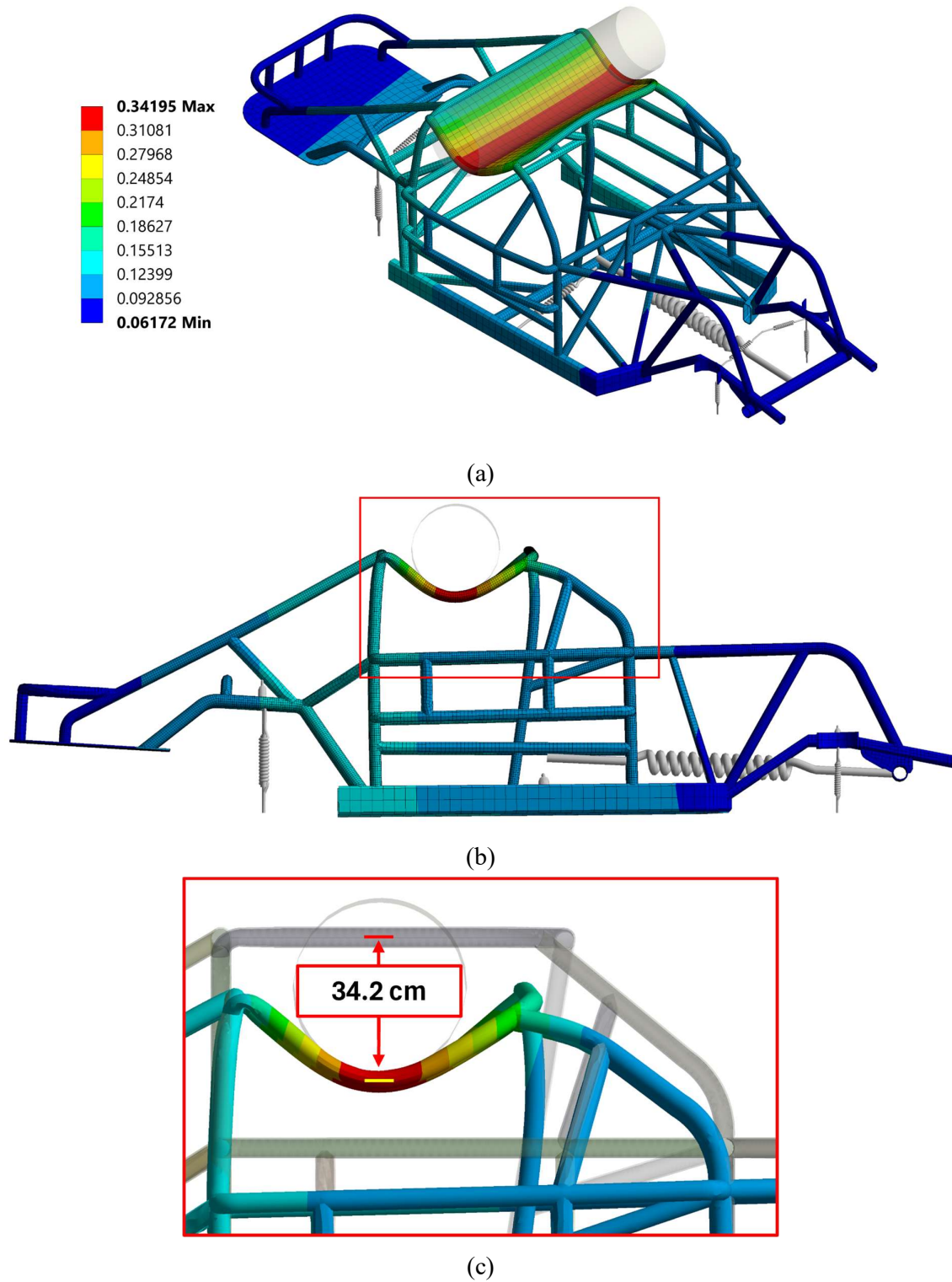


Figure 3.7. Depiction of the Total Deformation across the (a) whole Car Frame in Isometric View, (b) whole Car Frame from Side View, and (c) enlarged portion of the side view emphasizing the Roof Deformation for the 5 m Height Transient Analysis at $t = 1$ s.

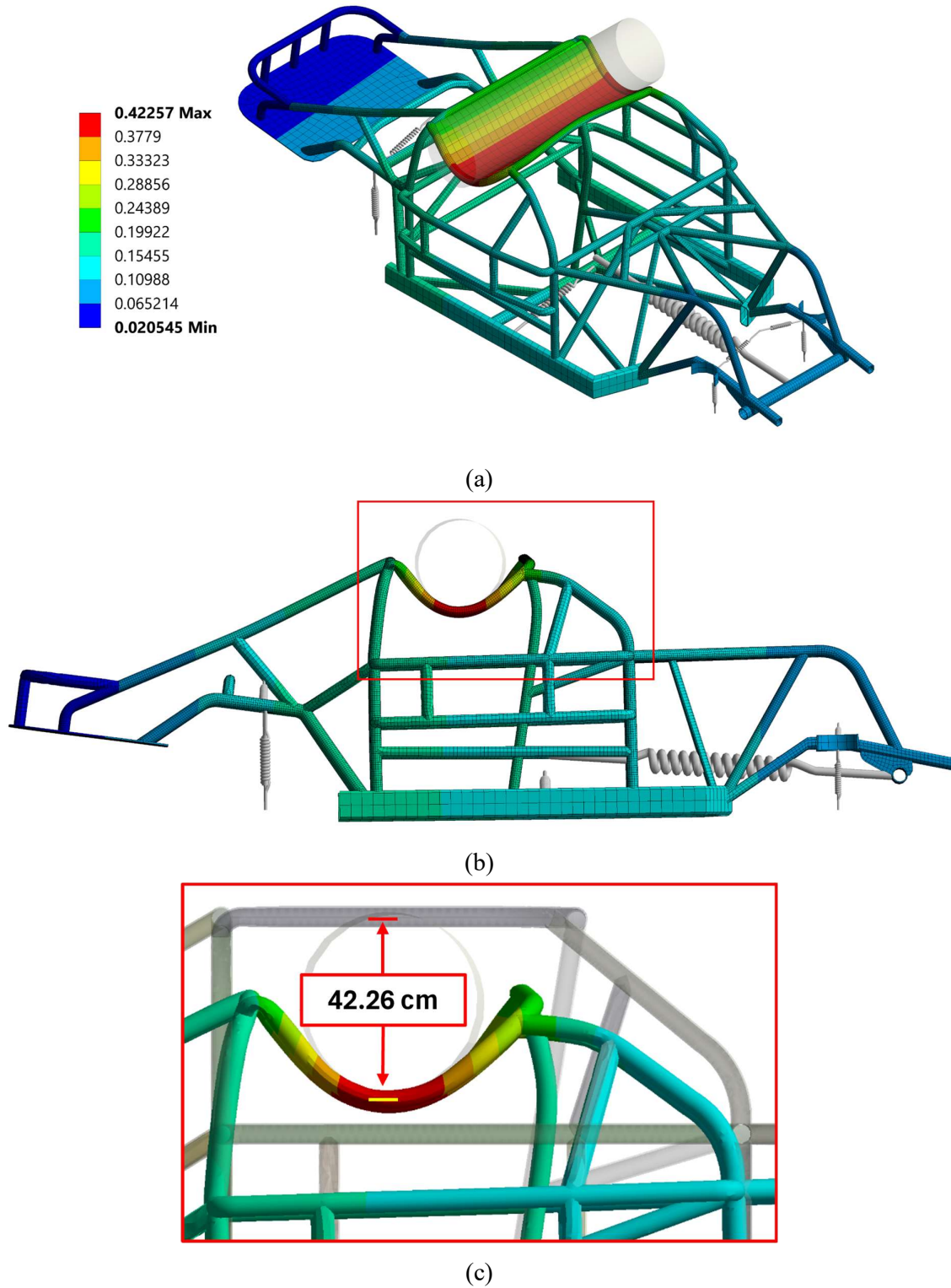


Figure 3.8. Depiction of the Total Deformation across the (a) whole Car Frame in Isometric View, (b) whole Car Frame from Side View, and (c) enlarged portion of the side view emphasizing the Roof Deformation for the 7.5 m Height Transient Analysis at $t = 1$ s.

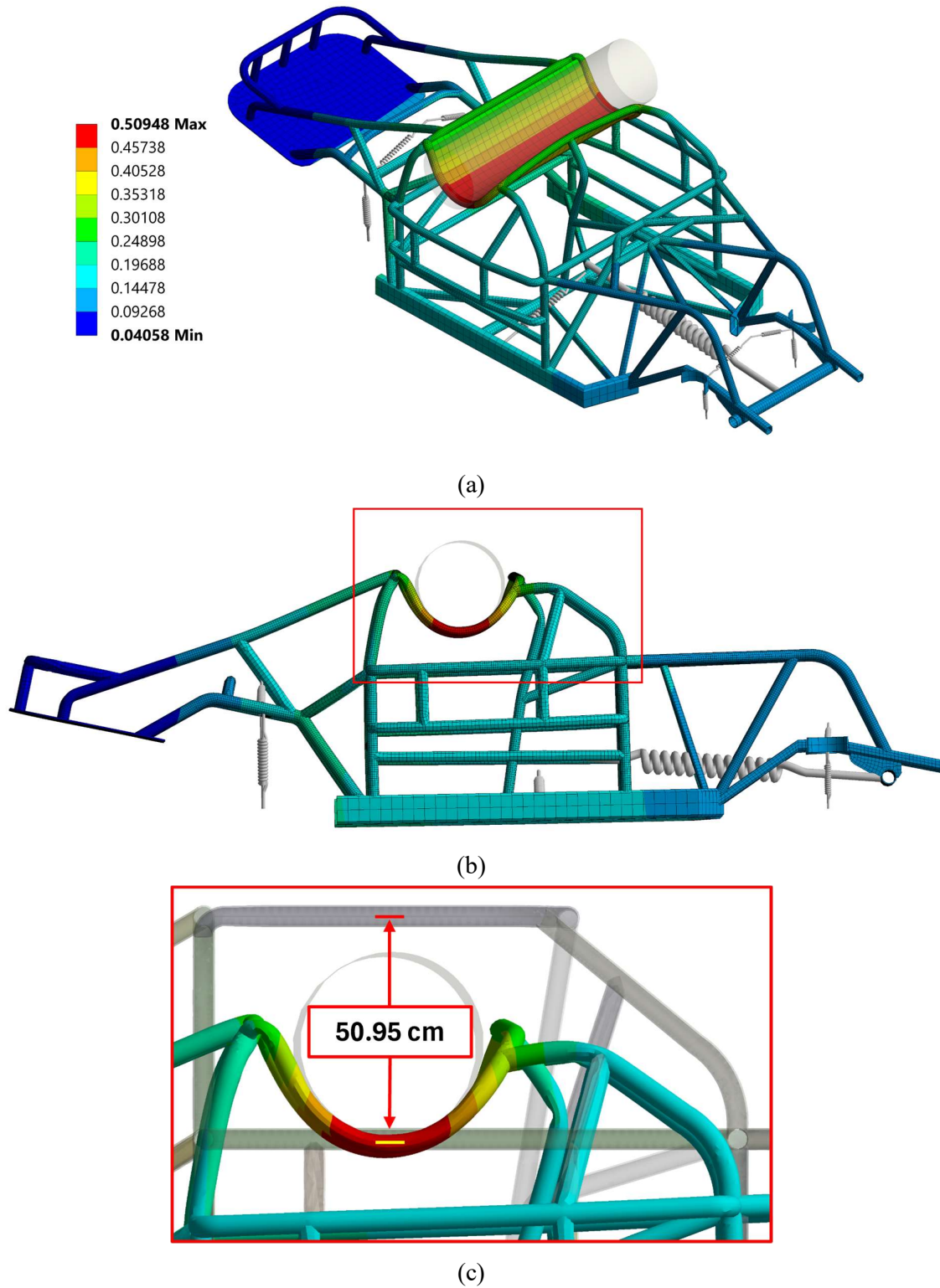


Figure 3.9. Depiction of the Total Deformation across the (a) whole Car Frame in Isometric View, (b) whole Car Frame from Side View, and (c) enlarged portion of the side view emphasizing the Roof Deformation for the 10 m Height Transient Analysis at $t = 1$ s.

3.1.2.2 Maximum Stress developed in the car frame at different heights

The maximum values of stress for each transient simulation have been listed in Table 3.1. A sudden jump from 203.08 MPa to 403.87 MPa was observed in this parameter when the height of fall was increased to 1 m. On further increasing the height, the change in the maximum equivalent stress value became much more minimal.

As shown in Figure 3.10 (a), (b), (c), and (d), the maximum stress occurs in the region where the trunk encountered the rim of the roof. This pattern remained the same till 3 m height of free fall. The value of maximum stress reached 436.31 MPa when the height of free fall reached 2 m as shown in Figure 3.10 (c) .i.e., an increase of 32.44 MPa from the previous case of 1 m fall height. The change further decreased for the case with 4 m height of free fall.

Increasing the height of free fall beyond 3 m fixed the location where maximum stress develops in the frame. As shown in Figure 3.10, for the heights of 4 m to 10 m, the hotspot occurs in the pillar which supports the windshield of the car. The case with 7.5 m height of free fall recorded the maximum value of 461.21 MPa followed by a slight decrease to 457.07 MPa when the height was increased to 10 m as depicted in Figure 3.10 (g) and Figure 3.10 (h).

3.2 Correlation between the Static and Transient Solutions

After performing a detailed comparison among the nine simulations, several insights were obtained. Seven parameters namely, the Equivalent Plastic Strain (ϵ_{eq}), Equivalent Stress (σ_{eq}), Roof Force (F_R), Suspension Spring Force (F_S), Suspension Damping Force (F_D), Total Suspension Force (F_T), and the Roof Distortion (u_R) were taken into consideration. The maximum value of these parameters was extracted for each simulation and were divided with the maximum values obtained from the static structural simulation. The only exception in this case was the Equivalent Plastic strain. The values obtained are listed in Table 3.4. The factors obtained were defined using Eqn. 3.1.

$$f_{X^{\max}} := \frac{X^{\max}}{X_s^{\max}} \quad 3.1$$

The parameter X_s^{\max} represents the maximum value of the parameter X obtained from quasi-static loading conditions. The parameter X^{\max} represents the maximum value of the parameter X extracted from the results of the transient simulations for all the various heights of free fall.

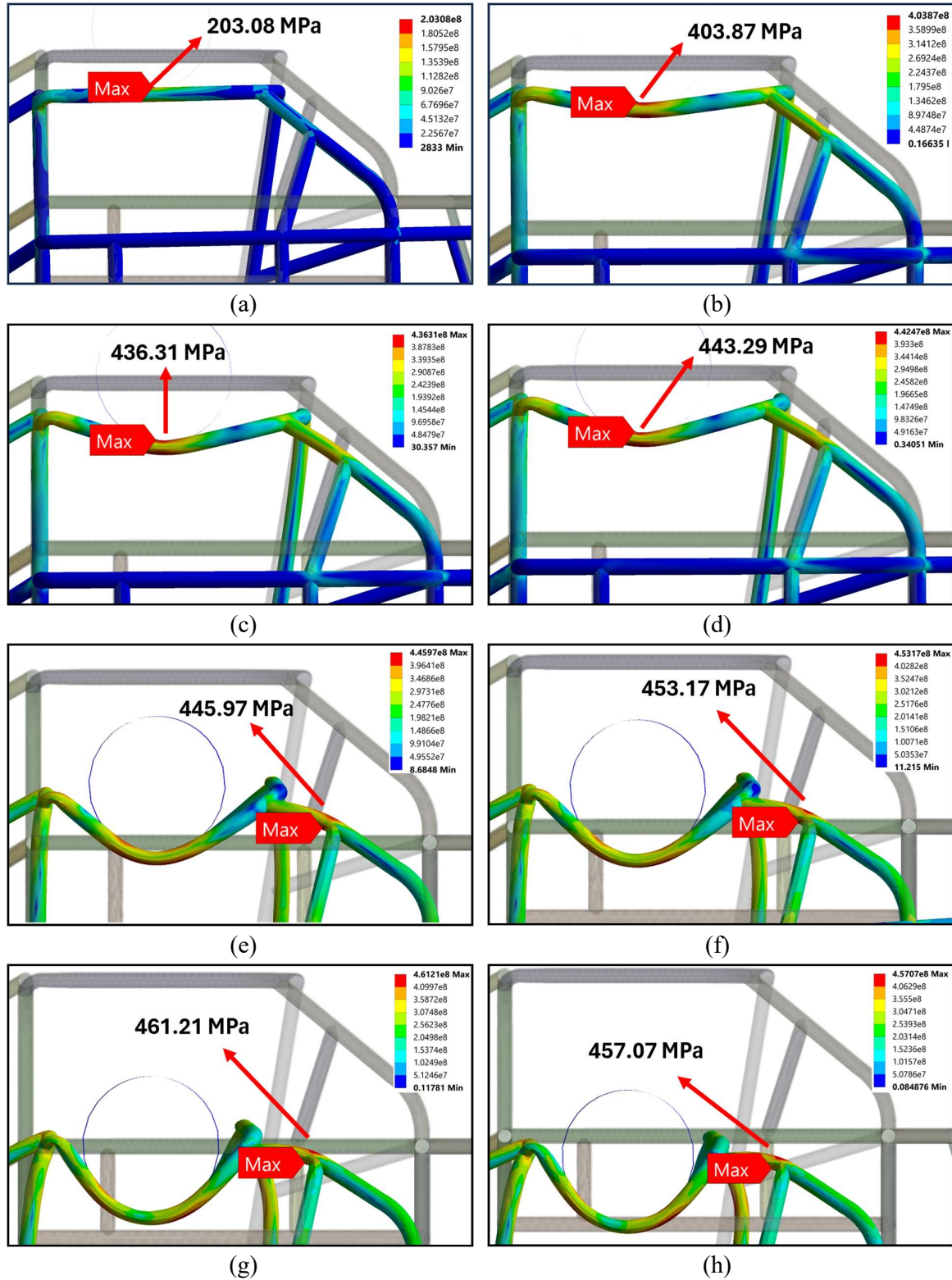


Figure 3.10. The Maximum Equivalent Stress (σ_{eq}^{max}) developed in the model for (a) 0 m Transient, (b) 1 m Transient, (c) 2 m Transient, and (d) 3 m Transient (e) 4 m Transient, (f) 5 m Transient, (g) 7.5 m Transient, and (h) 10 m Transient Simulations.

h (m)	ε_{eq}^{max}	$f_{\sigma_{eq}^{max}}$	$f_{F_R^{max}}$	$f_{F_S^{max}}$	$f_{F_D^{max}}$	$f_{F_T^{max}}$	$f_{u_R^{max}}$
0	0.42 %	1.47	1.32	1.65	0.22	1.69	1.91
1	8.02 %	2.93	6.76	4.78	1.33	4.84	4.36
2	19.57 %	3.16	8.88	10.66	2.09	10.82	8.09
3	26.19 %	3.21	9.66	10.08	1.97	10.31	10.27
4	28.22 %	3.23	13.57	11.87	2.18	12.13	11.64
5	29.38 %	3.28	11.57	13.10	2.33	13.29	12.73
7.5	30.61 %	3.34	17.44	16.42	2.80	16.54	14.64
10	47.65 %	3.31	27.91	18.84	3.24	19.06	15.64

Table 3.4. Values of the Max. Eq. Plastic Strain (ε_{eq}^{max}), Stress factor ($f_{\sigma_{eq}^{max}}$), Roof Force factor ($f_{F_R^{max}}$), Spring Force factor ($f_{F_S^{max}}$), Damping Force factor ($f_{F_D^{max}}$), Total Suspension Force factor ($f_{F_T^{max}}$), and Roof Deformation factor ($f_{u_R^{max}}$) vs. Height (h) of free fall.

The factors obtained for the parameters were individually evaluated against the height of fall using Eqn. 3.2. This equation has two behaviours; one is an exponentially decreasing nature and the other is a linear behaviour with the height of fall. The four parameters in this equation were estimated in MATLAB utilizing the curve fitting commands with the data listed in Table 3.4.

$$f_{X^{max}} = f_0 + f_Q(1 - e^{-bh}) + f_m h \quad 3.2$$

In the Eqn. 3.2, f_0 represents the initial value of the factor at $h = 0$, f_Q represents the maximum value of exponential dependence, b represents the constant of exponential decay, and f_m represents the slope of the linear dependence. The unit of b is m^{-1} while the rest of the constants are dimensionless. The base equation for Equivalent Plastic Strain is represented by Eqn. 3.3. In this equation, all the constants except b are expressed in percent (%).

$$\varepsilon_{eq}^{max} = \varepsilon_0 + \varepsilon_Q(1 - e^{-bh}) + \varepsilon_m h \quad 3.3$$

3.2.1.1 Maximum Equivalent Plastic Strain

The value was zero for the static analysis. The Transient simulation having 0 m height of free fall as expected, developed the least plastic strain of 0.42 %. As the height was increased, the maximum amount of plastic strain developed in the car body over time and space also increased. The strain reached a value of 30.61 % for the case where the height was 7.5 m. Beyond this height, there was a drastic increase, and the data was excluded while the approximate trendline was being fit. The equation of the non-linear fit obtained is given by Eqn. 3.4. The FE Result data along with the fitted curve is shown in Figure 3.11.

$$\varepsilon_{eq}^{\max} = 33.33 (1 - e^{-0.43 h}) \quad 3.4$$

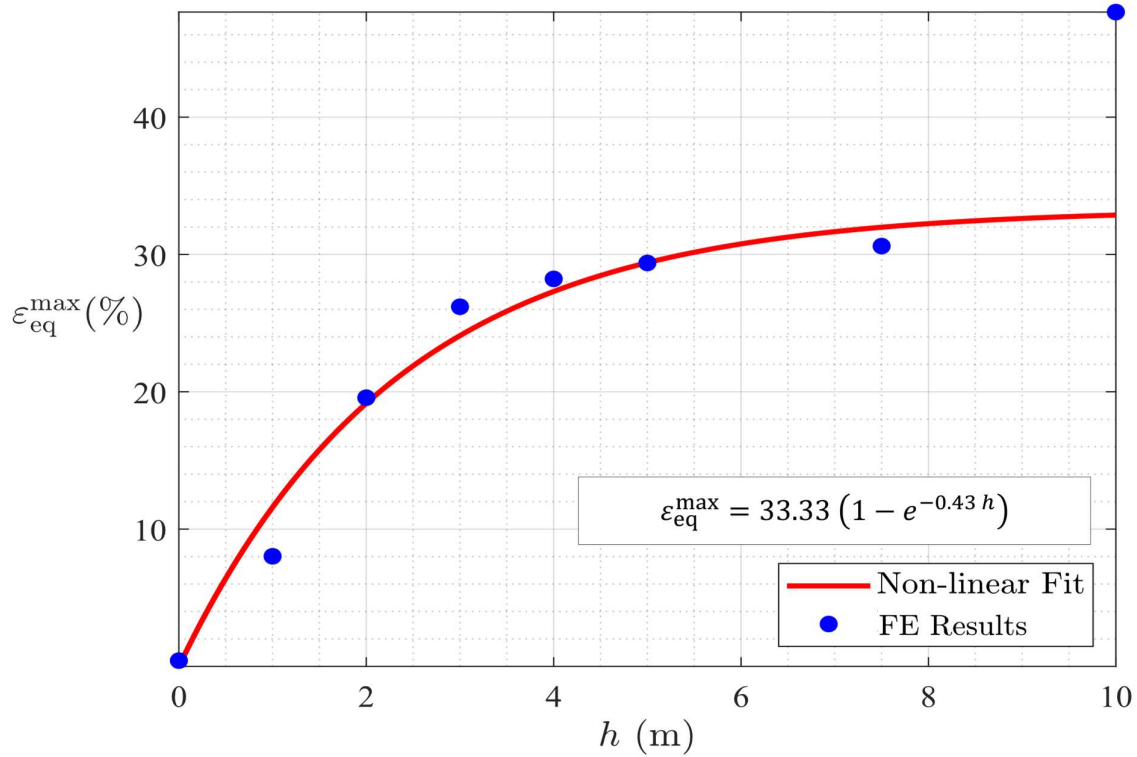


Figure 3.11. Plot of Max. Equivalent Plastic Strain (ε_{eq}^{\max}) vs. h (m)

3.2.1.2 Factor estimation for Maximum Equivalent Stress

The Maximum Equivalent Stress developed in the static structural simulation amounted to 138 Mpa. For the Transient simulations, the maximum stress value over time and space ranged from 203.08 Mpa (0 m height case) to 461.21 Mpa (7.5 m height case) with a slight dip in the value when the height was changed from 7.5 m to 10 m. It was observed that there was a sharp

increase in the value when the height increased to 1m, but this trend didn't continue as the height was increased. The eight stress factor values were obtained by comparing the maximum values of each transient analysis to the static analysis. The equation of the non-linear fit obtained after fitting this data to Eqn. 3.2 is given by Eqn. 3.5. The raw data along with the fitted curve is shown in Figure 3.12.

$$f_{\sigma_{eq}^{max}} = 1.47 + 1.71 (1 - e^{-1.85 h}) + 0.02 h \quad 3.5$$

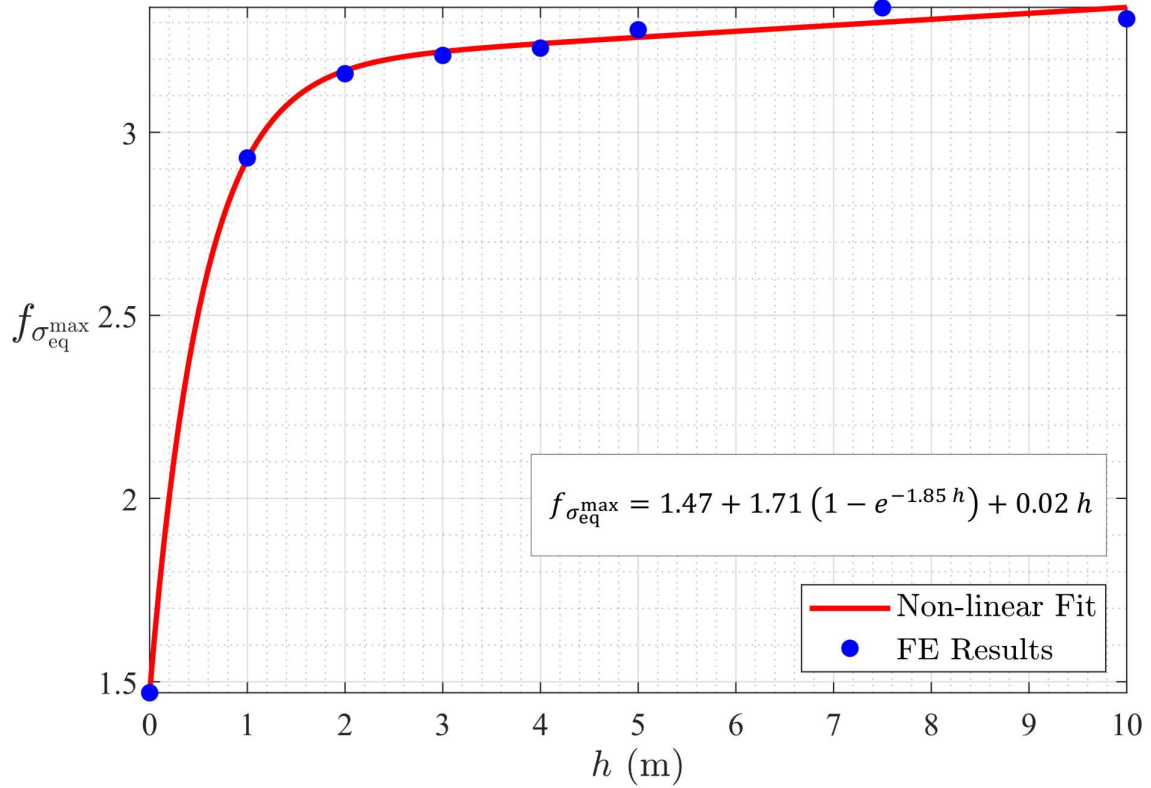


Figure 3.12. Plot of the Stress factor ($f_{\sigma_{eq}^{max}}$) vs. h (m) comparing the Fit.

3.2.1.3 Factor estimation for Maximum Roof Force

While inspecting the Roof Force results across all the transient simulations, a pattern was established. Firstly, the maximum value of the Roof Force over time and space was recognized and recorded for all the different heights. The car frame experienced a maximum force of 10.53 kN in the static analysis and 293.96 kN when the trunk fell from 10 meters of height. A sharp spike in the maximum roof force value from 13.89 kN to 69.73 kN was observed when the height of fall increased from 0 m to 1 m. These values were then individually divided with the

maximum roof force obtained from the static simulation. As a result, a set of eight dimensionless factors were obtained. After plotting and analysing these factors against the height of fall as shown in Figure 3.13, an approximate relation was established which is represented by Eqn. 3.6.

$$f_{F_R}^{\max} = 2.29 h + 2.86 \quad 3.6$$

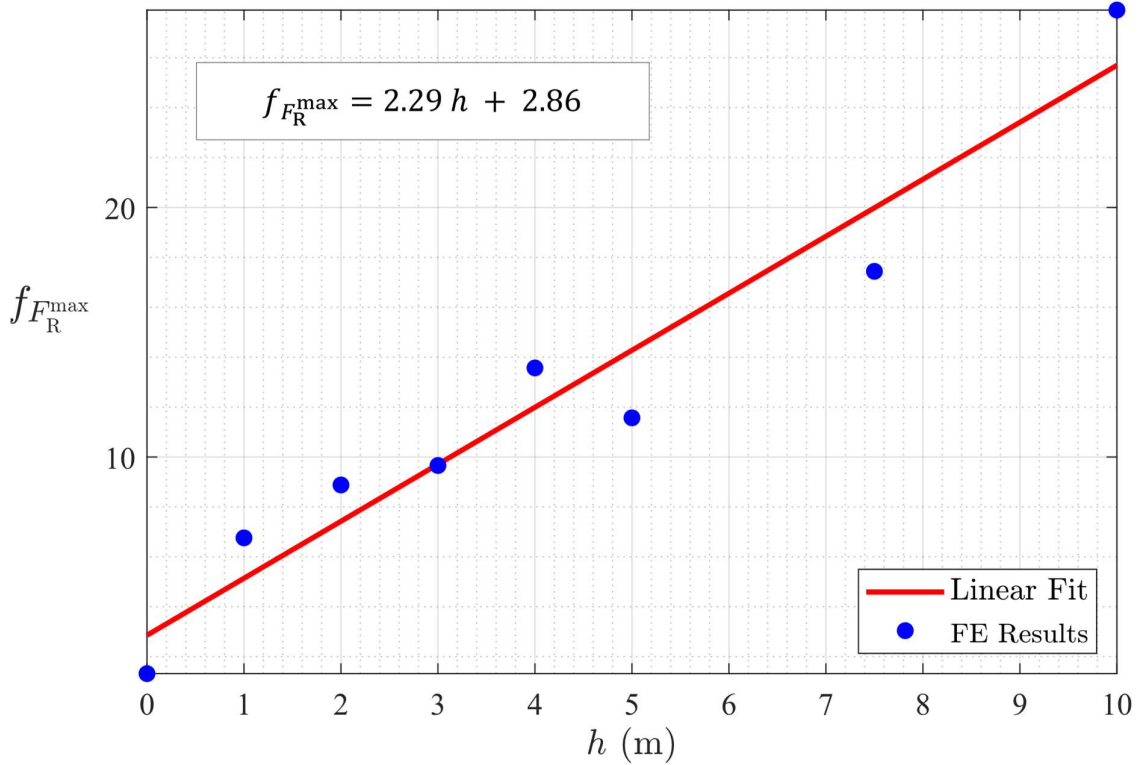


Figure 3.13. Plot of the Roof Force factor ($f_{F_R}^{\max}$) vs. h (m) comparing the Fit.

3.2.1.4 Factor estimation for Maximum Spring Force

The maximum value of the Spring Force obtained from the Static Analysis was 3.59 kN. Analysing the spring forces across all the transient simulations revealed that there was a gradual linear increase in the spring forces beyond the height of 3 m. A sudden jump of almost three times from 5.94 kN to 17.17 kN was recorded when the height increased to 1 m from 0 m. The value reached 38.32 kN when the height reached 2 m. On further increasing the height to 3 m, the value dipped a bit to 36.21 kN. Beyond this height, an approximate linear increase was observed as shown in Figure 3.14. The equation of the non-linear fit is given by the Eqn. 3.7.

$$f_{F_S}^{\max} = 1.41 + 6.51 (1 - e^{-0.78 h}) + 1.11 h \quad 3.7$$

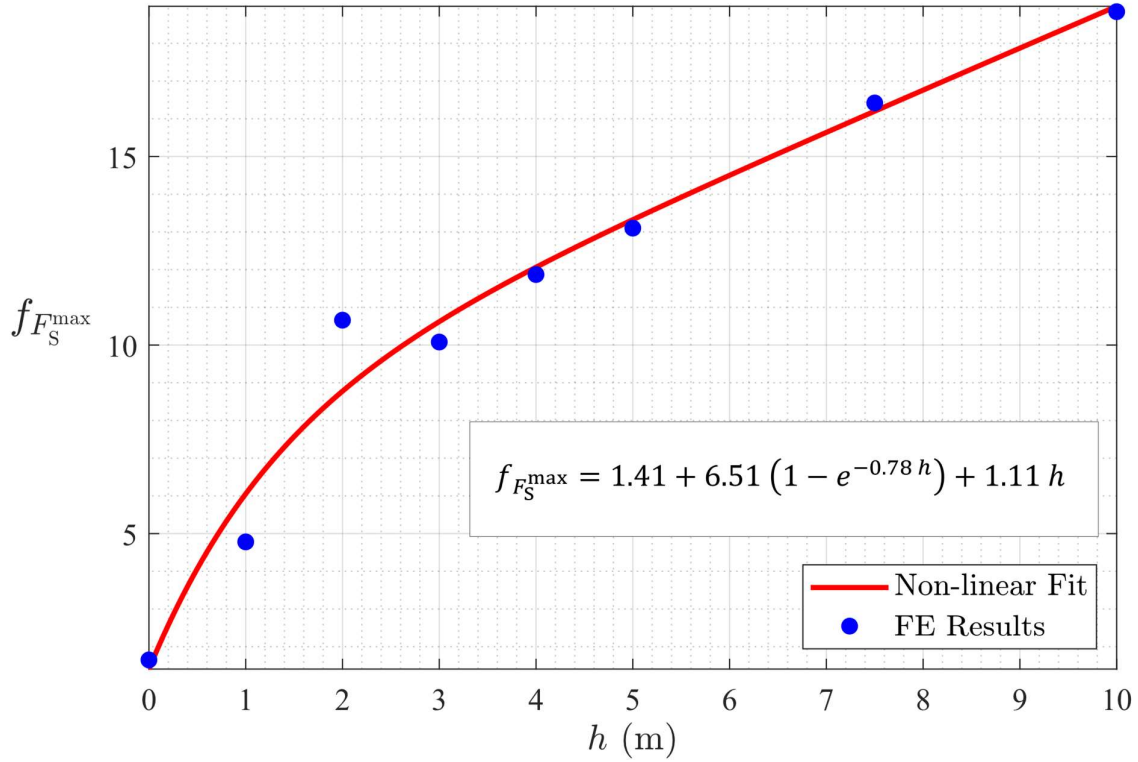


Figure 3.14. Plot of the Spring Force factor ($f_{F_S}^{\max}$) vs. $h \text{ (m)}$ comparing the Fit.

3.2.1.5 Factor estimation for Maximum Damping Force

Damping Forces cannot be obtained for Static simulations. To counter this problem and maintain continuity, the damping forces extracted from the transient simulations were factored against the Total maximum suspension force over space obtained from the static simulation. This value amounted to 3.59 kN which is equal to the maximum spring force obtained due to the absence of damping. A closer inspection revealed that the pattern of the damping forces for different heights was similar to that of the spring forces with a couple of differences. For the 0 m height of free fall, the maximum damping force amounted to 0.78 kN which is way less than the spring force for the same height. When the height was increased to 1 m, the maximum damping force increased to 4.78 kN i.e., a bump of more than six times compared to the 0 m height scenario. The gap between the maximum forces of the 2 m and 1 m height of free fall decreased but the dip from 2 m to 3 m remained almost the same. After plotting and analysing

these factors against the height of fall as shown in Figure 3.15, the equation of the non-linear fit obtained is given by the Eqn. 3.8.

$$f_{F_D}^{\max} = 0.21 + 1.38 (1 - e^{-1.46 h}) + 0.16 h \quad 3.8$$

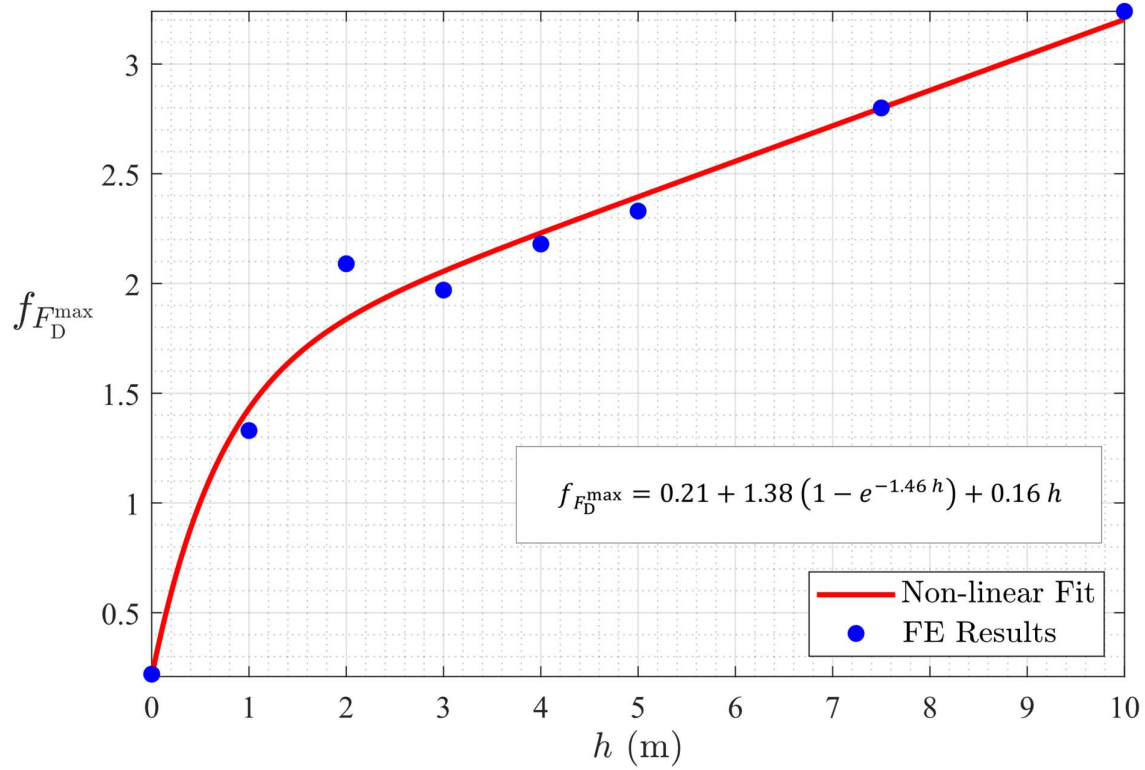


Figure 3.15. Plot of the Damping Force factor ($f_{F_D}^{\max}$) vs. h (m) comparing the Fit.

3.2.1.6 Factor estimation for Maximum Suspension Force

A Maximum Total Suspension Force of 3.59 kN was obtained from the Static Simulation. Analysing the results from the transient simulations revealed that the pattern followed by the Maximum Total Suspension Forces over time and space with varying heights was identical to that of the Spring Forces. There weren't any noticeable differences in the pattern except for a slight increase in the numerical values when compared to that of the Spring Forces. The least value of 6.07 kN was obtained for the simulation with 0 m free fall height, whereas the highest of 68.51 kN was found when the free fall height was increased to 10 m. The Eqn. 3.9 gives the non-linear fit obtained. The FE Result data along with the fitted curve is shown in Figure 3.16.

$$f_{F_T}^{\max} = 1.69 + 10.3 (1 - e^{-0.39 h}) + 0.69 h \quad 3.9$$

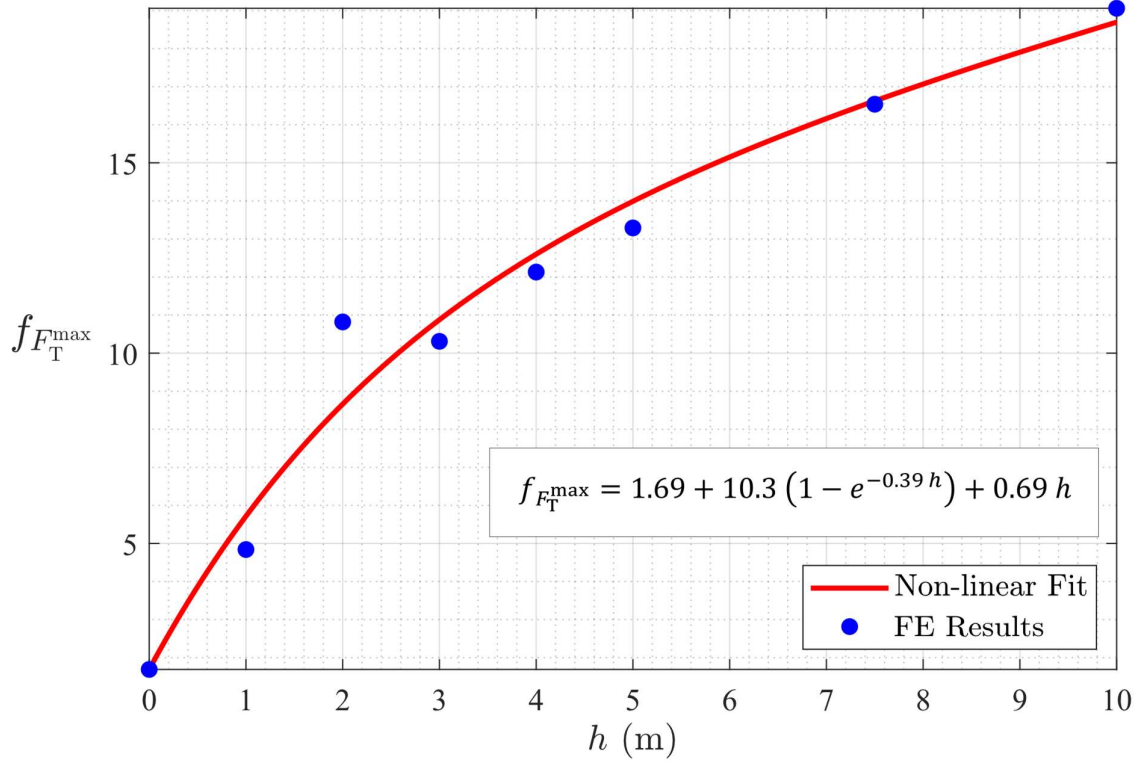


Figure 3.16. Plot of the Total Suspension Force factor ($f_{F_T}^{\max}$) vs. h (m) comparing the Fit.

3.2.1.7 Factor estimation for Maximum Roof Distortion

A Roof Distortion of approximately 1.1 cm occurred in the Static Simulation. The Roof Distortion was calculated by finding out the difference between the total deformation of the Roof Rim and the edge of one of the side pillars attached to the roof. These values were extracted from the last converged substep at $t = 1$ s. The amount of Roof Distortion keeps on increasing rapidly from 2.1 cm at 0 m height to 4.8 cm at 1 m height and 8.9 cm at 2 m height as shown in Figure 3.17. This rapid increase stopped beyond the 3 m height mark and a nominal steady increase was observed till $h = 10$ m where the Roof Deformation amounted to 17.2 cm approximately. Eqn. 3.10 represents the final equation of the non-linear fit obtained.

$$f_{u_R}^{\max} = 1.51 + 10.68 (1 - e^{-0.38 h}) + 0.4 h \quad 3.10$$

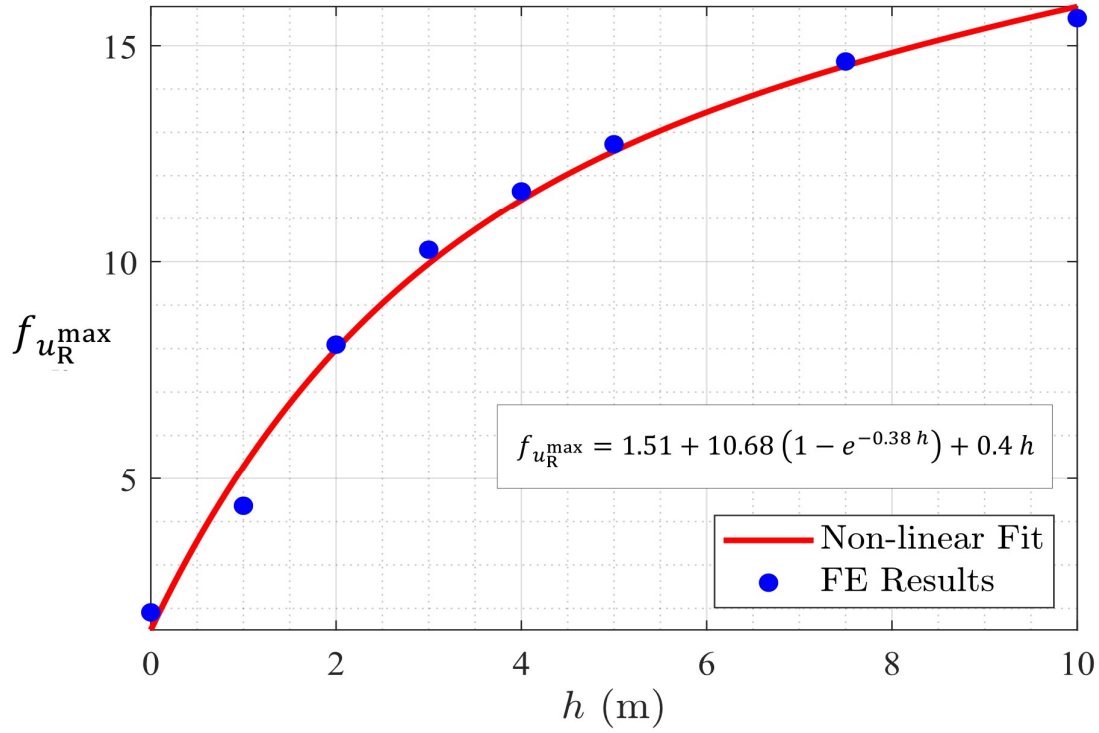


Figure 3.17. Plot of the Roof Distortion factor ($f_{u_R}^{\max}$) vs. h (m) comparing the Fit.

All the constants obtained for all the different parameters have been listed in **Table 3.5** along with the respective E_{rms} values obtained while fitting the curves.

Parameter	f_0	f_Q	b	f_m	E_{rms}
$\sigma_{\text{eq}}^{\max}$	1.47	1.71	1.85	0.02	0.18
F_R^{\max}	2.86	0	0	2.29	0.81
F_S^{\max}	1.41	6.51	0.78	1.11	0.55
F_D^{\max}	0.21	1.38	1.46	0.16	0.58
F_T^{\max}	1.69	10.3	0.39	0.69	0.64
u_R^{\max}	1.51	10.68	0.38	0.4	0.39

Table 3.5. Tabulation of the values of constants obtained for all the different parameters.

3.3 Simulations with $h = 5$ m using three Different Materials

A set of three Transient Simulations were performed with the height of free fall of the tree trunk set to 5 m. All the simulations were conducted using different materials in the car frame namely,

- Two variants of UHSS – (i) Baseline sample, (ii) Welded Sample
- One variant of AHSS – DP 350/600

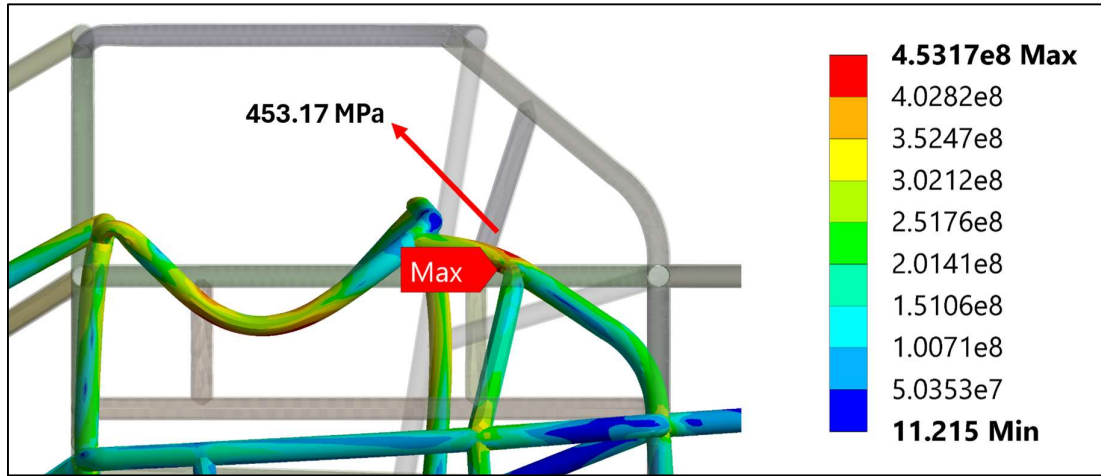
Seven parameters namely, the Equivalent Plastic Strain (ϵ_{eq}), Equivalent Stress (σ_{eq}), Roof Force (F_R), Suspension Spring Force (F_S), Suspension Damping Force (F_D), Total Suspension Force (F_T), and the Roof Distortion (u_R) were taken into consideration. The maximum values obtained from for all the above parameters are listed below in Table 3.6.

Parameter	UHSS heat Treated	DP 350-600	UHSS Baseline
ϵ_p^{\max} (%)	29.38	25.52	13.14
σ_{eq}^{\max} (MPa)	453.17	668.14	1431.12
F_R^{\max} (kN)	121.86	160.06	256.53
F_S^{\max} (kN)	47.09	49.43	54.79
F_D^{\max} (kN)	8.39	9.79	12.15
F_T^{\max} (kN)	47.77	49.97	55.42
u_R^{\max} (cm)	14.0	11.2	5.6

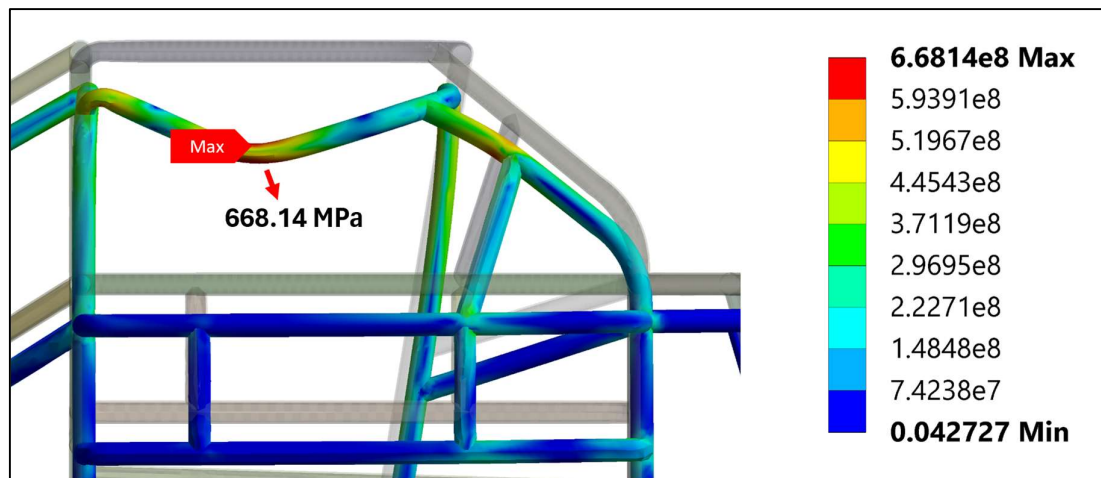
Table 3.6. Tabulation of the Maximum values of Equivalent Plastic Strain (ϵ_{eq}), Equivalent Stress (σ_{eq}), Roof Force (F_R), Suspension Spring Force (F_S), Suspension Damping Force (F_D), Total Suspension Force (F_T), and Roof Distortion (u_R) for the materials UHSS Heat Treated, DP 350-600, and UHSS Baseline

3.3.1.1 Maximum Stress developed in the car frame for different materials

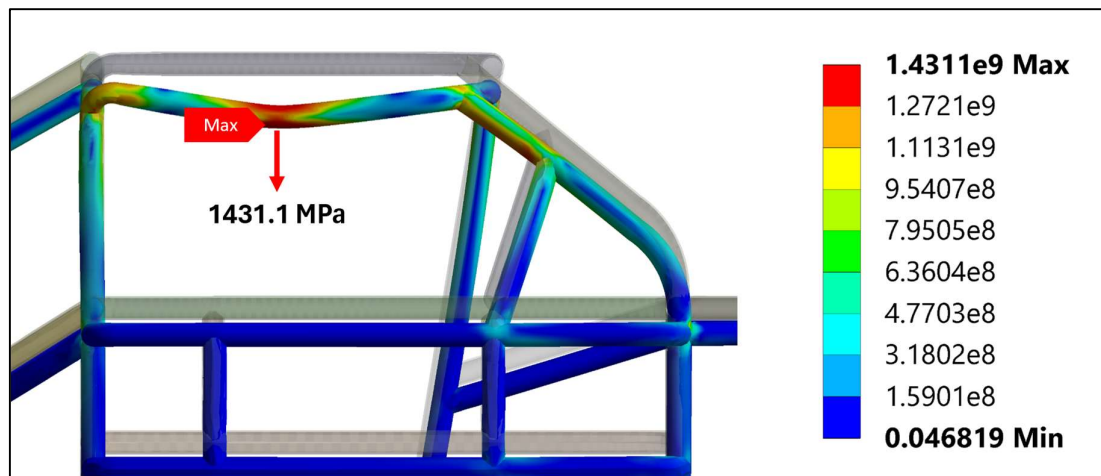
For the materials UHSS – Heat Treated and UHSS – Baseline, the location where maximum stress develops in the frame was the same as shown in the Figure 3.18 (a) and Figure 3.18 (c). A maximum stress of 668.14 MPa was developed in the bent part of the roof rim for the material DP 350-600 as shown in Figure 3.18 (b).



(a)



(b)



(c)

Figure 3.18. The Maximum Equivalent Stress (σ_{eq}^{max}) developed in the model with frame material as (a) UHSS Heat Treated, (b) DP 350-600, and (c) UHSS Baseline.

3.3.1.2 Deformation of the car frame for different materials

The Total Deformation of the roof structure at the end of 1 s consisted of two separate entities namely; the roof displacement and the roof distortion. The summation of these two gives the Total Roof Deformation (u_{TD}). After noting the maximum value of this parameter across all simulations with the three different materials, the least deformation was observed with the UHSS Baseline material, and the maximum occurs in the simulation with the UHSS Heat Treated material as listed in Table 3.7.

Material	u_{TD}^{\max} (cm)
UHSS - Heat Treated	34.20
DP 350-600	27.90
UHSS - Baseline	17.86

Table 3.7. Maximum value of Roof Distortion (u_{TD}) for the materials UHSS Heat Treated, DP 350-600, and UHSS Baseline

Figure 3.7, Figure 3.19, and Figure 3.20 represent the Total Deformation of the car frame at the end of one second for the materials UHSS Heat Treated, DP 350-600, and UHSS Baseline respectively. Part (a) of all the figures represent the isometric view of the deformed frame with the tree trunk partially visible. This was done to show the roof surface deformation without being hindered by the trunk. A roof distortion of 14 cm accompanied by a roof deformation of 34.2 cm was observed in Figure 3.7 which represents the simulation result of the material – UHSS Heat Treated. This material exhibited the largest deformation among the three while the least occurred when the material was changed to the Baseline variant of UHSS. Figure 3.20 shows that the latter had a distortion of approximately 5.6 cm with a deformation of 17.86 cm. The car frame using the material DP 350-600 had a roof distortion of 11.2 cm 27.9 cm of total deformation at $t = 1$ s as shown in Figure 3.19.

For UHSS – Heat Treated, an upward bending was observed in the rear section of the frame represented by Figure 3.7 (b). This bending was negligible for the other two materials as observed in Figure 3.19 (b) and Figure 3.20 (b).

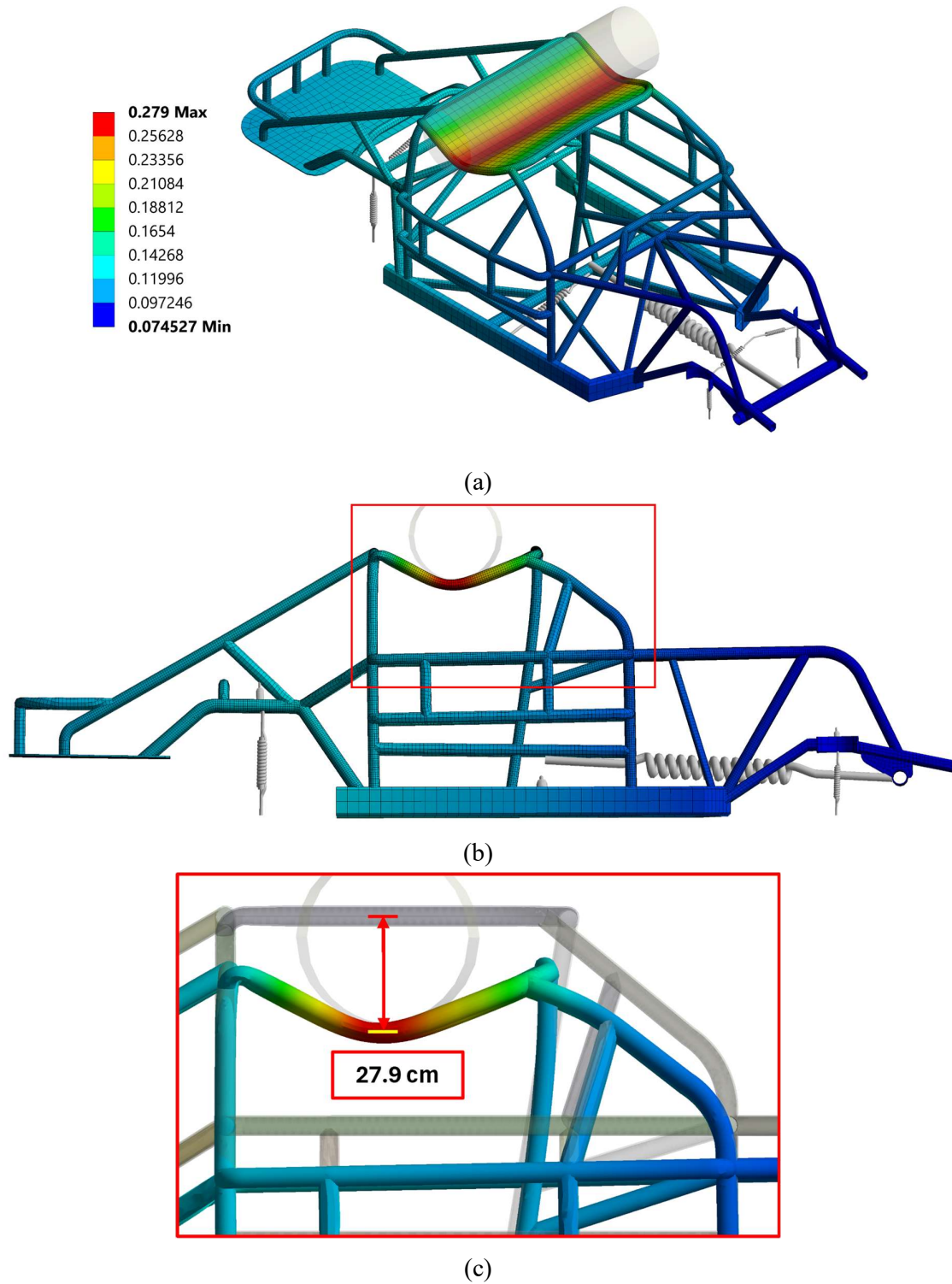


Figure 3.19. Total Deformation across the (a) whole Car Frame in Isometric View, (b) whole Car Frame from Side View, and (c) enlarged portion of the side view emphasizing the Roof Deformation for the Transient Analysis at $t = 1$ s using DP 350-600 as the material.

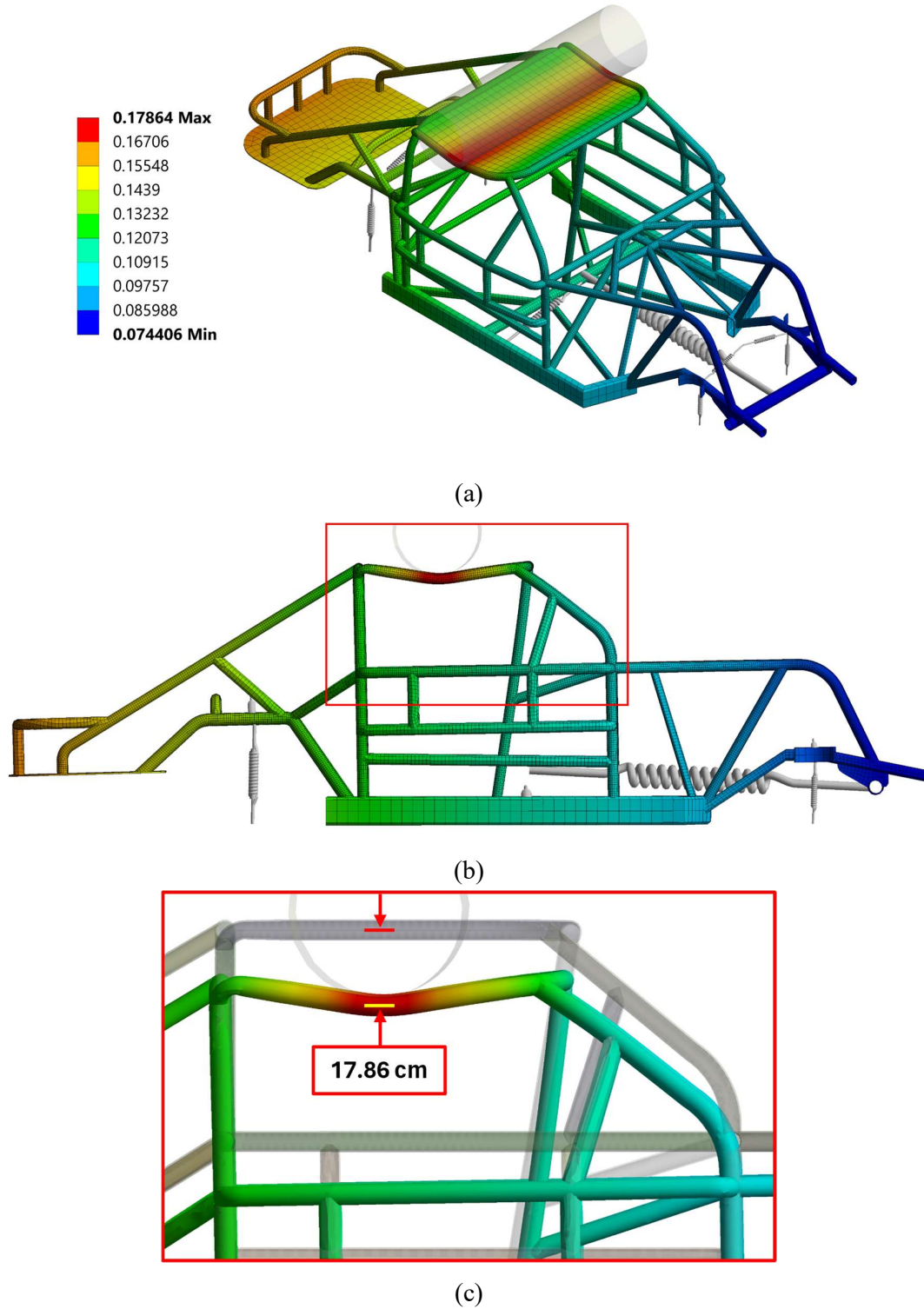
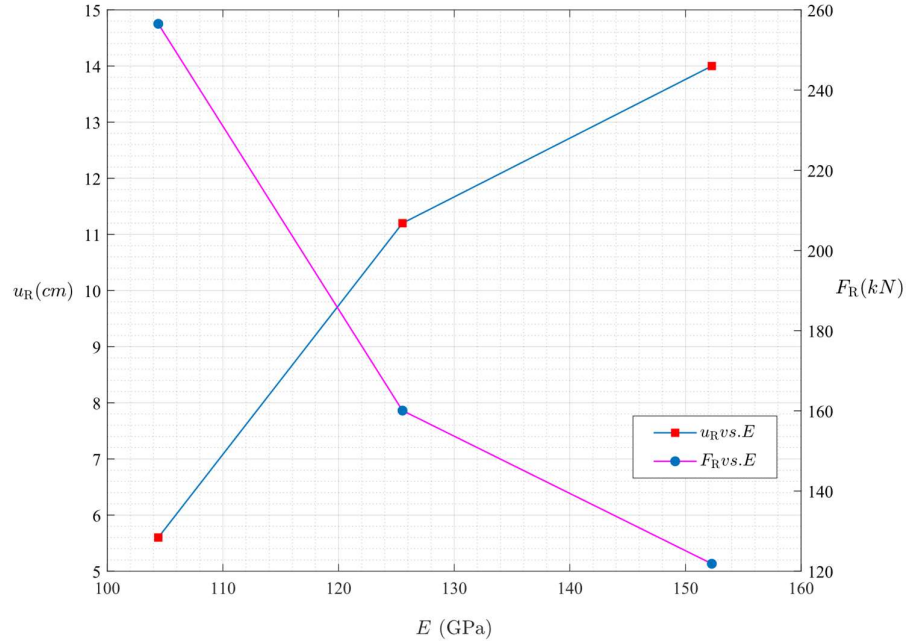


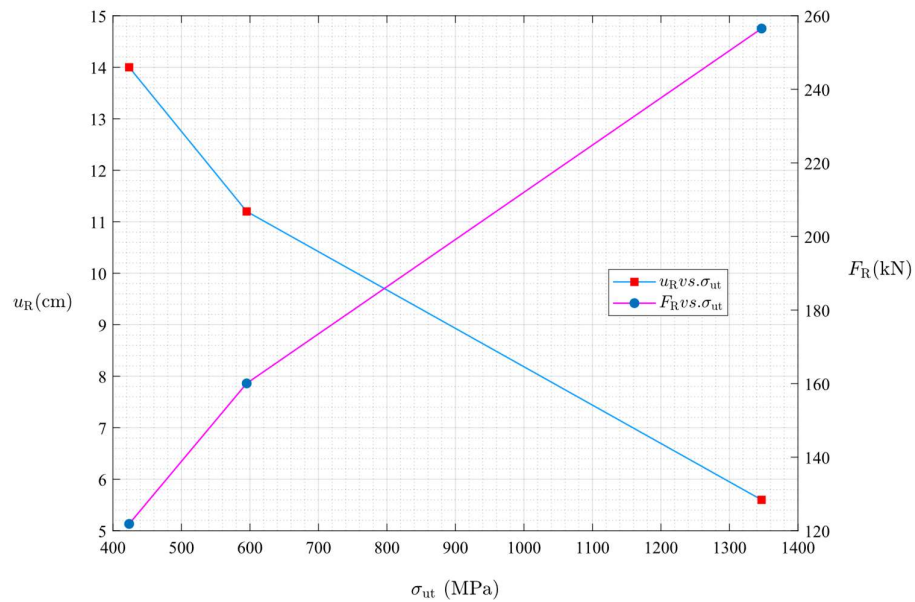
Figure 3.20. Total Deformation across the (a) whole Car Frame in Isometric View, (b) whole Car Frame from Side View, and (c) enlarged portion of the side view emphasizing the Roof Deformation for the Transient Analysis at $t = 1\text{ s}$ using UHSS – Baseline as the material.

3.3.1.3 Variance of u_R and F_R pertaining to Material Parameters

Figure 3.21 depicts the variation of the Roof Distortion (u_R) and Roof Force (F_R) due to the change in the Young's Modulus (E) and Ultimate Tensile Strength (σ_{ut}) of materials.



(a)



(b)

Figure 3.21. Variation of the Roof Force (F_R) and Roof Distortion (u_R) with (a) Young's Modulus (E), and (b) Ultimate Tensile Strength (σ_{ut}) of the materials.

3.4 Force vs. Time behaviour for $h = 5$ m using UHSS – Heat Treated as the material

The Roof Force (F_R) as shown in Figure 3.22, has a spike of 121.86 kN in the negative y-direction when the contact with the tree trunk occurs. A second spike was observed at $t = 0.11$ s when the suspensions reached the maximum compression after which the car tried to push the trunk upwards. F_R was 0 from $t = 0.21$ s after the car pushed away the trunk until $t = 0.51$ s when the trunk impacted the car for a second time. Beyond $t = 0.6$ s, a damped harmonic motion is seen till $t = 1$ s.

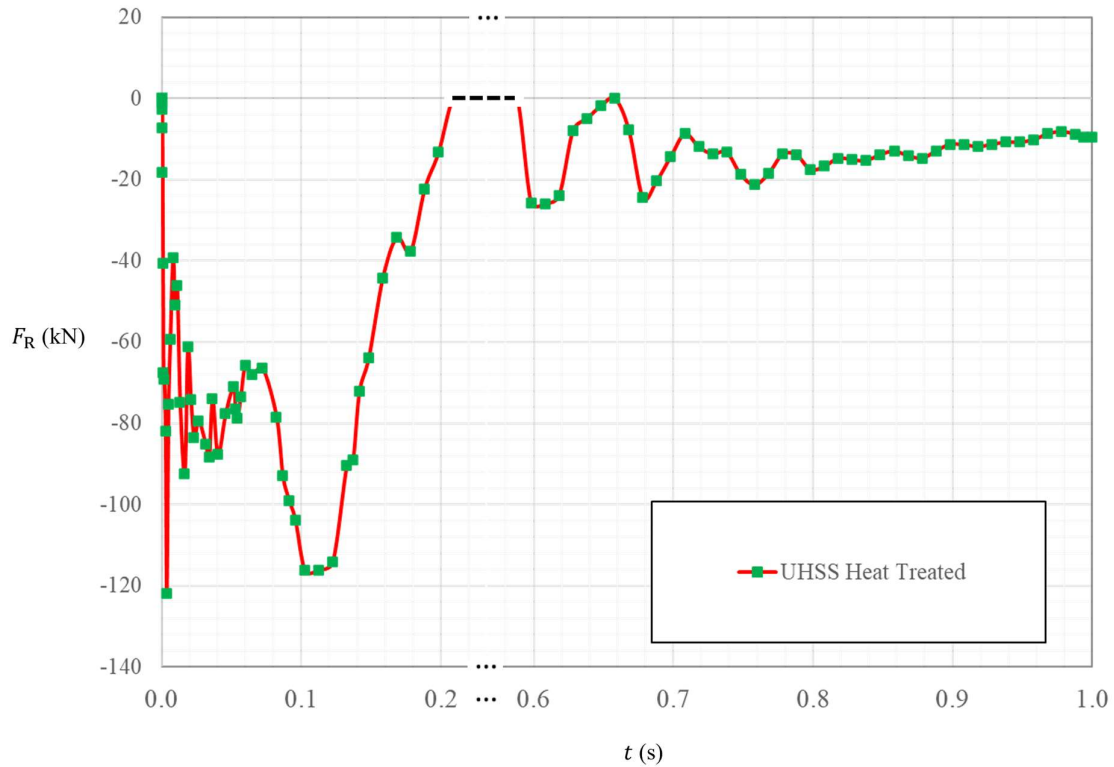
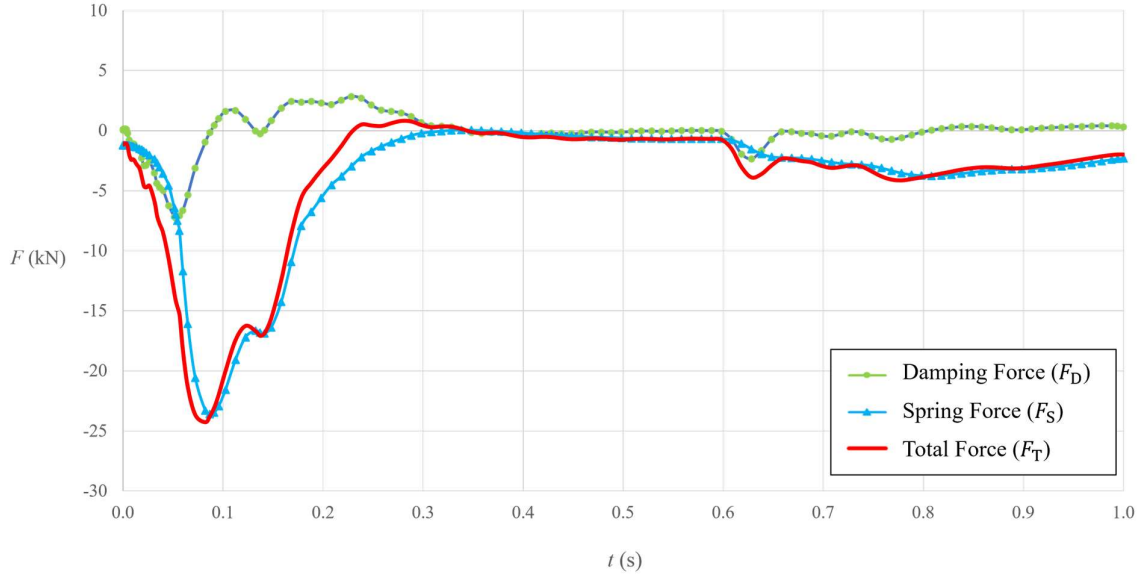


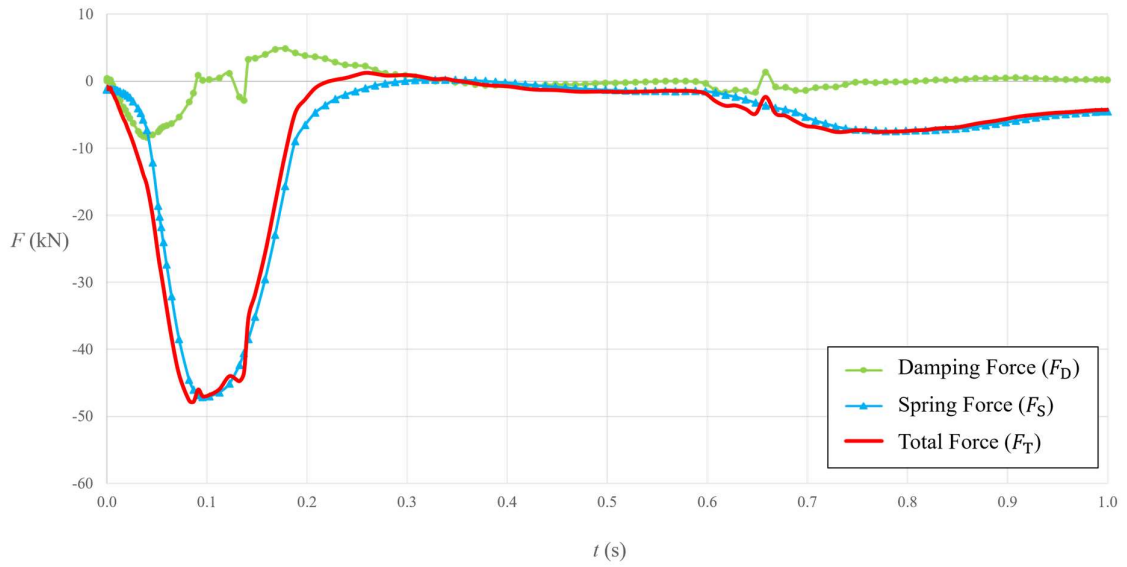
Figure 3.22. Dependence of the Roof Force (F_R) on time (t) when $h = 5$ m and UHSS – Heat Treated was the material used.

The Total Suspension force (F_T) along with the Spring (F_S) and Damping Forces (F_D) were plotted against time for both the Rear and Front wheel suspensions. A clear difference in the range of values was observed due to the uneven balance of the tree trunk forces on the car. The initial spring force was the same for both wheels, but the initial damping force showed a deviation. As time progressed, the spring and damping forces on the rear suspension increased

as the trunk was comparatively closer to the rear wheels than the front. The time dependent behaviour of the suspension forces for the 5 m height Transient simulation is depicted in Figure 3.23.



(a)



(b)

Figure 3.23. Dependence of the Damping Force (F_D), Spring Force (F_S), and Total Suspension Force (F_T) on time (t) for (a) the Front Wheel Suspension and (b) the Rear Wheel Suspension when $h = 5$ m and UHSS – Heat Treated was the material used.

Chapter 4: Conclusion and Future Work

4.1 Conclusion

The car frame was analysed under quasi-static and dynamic conditions and the results were extracted. Observing the results revealed that the frame did not undergo any plastic deformation when loaded under quasi-static conditions i.e., the weight of the tree trunk gradually fell on the roof. On the other hand, changing to dynamic loading caused a plastic strain of 0.42 %.

From the simulation results, it was evident that the roof of the car kept crumbling to a dangerous amount as the height of free fall of the trunk gradually increased beyond 1 m. The material started to locally undergo heavy plastic strain reaching slightly above 30% when the trunk fell from a 5 m height above the roof. Maximum plastic strain was observed locally at the location where the trunk and the roof made contact. For some cases, the maximum was also observed in the location where the rim of the roof was connected to the supporting pillars.

The roof of a car doesn't have any kind of safety mechanism to prevent passenger injury. The intrusion of the roof into the passenger cabin i.e., the roof distortion exceeded 8 cm when the height of fall was increased to 2 m. This can have the potential to cause serious injuries due to decreased passenger headroom.

The material of the car structure plays a crucial role in deciding the amount of roof intrusion. A material with a greater ultimate strength will allow less intrusion. Conversely, increasing the strength will decrease the cushioning effect of the structure.

The cushioning effect offered by the roof and the frame structure along with the suspension was prominent when the height of free fall of the trunk was under 2 m. This effect gradually became negligible when the impact velocity exceeded 7 m/s.

Most of the structural deformation happens within 100 to 150 ms of time which doesn't give much time to the passengers and might transform the impact to a fatal one. As observed, this kind of impacts can be much more severe than a vehicular rollover.

From this aggregation, an approximate prediction can be made to estimate the forces acting on the roof when compared to static behaviour which is still the trademark to formulate the Roof Strength of a passenger car.

4.2 Future Scope of Work

In a more practical scenario, a tree trunk would not fall in a perfectly horizontal alignment on the car roof. Instead, it would rotate about its base (where it's rooted to the soil) and fall on one side of the roof in an oblique orientation as shown in Figure 4.1 (a). This would result in an unequal distribution of the trunk weight leading to a greater amount of damage on the side where it would make initial contact.

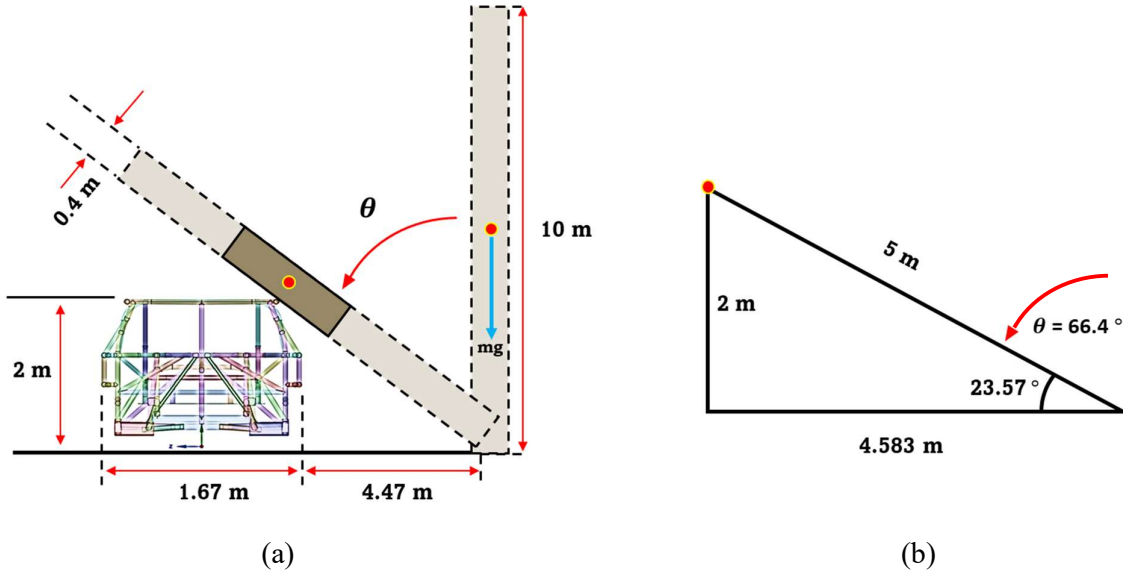


Figure 4.1. (a) Diagrammatic representation of the phenomenon when the tree trunk falls on the car roof in an oblique orientation. (b) Schematic showing the angle of orientation of the trunk with respect to the road and its original position.

The dimensions shown in Figure 4.1 (b) are calculated based on the following parameters.

1. The width of the road is assumed to be 9 m, which is the average width of a Major District Road (MDR) in India [57]. So, the resulting width of a single lane will be 4.5 m.
2. It is assumed that the car is parked perfectly in the middle of a single lane resulting in a distance of 2.25 m from the edge of the road between the tree and the car.
3. For the sake of convenience and due to the lack of relevant data, the distance between the edge of the road and the tree is assumed to be 3.05 m.
4. The distance of 3.05 m is assumed based on the guideline of 5-6 m distance between trees and road edge for highways (>12 m in width) [58].
5. The distance between the roof and the road is taken as 2 m assuming a standard passenger

car tyre parameter “195/60 R16” [59] which results in an outer tyre diameter of approximately 525 mm.

Figure 4.2 shows the whole model of the car and the trunk which could be used. Assuming a distance of 3.05 m between the edge of the road and the tree can simplify the problem related to the location of the point mass of 1074 kg. The gap of 3.05 m will assure that the centre of gravity of the trunk will be located very close to the location of impact. The trunk model will have the exact same dimensions as the one used for this study. Its orientation could be set at an angular distance of 23.57° from the ground i.e., 66.4° with the global positive y axis. A coordinate system could then be created at the point which replicates the location where the tree trunk attaches to the ground. The created coordinate system could then be aligned with the principal axis of the trunk. A remote boundary condition could be given to the trunk so that it can only rotate about the x axis of the new coordinate system.

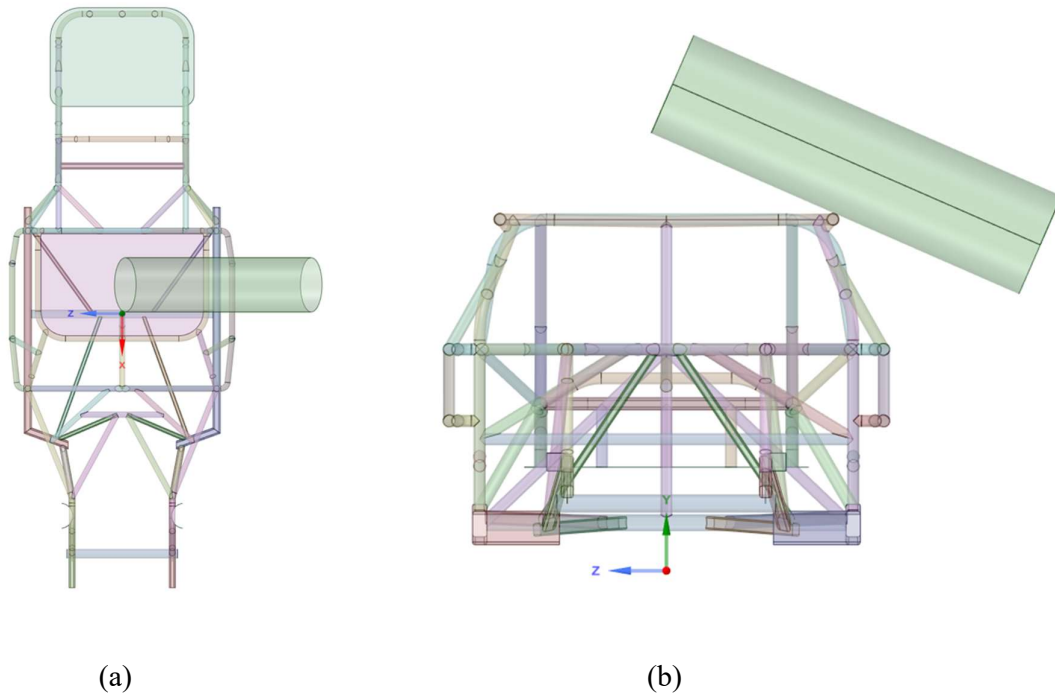


Figure 4.2. (a) Top view of the complete model. (b) Front view of the complete model.

The nodal coordinate system of the point mass (“MASS21” element) could be rotated to align it with the principal axis of the trunk with the help of the “NROTAT” command in the APDL code window. “KEYOPT (2)” of the “MASS21” element will be changed to “1”. This would align the Element coordinate system with the Nodal coordinate system. As a result of this

alignment, the Element coordinate system of the “MASS21” element would also be aligned with the Principal coordinate system of the tree trunk.

The coefficient of sliding friction between the tyres and the road varies from 0.7 (wet road) to 0.9 (dry road) [44, 45]. The spring stiffness of the spring aligned with the global z direction could be taken as 21.6 kN/m to account for the sliding friction. Alternatively, a non-linear spring can be declared with a constant value of force for all spring displacements. The challenge being the estimation of this force due to the contribution from the dynamic loading of the trunk.

In the Design Modeller, a solid cylinder with the entire dimensions of the tree trunk could be created. The principal axis of the cylinder being aligned to the global z axis. The moments of inertia of the cylinder would be noted.

The “ESEL” command followed by the “NSLE” command can be utilized to select all the nodes on the shell bodies of the trunk. After the node selection, the “NROTAT” command would be implemented to align them with the new coordinate system.

The initial angular velocity ($\dot{\theta}$) of the trunk just before its impact with the roof could be calculated with the help of the law of conservation of energy. The reduction in potential energy of the trunk due to the fall should be equal to the kinetic energy with which it hits the roof. This statement can be represented with Eqn. 4.1.

$$M_t g (\Delta u_{cg}) = \frac{1}{2} I_t \dot{\theta}^2 \quad 4.1$$

For a solid cylinder of mass M_t and length L , the moment of inertia I_t is given by Eqn. 4.2.

$$I_t = \frac{M_t L^2}{3} \quad 4.2$$

The Eqn. 4.1 can be simplified using Eqn. 4.2 to calculate the angular velocity which is given by the Eqn. 4.3. The value of $\dot{\theta}$ was calculated as 1.33 rad/s.

$$\dot{\theta} = \sqrt{\frac{6g (\Delta u_{cg})}{L^2}} \quad 4.3$$

Finally, the “IC” command can be administered to provide $\dot{\theta}$ (“ROTX”) to the tree trunk.

References

- [1] “How are traffic accidents defined?: FAQ: Morelli Law Firm,” Morelli Law, May 14, 2023.
- [2] “Road traffic injuries,” World Health Organization, Jun. 20, 2022.
- [3] Progressive Corporation, “What is a rollover car accident?,” Mar. 07, 2023.
- [4] NHTSA, “Crashworthiness,” United States Department of Transportation, Oct. 2010.
- [5] Robert Hurlston, “Isotropic, kinematic or mixed-mode? which hardening model for YOUR ABAQUS FEA analysis?,” Fidelis, Jan. 28, 2021. <https://www.fidelisfea.com/post/isotropic-kinematic-or-mixed-mode-which-hardening-model-for-your-abaqus-fea-analysis> (accessed Aug. 23, 2023).
- [6] M. C. Araujo, “Non-linear kinematic hardening model for multiaxial cyclic Non-linear kinematic hardening model for multiaxial cyclic plasticity plasticity.” [Online]. Available: https://digitalcommons.lsu.edu/gradschool_theses
- [7] “Chapter 4 Static Structural Analysis,” 2009.
- [8] “In short explained: Linear and nonlinear structural analysis,” Femto Engineering, May 22, 2017.
- [9] “Transient Analysis,” Budapest University of Technology and Economics (BME), Jul. 14, 2017.
- [10] “Damping in FEA simulations: Materials,” SimScale, May 25, 2021.
- [11] R. Bosch, T. Lich, J. Moennich, and A. Georgi, “Girikumar Kumaresh Representativeness and Weighting Methods of Real Time Accident Data in India,” 2013.
- [12] “ROAD ACCIDENTS IN INDIA-2019 IR;es oot;rs.” [Online]. Available: www.morth.nic.in
- [13] “ROAD ACCIDENTS IN INDIA 2020 IR;es o t;rs.” [Online]. Available: www.morth.nic.in
- [14] B. Ross Silcock and R. Silcock, “Ross Silcock TRL Department for International Development Project R7780 Guidelines for Estimating the Cost of Road Crashes in

Developing Countries Final Report Department for International Development Guidelines for Estimating the Cost of Crashes in Developing Countries,” 2003.

- [15] G. Kumaresh, F. Saldanha, T. Lich, and J. Moennich, “Estimation of Socio-Economic Loss due to Road Traffic Accidents in India,” in SAE Technical Papers, SAE International, Sep. 2021. doi: 10.4271/2021-26-0012.
- [16] “THE TRUE COST OF ROAD CRASHES Valuing life and the cost of a serious injury.” [Online]. Available: www.irap.net
- [17] S. Wicaksono, M. Rizka Faisal Rahman, S. Mihradi, and I. Nurhadi, “Finite element analysis of bus rollover test in accordance with UN ECE R66 standard,” *Journal of Engineering and Technological Sciences*, vol. 49, no. 6, pp. 799–810, 2017, doi: 10.5614/j.eng.technol.sci.2017.49.6.7.
- [18] K. M. Dobbertin, M. D. Freeman, W. E. Lambert, M. R. Lasarev, and S. S. Kohles, “The relationship between vehicle roof crush and head, neck and spine injury in rollover crashes,” *Accid Anal Prev*, vol. 58, pp. 46–52, 2013, doi: 10.1016/j.aap.2013.04.020.
- [19] G. C. Rains and J. N. Kaniyanthra, “Determination of the Significance of Roof Crush on Head and Neck Injury to Passenger Vehicle Occupants in Rollover Crashes,” *SAE Transactions*, vol. 104, pp. 1238–1248, 1995, [Online]. Available: <http://www.jstor.org/stable/44612284>
- [20] S. P. Burns, R. P. Kaufman, C. D. Mack, and E. Bulger, “Cost of spinal cord injuries caused by rollover automobile crashes,” *Injury Prevention*, vol. 16, no. 2, pp. 74–78, Apr. 2010, doi: 10.1136/ip.2008.021097.
- [21] National Highway Traffic Safety Administration (NHTSA), “Federal Motor Vehicle Safety Standards; Roof Crush Resistance,” DEPARTMENT OF TRANSPORTATION, 2005, Accessed: Jul. 03, 2023. [Online]. Available: https://www.nhtsa.gov/sites/nhtsa.gov/files/216_snprm_final_version_jan_16rev.pdf
- [22] M. Mao, E. C. Chirwa, and W. Wang, “Assessment of vehicle roof crush test protocols using FE models: Inverted drop tests versus updated FMVSS No. 216,” *International Journal of Crashworthiness*, vol. 11, no. 1, pp. 49–63, 2006, doi: 10.1533/ijcr.2005.0383.
- [23] Tamaghna Banerjee, “Kolkata: Near escape for driver as tree falls on car,” *The Times of India*, Feb. 02, 2018. <https://timesofindia.indiatimes.com/city/kolkata/kolkata-near->

escape-for-driver-as-tree-falls-on-car/articleshow/62761061.cms (accessed Jul. 02, 2023).

- [24] Manoj Badgeri and Mateen Hafeez, “Tree Branch fall kills man in car near Mahalaxmi,” The Times of India, Nov. 22, 2022. <https://timesofindia.indiatimes.com/city/mumbai/tree-branch-fall-kills-man-in-car-near-mahalaxmi/articleshow/95672832.cms> (accessed Jul. 02, 2023).
- [25] “Bolt from the green: Delhi tree comes crashing on road,” The Times of India, Jul. 15, 2022. <https://timesofindia.indiatimes.com/city/delhi/bolt-from-the-green-delhi-tree-comes-crashing-on-road/articleshow/92886655.cms> (accessed Jul. 06, 2023).
- [26] Natalie Tan, “Tree Branch falls on car in Tiong Bahru, injuring driver,” SPH Media Limited, Mar. 30, 2021. <https://www.straitstimes.com/singapore/tree-branch-falls-on-car-in-tiong-bahru-injuring-driver> (accessed Jul. 06, 2023).
- [27] James Leclair, “Nascar Car of the Future Frame,” Grabcad, May 10, 2014. <https://grabcad.com/library/nascar-car-of-the-future-frame-1> (accessed Jul. 06, 2023).
- [28] H. Nagendra and D. Gopal, “Street trees in Bangalore: Density, diversity, composition and distribution,” *Urban For Urban Green*, vol. 9, no. 2, pp. 129–137, 2010, doi: 10.1016/j.ufug.2009.12.005.
- [29] B. Tamang Uttar Banga Krishi Vishwavidyalaya, N. A. Pala, B. Chandra Sarkar, and G. Shukla Uttar Banga Krishi Vishwavidyalaya, “Wood specific gravity of some tree species in sub-tropical humid climate in India Himalayan forest ecosystem View project Communication skills & Personality development View project,” 2019. [Online]. Available: <https://www.researchgate.net/publication/334193396>
- [30] A. Arankalle, “Advances in light weight materials for body-in-white (BIW),” *Lecture Notes in Mechanical Engineering*, vol. PartF9, pp. 517–525, 2017, doi: 10.1007/978-981-10-1771-1_55.
- [31] P. U. Shiva, R. B. Athota, and S. Bandu, “Automotive Chassis Design Material Selection for Road and Race Vehicles Flight Demonstrator View project CFD Analysis View project.” [Online]. Available: <https://hal-mines-albi.archives-ouvertes.fr/hal-02519178>
- [32] M. Tisza and I. Czinege, “Comparative study of the application of steels and aluminium in lightweight production of automotive parts,” *International Journal of Lightweight*

- Materials and Manufacture, vol. 1, no. 4, pp. 229–238, Dec. 2018, doi: 10.1016/j.ijlmm.2018.09.001.
- [33] H. Hofmann, T. Heller, and S. Sikora, “(Design of) modern steels for automotive application,” in Materials Science Forum, Trans Tech Publications Ltd, 2010, pp. 3111–3116. doi: 10.4028/www.scientific.net/MSF.638-642.3111.
- [34] V. Sutar, C. S. Dharankar, and B. T. Raju, “High Strength Steel for Automotive Applications,” International Research Journal of Engineering and Technology, 2016, [Online]. Available: www.irjet.net
- [35] X. Hu and Z. Feng, “Advanced High-Strength Steel-Basics and Applications in the Automotive Industry,” 2021. [Online]. Available: www.osti.gov
- [36] M. Singh, W. : Www, and M. K. Singh, “Application of Steel in Automotive Industry To analyse the effect of ICE Downsizing and Downspeeding on Automotive Powertrain Vibrations View project Review of Vehicle Light Weighting Initiatives and Design Concepts View project International Journal of Emerging Technology and Advanced Engineering Application of Steel in Automotive Industry,” 2008. [Online]. Available: www.ijetae.com
- [37] G. Noorumar, D. Vysochinskiy, E. Englund, K. G. Robbersmyr, and S. Rogovchenko, “Effect of welding and heat treatment on the properties of UHSS used in automotive industry,” EPJ Web Conf, vol. 250, p. 05015, 2021, doi: 10.1051/epjconf/202125005015.
- [38] B. C. De Cooman, “Structure-properties relationship in TRIP steels containing carbide-free bainite,” Curr Opin Solid State Mater Sci, vol. 8, no. 3–4, pp. 285–303, 2004, doi: 10.1016/j.cossms.2004.10.002.
- [39] J. Chaboche and G. Rousselier, “On the Plastic and Viscoplastic Constitutive Equations-Part I: Rules Developed With Internal Variable Concept.” [Online]. Available: <https://minesparis-psl.hal.science/hal-03464390>
- [40] B. H. Cheong, J. Lin, and A. A. Ball, “Modelling of the hardening characteristics for superplastic materials,” Journal of Strain Analysis for Engineering Design, vol. 35, no. 3, pp. 149–157, 2000, doi: 10.1243/0309324001514314.
- [41] Wasee Syed, “Ansys plasticity models explained,” FEA Tips, Jan. 26, 2023.

- [42] J. L. Chaboche, "A review of some plasticity and viscoplasticity constitutive theories," *Int J Plast*, vol. 24, no. 10, pp. 1642–1693, Oct. 2008, doi: 10.1016/j.ijplas.2008.03.009.
- [43] Q. J. Ashraf, G. V. Prasad Reddy, R. Sandhya, K. Laha, and G. A. Harmain, "Simulation of low cycle fatigue stress-strain response in 316LN stainless steel using non-linear isotropic kinematic hardening model—A comparison of different approaches," *Fatigue Fract Eng Mater Struct*, vol. 41, no. 2, pp. 336–347, Feb. 2018, doi: 10.1111/ffe.12683.
- [44] C. Tong and T. Li, "Car Driving Safety Analysis in Rainy and Snowy Weather Based on ADAMS/Car," in *CICTP 2015*, Reston, VA: American Society of Civil Engineers, Jul. 2015, pp. 2895–2903. doi: 10.1061/9780784479292.266.
- [45] I. Kageyama, Y. Kuriyagawa, T. Haraguchi, T. Kaneko, M. Asai, and G. Matsumoto, "Study on the Road Friction Database for Automated Driving: Fundamental Consideration of the Measuring Device for the Road Friction Database," *Applied Sciences (Switzerland)*, vol. 12, no. 1, Jan. 2022, doi: 10.3390/app12010018.
- [46] J. A. Calvo, V. Dõ Âaz, and J. L. San Roma, "Establishing inspection criteria to verify the dynamic behaviour of the vehicle suspension system by a platform vibrating test bench," 2005.
- [47] A. Shirahatt, P. S. S. Prasad, P. Panzade, and M. M. Kulkarni, "Optimal design of passenger car suspension for ride and road holding," *Journal of the Brazilian Society of Mechanical Sciences and Engineering*, vol. 30, no. 1, pp. 66–76, 2008, doi: 10.1590/s1678-58782008000100010.
- [48] M. S. Mahmood, A. A. Nassar, and H. M. Mohammad, "Study of Performance of Incorporating Pneumatic Suspension System with the Hydraulic Actuator for Quarter Car and Using Controllers with Genetic Algorithm," *Instrumentation Measure Metrologie*, vol. 21, no. 4, pp. 151–158, Aug. 2022, doi: 10.18280/i2m.210405.
- [49] G. Ślaski, "DAMPING PARAMETERS OF SUSPENSION OF PASSENGER VEHICLE EQUIPPED WITH SEMI-ACTIVE DAMPERS WITH BY-PASS VALVE," 2011.
- [50] V. Guruguntla et al., "Ride comfort and segmental vibration transmissibility analysis of an automobile passenger model under whole body vibration Koneru Lakshmaiah Education Foundation," 2023, doi: 10.21203/rs.3.rs-2930805/v1.

- [51] Guillermo Giraldo, “Computing rayleigh damping coefficients: Knowledge base,” SimScale, Feb. 02, 2022.
- [52] M. H. Rahman and C. Gupta, “Computation of Rayleigh damping coefficient of a rectangular submerged floating tunnel (SFT),” SN Appl Sci, vol. 2, no. 5, May 2020, doi: 10.1007/s42452-020-2629-z.
- [53] A. Paixão, E. Fortunato, and R. Calçada, “The effect of differential settlements on the dynamic response of the train-track system: A numerical study,” Eng Struct, vol. 88, pp. 216–224, Apr. 2015, doi: 10.1016/j.engstruct.2015.01.044.
- [54] A. Kahraman, A. A. Kharazi, and M. Umrani, “A deformable body dynamic analysis of planetary gears with thin rims [5],” Journal of Sound and Vibration, vol. 262, no. 3. Academic Press, pp. 752–768, May 01, 2003. doi: 10.1016/S0022-460X(03)00122-6.
- [55] S. Hajdu and P. Gáspár, “Multi-body modelling of single-mast stacker cranes,” 2016.
- [56] “Mechanical metallurgy - Dieter_ George Ellwood”.
- [57] Balram, “2 (two) lane road width in India as per IRC,” Civil Sir, Jun. 21, 2023. <https://civilsir.com/2-two-lane-road-width-in-india-as-per-irc/> (accessed Sep. 02, 2023).
- [58] “Principles of landscape gardening (0+1),” Indian Council of Agricultural Research. <http://ecoursesonline.iasri.res.in/mod/page/view.php?id=6991> (accessed Sep. 02, 2023).
- [59] “What is the tyre size of Tata Nexon? @ Zigwheels,” ZigWheels.com. <https://www.zigwheels.com/newcars/faqs/what-is-the-tyre-size-of-tata-nexon> (accessed Sep. 02, 2023).